TOR VERGATA
UNIVERSITÀ DEGLI STUDI DI ROMA

Development of Computational Tools for Cardiovascular Applications

Eirini Kardampiki

A thesis presented in fulfillment of the requirements for the degree of Doctor of Philosophy

Tutor & Coordinator: Marco Evangelos Biancolini

Department of Enterprise Engineering
University of Rome Tor Vergata
XXXVI Ph.D. cycle
A.Y. 2023/2024
Rome, Italy

Table of Contents

Acknowledgements

I extend my gratitude to my thesis supervisor, Prof. Marco Evangelos Biancolini, whose valuable support played a pivotal role in shaping this research. Additionally, I want to thank Dr. Emiliano Costa and Dr. Karen-Helen Støverud for their guidance during my work in RINA (Rome) and SINTEF (Trondheim) respectively. They did everything within their power to help me, investing time and effort in my intellectual development throughout this journey.

I wish to express my profound gratefulness to the European-funded MeDiTATe project for its funding that made my doctoral research possible. The support provided through Marie Skłodowska-Curie grant agreement No. 859836, has been instrumental in shaping the trajectory of my academic journey. This financial support not only facilitated the exploration of my research questions but also allowed me to engage in international collaborations, attend conferences, and access resources vital for the successful completion of my PhD.

No journey is complete without the unwavering support of those closest to us. I would like to thank my family and friends for their support. Finally, and most of all, I need to thank my anchor: my partner, who always encourages me to embrace new challenges. Thanks for being the best listener and advisor I could ever ask for!

Abstract

Cardiovascular diseases (CVDs) are a group of disorders of the heart and blood vessels and constitute the leading cause of death globally. Among the most common CVDs are pulmonary atresia and abdominal aneurysms which are mainly treated with modified Blalock–Taussig shunt operation (MBTS) and Endovascular Aneurysm Repair (EVAR) procedure respectively.

During MBTS, a synthetic shunt is implanted between the subclavian and pulmonary arteries to supply the blood with sufficient levels of oxygen. Even though the shape of the implant plays a crucial role in the operation's success, its' selection relies on clinicians' experience. To offer a personalized shunt morphology recommendation to patients, we developed a static Reduced Order Model (ROM) trained on Computational Fluid Dynamics (CFD) data which predicts the fluid flow solution as a function of critical morphological shunt parameters. The MBTS morphological parameterization was performed with the use of Radial Basis Functions. The ROM validation exhibited high precision, indicating a strong possibility of being integrated into clinical use.

EVAR is a minimally invasive procedure for the treatment of abdominal aortic aneurysms, and it is usually performed in patients with aortic diameter exceeding 5 cm. Even though this operation is characterized by low mortality and morbidity rates compared to open surgery, it also comes with some complications such as challenging intraoperative navigation due to guidewire-induced deformations and significant risk of post-operative thrombus formation. Concerning those issues, we performed two distinct studies.

The first work refers to the development of a pipeline based on ROM and Finite Elements (FE) simulations for the prediction of the aortic configuration in function of the guidewire orientation, the pre-operative aortic geometry, and material properties in almost real-time. Thanks to this tool, we were able to explore a wide spectrum of possible EVAR cases in a fast and efficient manner. The ROM prediction was found to offer sufficient precision. The developed framework showed the potential to support the clinicians' decision-making process pre and intra operatively, reducing the use of radiation and contrast agents.

The second work is related to the prediction of post-EVAR intra-prosthetic thrombus (IPT) formation through a holistic CFD analysis among simplified models of the three most popular commercial stent grafts, i.e., Zenith Alpha, Excluder, and Endurant II. For this work, we quantified the backflow, investigated the orientation of velocity vectors, and calculated the shear strain rates as well as the most common Wall-Shear-Stress related indices. Our main finding was that the simplified model of Zenith Alpha experiences higher recirculation and shear strain rates on its flared extension compared to the other grafts, which might explain its relatively higher susceptibility to thrombus formation. Conversely, the WSS parameters provided us with controversial results.

In summary, three independent works were developed in the framework of this Ph.D. Two of them were focused on the ROM build-up to bridge the time gap between computational simulations and clinical reality. Achieving almost real-time ROM response on both works seems a promising start, which needs to be further investigated. Acknowledging the diversity in patients' morphologies, both studies were conducted with a focus on individualized healthcare guidance through the consideration of patient-specific anatomies. The third study, dedicated to the post-EVAR IPT formation, revealed that blood flow patterns, developed within a stent graft, can regulate thrombotic phenomena. The method of analyzing blood flow data was found to be crucial, showing that the conventional examination of WSS parameters might fall short of information. Finally, it appears that comprehensive and interdisciplinary approaches are essential and efficient both for explaining intricate cardiovascular issues and for planning and performing successful personalized treatments.

List of Abbreviations

AAA	Abdominal Aortic Aneurysm
CAD	Computer-Aided Design
CAE	Computer-Aided Engineering
CCHD	Cyanotic Congenital Heart Disease
CFD	Computational Fluid Dynamics
CPU	Central Processing Unit
CSP	Cylindrical Source Points
CT	Computed Tomography
CTA	Computed Tomography Angiography
CVD	Cardiovascular diseases
DA	Descending Aorta
DICOM	Digital Imaging and Communications in Medicine
DOE	Design of Experiments
DPM	Discrete Phase Modeling
DSA	Digital Subtraction Angiography
DSP	Diameter Source Points
ECAP	Endothelial Cell Activation Potential
EVAR	Endovascular Aneurysm Repair
FE	Finite Element
GARS	Genetic Aggregation Response Surface
GP	Glycoprotein
GUI	Graphical User Interface
HPC	High-Performance Computing
IPT	Intra-prosthetic thrombus
ISP	Inferior Source Points
LCRS	Local Coordinate Reference System
LGO	Limb Graft Occlusion
MBTS	Modified Blalock–Taussig Shunt
MRI	Magnetic Resonance Imaging
OSI	Oscillatory Shear Index
PA	Pulmonary atresia

PISO	Pressure-Implicit with Splitting of Operators
RBFs	Radial Basis Functions
RCCA/LCCA	Right/Left Common Carotid Arteries
RCR	Resistance Compliance Resistance
ROI	Region of Interest
ROM	Reduced Order Modeling
RPA/LPA	Right/Left Pulmonary Artery
RS	Response Surface
RSA/LSA	Right/Left Subclavian Artery
SP	Source Points
SSP	Superior Source Points
SSR	Shear Strain Rate
SVD	Singular Value Decomposition
TAWSS	Time Averaged Wall Shear Stress
UDF	User-Defined Function
US	Ultrasound
vWF	Von Willebrand Factor
WSS	Wall Shear Stresses

1 Introduction

Cardiovascular diseases (CVDs) encompass a wide range of disorders that affect the heart and blood vessels, representing a leading global health challenge[1]. Among the most common CVDs are aortic and pulmonary diseases, heart failure, and stroke, which contribute significantly to morbidity and mortality worldwide. Often, the origin of these diseases consists of a combination of genetic, lifestyle, and environmental factors, with risk factors such as high blood pressure, high cholesterol, smoking, obesity, and diabetes playing pivotal roles[2,3]. The impact of CVDs affects individuals' quality of life and places a substantial burden on healthcare systems[4]. Prevention, early detection, and effective management are key strategies in mitigating the effects of CVDs[5]. Simultaneously, advancements in medical research and treatment modalities also help address this pervasive health issue. Delving into the root causes of CVDs, advancing current therapy modalities, and developing personalized medicine is the state of the art of healthcare research[6,7,8]. In the light of latest advancements in the biomedical field, this doctoral research aims to develop supportive tools for facilitating some of the most common cardiovascular operations as well as mitigating potential post-operative complications. More precisely, the developed tools are designed for applications in pulmonary atresia (PA) and its corresponding surgery, i.e. modified Blalock Taussig shunt (MBTS) as well as abdominal aortic aneurysms and their treatment with Endovascular Aneurysm Repair procedure (EVAR). The following section delves into the medical background of these diseases, outlining the associated challenges in their treatment and revealing the driving motivation behind our research.

1.1 Cyanotic Congenital Heart Diseases

Cyanotic congenital heart disease (CCHD) is any heart defect present at birth that reduces the amount of oxygen delivered to the human body. Newborns with CCHD typically experience blue baby syndrome. This syndrome is expressed with a bluish appearance of the neonate's skin color mainly on the lips, earlobes, and nail beds due to poor blood oxygenation. Congenital heart defects are present in about 9 of every 1000 live-born children and approximately 25% of them are considered CCHD[9].

Usually, infants diagnosed with CCHD need heart surgery or other interventions to survive.

Within the realm of CCHD lies the dysfunction of the pulmonary valve. Pulmonary valve stenosis is a type of heart valve disease that involves the narrowing of the pulmonary valve, which controls the blood flow from the heart's right ventricle into the pulmonary artery. This condition leads to reduced blood flow in the pulmonary artery and excessive strain of the right heart ventricle, which might lead to heart failure[10]. Pulmonary atresia represents the most severe form of pulmonary valve stenosis, in which the pulmonary valve is completely nonfunctional, i.e. no blood can be supplied to the lungs. It has been estimated that its occurrence frequency is 1 in every 7100 babies born in the United States yearly[11].

1.1.1 Modified Blalock Taussig Shunt

Among the most widespread approaches to tackle pulmonary valve stenosis and atresia is the modified Blalock–Taussig shunt (MBTS): a surgical procedure that consists of implanting a synthetic shunt between the subclavian and pulmonary artery (Fig. 1)[12]. In this way, sufficient levels of oxygenated blood are delivered to the pulmonary circulation. Although the implanted shunt does not guarantee the holistic repair of pulmonary vascular blockage, it offers a time extension until the child grows up to subsequently proceed with a permanent surgical treatment[13]. In general, the MBTS is considered a low-risk management option for the palliation of congenital heart diseases. Nevertheless, the danger associated with this intervention should not be downplayed, as the overall mortality and composite morbidity rates remain relatively high at 7.2% and 13.1%, respectively[13,14].

To date, in clinical practice, the selection of the suitable MBTS implant is performed by exclusively considering its cross-sectional diameter. Surgeons select the optimal MBTS implant for each patient according to their experience, their evaluation of the patient's condition and weight, and other clinical factors[15]. Beyond these aspects, several works from the literature have underlined the importance of patient-specific approaches that personalize treatment for each patient[16,17]. In practice, if the shunt is undersized, the thrombosis risk soars[18]. On the contrary, if the shunt

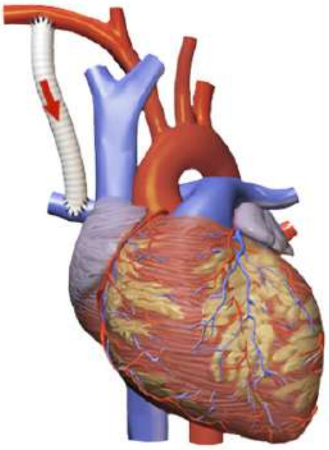

Figure 1: Representation of the successful shunt implantation between the right subclavian and pulmonary artery employing the modified Blalock Taussig shunt procedure.

is oversized, a state of pulmonary overflow with consequent diastolic pressure and systemic perfusion decrease is detected. Subsequently, from the clinical state of the art, it appears clear that MBTS sizing is pivotal in managing complex CCHD[19,20].

Taking into account the current literature status, we present a static Reduced Order Model (ROM) for the fast prediction of the most significant fluid flow parameters, i.e., velocity, pressure, and wall shear stresses, of different MBTS configurations. The objective is to combine ROM, Computational Fluid Dynamics (CFD), and mesh morphing techniques to overcome the computational expense and obtain high-fidelity analysis of a wide range of MBTS shapes (Study I).

1.2 Abdominal Aortic Aneurysm

The aorta is the principal blood vessel responsible for the delivery of oxygen-rich blood from the heart to the rest of the body[21]. The aorta can be subdivided into smaller distinct segments based on their anatomical position and function. The most common subdivisions are the ascending aorta, the aortic arch, the descending or thoracic aorta, and the abdominal aorta[22]. In this work, we focus on the ascending, thoracic and the abdominal part of the aorta.

According to the literature, every segment of the abdominal aorta with a diameter greater than 3 cm is considered an abdominal aortic aneurysm (AAA)[23]. Aortic aneurysms are the 13th leading cause of death in the United States[24]. They have an incidence of 5 – 10 cases per 100000 and occur more commonly in men over the age of 60[25]. Though aortic aneurysms do not directly cause death, their complications such as dissection or rupture cause approximately 15000 deaths annually[26]. The main challenge in addressing this illness is its asymptomatic nature[27]. AAA often has no symptoms, hence called a silent disease. For the AAA diagnosis, the patient should be subjected to an imaging scan such as Ultrasound (US), Computed Tomography (CT), or Magnetic Resonance Imaging (MRI)[28]. In case this does not happen and the aneurysm ruptures, the mortality rates are high, ranging between 32% and 70%, with significant associated morbidity[29]. Therefore, the principle, that prevention is better than cure, applies to this disease.

When a patient is diagnosed with AAA, clinicians make a decision between two strategies: either frequent health checkups and imaging, called medical monitoring, or surgical operation. The second option is suggested for patients with aneurysm size bigger than 5 cm or aneurysm growth rate of 0.5 cm over a period of six months to a year[30,31,32]. However, the intervention criterion is mainly empirical and not patient-specific. For example, some patients experience rupture below the aforementioned threshold while others at considerably larger diameters[33]. Surgical procedures for the treatment of AAAs include Endovascular Aneurysm Repair (EVAR) and open surgery.

1.2.1 Endovascular Aneurysm Repair

During EVAR, a stent graft, compressed inside a catheter, is inserted from the femoral artery to its distal implantation location. Subsequently, as shown in Fig. 2, the graft gets unfolded in the intended position. In this manner, the blood flow is diverted away from the aneurysmatic sac and ultimately the aneurysm rupture is prevented. In open surgery, clinicians cut away the aneurysmatic portion of the aorta and substitute it with a stent graft, which is sewn onto the ends of the aorta[34]. EVAR is usually selected because it is minimally invasive, guaranteeing reduced blood loss and short hospital stays[35]. Nevertheless, recent works show the early survival benefits of EVAR decrease or even get lost over time, with EVAR carrying a higher risk of rupture and secondary intervention than open surgical repair in the long term[36,37,38]. The most common complications associated with EVAR are graft endoleak, migration and thrombosis, which occur with a corresponding frequency of 15 — 30%[39,40], 1 – 10%[41] and 10.7 – 33%[42,43].

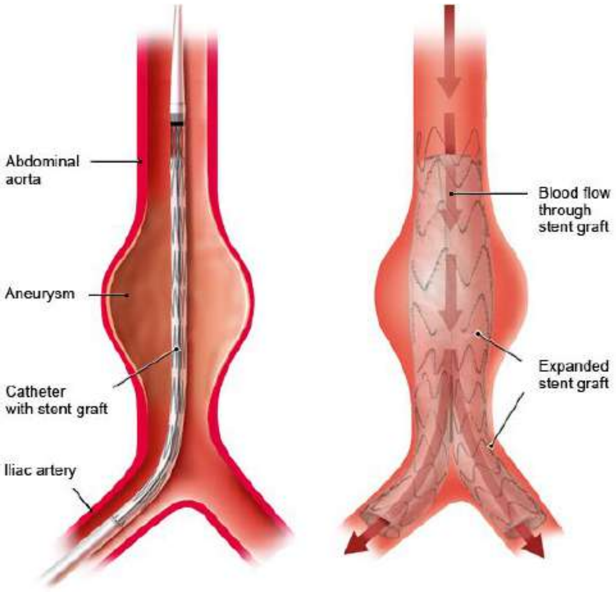

Figure 2: Illustration of EVAR procedure: catheter insertion from the right femoral artery, stent-graft implantation, and blood flow restoration

1.2.2 EVAR planning and navigation challenges

Another issue that arises in EVAR application is the challenging preoperative planning and intraoperative navigation. As already elucidated, the stent graft is introduced through a catheter to its intended position, i.e., inside the aneurysmatic bulge. Nonetheless, this procedure consists of several steps. Initially, a soft guidewire is inserted for the atraumatic navigation from the femoral artery to the distal implantation location. Then, a catheter, through which the stent graft will be advanced, is pushed over the former guidewire. Before proceeding to the stent graft deployment, the soft guidewire is substituted with a stiff one. The latter induces a straightening of the iliac artery and facilitates the insertion of the stent graft delivery system[44]. Previous works remarked that the deformation caused by the insertion of the stiff guidewire affects significantly the final configuration of the vessel[45,46,47]. This can have implications for both pre and intra-operative procedures.

Currently, during the pre-operative planning, this updated vessel morphology is not considered, leading to an increased likelihood of choosing sub-optimal stent graft sizing[48]. It has been highlighted that the incidence of deficient stent graft selection is particularly high in cases of tortuous iliac arteries stenting[46]. The suboptimal stent graft size and placement are also linked to higher procedural failures and postoperative complications such as endoleaks, endograft migration, or collapse and kinking of the endograft limbs[49].

Intra-operative navigation during EVAR is mainly performed through 2D fluoroscopy and Digital Subtraction Angiography (DSA) for the real-time visualization of the position of the inserted tools and the vessel's morphology. These acquisitions entail the use of radiations and contrast agents, whose dose increases along with the complexity of the case. This results in potentially harmful exposure to radiation for both patient and clinicians[50]. Furthermore, the limited 2D view provided by the above-mentioned imaging techniques can hinder the success of the procedure, by increasing the operation time and making the intra-operative visualization poor[51]. For this purpose, imaging fusion techniques, that combine the pre-operative CT and X-ray acquisitions are currently adopted. Nonetheless, the registration of pre- and intra-operative data is still time consuming and low in accuracy[52].

In the literature, several researchers have developed finite element (FE) models for simulating the interaction between aortoiliac structure and stiff guidewire[53,54]. Kaladji *et al.*[55] demonstrated that FE simulations can predict guidewire-induced deformations with sufficient accuracy. More precisely, they launched contact FE simulations for 14 patients, concluding that they were able to estimate the aortic deformation due to the insertion of EVAR delivery system, with an average discrepancy of 2.3 ± 1.1 mm. Emendi *et al.*[56] found good agreement in their models between experimental and in vitro studies. However, the computational cost of these simulations is rather high and not compatible with the clinical time frame. Moreover, any minor alteration in the model's configuration or set-up necessitates a new simulation. Finally, from a practical point of view, simulation experts are needed for the set-up, launching, and analysis of the results.

Considering the significance and complexity of estimating the updated vessel geometry, we present a ROM trained on FE simulations for the fast prediction of the guidewire-induced aortic deformations as a function of seven critical mechanical, morphological, and clinical parameters (Study II).

1.2.3 EVAR related blood clots

Clinical data have shown that thrombotic deposits may accumulate both in the main body and the limbs of the stent graft after its implantation[57]. Hitherto, several definitions of intra-prosthetic thrombus (IPT) have been considered in the literature. Most of them take into account the thrombus thickness, extension of the main body circumference, and longitudinal distribution[58,59,60]. The various thrombus definitions have led to a broad range of published incidence rates of developing post-EVAR blood clots. For instance, Mestres *et al.*[60] reported that 24% of the study's admitted patients experienced intra-graft mural thrombus after EVAR. A recent study by Ucci *et al.*[42] calculated the IPT occurrence was 36% on a population of 221 patients treated with EVAR. Regardless of the exact occurrence rate, it appears that thrombotic events, triggered by stent graft implantation, remain a noteworthy EVAR complication.

Post-EVAR thrombosis has been linked with the patient's characteristics such as anatomy, age, lifestyle, health history, and the implantation technique[61,62,63]. However, in recent years, through the analysis of data records, it was detected that the type of abdominal stent graft also matters. This shifted the focus to the side of the manufacturers of commercial abdominal stents[64]. Several studies have been performed for the evaluation of the mechanical and hemodynamic performance of the stent-grafts but without investing the blood clot phenomena[65,66,67,68].

Among the most commonly employed stent grafts are: the Excluder by W.L. Gore, Endurant II by Medtronic, and Zenith Alpha by Cook Medical. Nonetheless, the very last device has raised some concerns in the clinical field with its higher incidence of thrombosis. In 2020, Cook Medical Europe issued an urgent field safety notice emphasizing some stent graft implantation guidelines to avoid thrombus formation and lumen occlusion. In connection to this, Broda *et al.*[69] published a work demonstrating that none of the risk factors suggested by that safety notice or current literature were positively associated with limb graft occlusion (LGO). Additionally, they estimated that the cumulative incidence of LGO after EVAR was 7% per limb for patients treated with Zenith Alpha for up to three years postoperatively. Bogdanovic *et al.*[43] detected that Zenith Alpha has an increased risk of LGO compared to Endurant and Excluder devices. This finding was also confirmed by Ulsaker *et al.*[70], who found that the incidence rate of LGO was significantly higher in patients treated with Zenith Alpha than Endurant II. However, all the previously presented studies investigated the LGO occurrence, which differs from the IPT rates. Draper *et al.*[71] suggested that the IPT occurrence of Zenith Alpha graft was not significantly different compared to the corresponding rates of other commercial grafts.

In terms of physiology, a thrombus is initiated by damage to the endothelial lining of the blood vessels or by the presence of thrombogenic artificial material[72]. Then, due to the hemostasis mechanism, von Willebrand Factor (vWF), which is a large glycoprotein stored in megakaryocytes and platelets, sticks to the aortic wall attracting platelets from the blood flow via its platelet receptors: glycoprotein (GP) Ib-IX-V and αIIbβ3 integrin[73,74]. High blood shear strain rates enhance the reformation of vWF from a globular to an elongated/stretched molecule[75,76]. This updated vWF morphology is characterized by an increased number of binding sites leading to the recruitment of additional platelets[77]. As more and more platelets adhere to the wall while exposed to high strain rates, eventually, after an elapsed period of time, they get activated[78,79]. During their activation, platelets get a more extended and spiky form and release the contents of their granules and bound fibrinogen, which support the thrombus stabilization[80,81]. The cycle of platelet adhesion, aggregation, and activation may continue until the lumen is completely occluded or a stable thrombus is formed[82].

A substantial part of the research community supports examining the wall shear stresses (WSS) for the prediction of thrombus formation. This concept is based on the fact that the endothelium responds to the changes of the applied shear stress by altering its anti-inflammatory and anti-thrombogenic properties[83]. Among the most diffused WSS indices are the time averaged wall shear stresses (TAWSS), oscillating shear index (OSI), and the endothelial cell activation potential (ECAP). Multiple studies have suggested critical ranges for these parameters, attempting to link them with thrombotic phenomena. In general, high OSI and ECAP values as well as low TAWSS values are considered blood clot predisposed conditions[84,85]. Tzirakis *et al.*[86] and Kelsey *et al.*[84] found a good correlation of OSI and TAWSS values with thrombus formation in AAAs[84,86]. On the contrary, Arzani *et al.*[87] reported that low OSI triggered blood clot formation, while TAWSS were poorly associated with thrombotic events in AAAs. Hence, the significance of these parameters is yet disputed. To our knowledge, no work studying the post-EVAR IPT occurrence on abdominal stent grafts through WSS analysis has been presented before.

Hemodynamic works have also highlighted the bond between recirculating flow and the development of IPT. Slowly recirculating flow, due to core jet flow patterns through a stenosis, promotes platelets' aggregation and activation[88]. More precisely, platelets moving through a stenotic area experience high shear stresses, which lead to their activation. When these activated platelets are moving further down to the graft, they are brought into contact by the contracting streamlines on the slower side of the shear layer. When trapped within a recirculating area, platelets slide along to the aortic wall, from the flow separation till reattachment point[89]. This condition favors thrombus generation. Martorell *et al.*[90] stated that endothelial health is preserved by arterial flow but jeopardized in regions of flow recirculation in a quasi-linear manner.

In light of the aforementioned theories, we present a holistic blood flow analysis of three simplified abdominal commercial stent grafts: Zenith Alpha, Excluder and Endurant II (Study III). The objective of this work is the detection of thrombotic predictors. For this purpose, we evaluate the shear strain rates, WSS related indices, and examine the recirculation patterns.

In a nutshell, in the context of this research work, three independent works were performed:

- Development of Reduced Order Model for the support of modified Blalock Taussig shunt procedures, i.e. **Study I**
- Development of Reduced Order Model for the assisting of the pre-operative planning and intra-operative EVAR navigation, i.e. **Study II**
- Investigation of the thrombotic events on simplified abdominal commercial stent grafts, through computational fluid dynamic simulations, i.e. **Study III**

2 Materials and Methods

This section provides a detailed description of both the materials and the specific procedures employed for the conduction of the aforementioned studies. Initially, the data acquisition and image segmentation are analyzed. Thereafter, the computational fluid dynamic and the finite element modeling are presented for the relevant works. Subsequently, the Radial Basis Functions mesh-morphing technique is thoroughly described. Finally, the background and set-up of the developed Reduced Order Models are exhibited.

2.1 Image Acquisition and Segmentation

The initial stage in creating digital representations of patients or medical devices involves image acquisition. The quality and fidelity of the acquired images play a pivotal role in subsequent analyses[91]. Factors such as resolution and color accuracy significantly influence the effectiveness of image acquisition systems[92]. The image resolution determines the level of detail that can be captured within an image, typically measured in pixels per unit of length. Therefore, image resolution poses the threshold of achievable precision of image segmentation. Usually, higher image resolution results in clearer segmentation results.

Image segmentation in cardiovascular applications holds significant importance in medical imaging and clinical practice. This process focuses on accurately identifying and delineating the area of interest, in our case abdominal aorta, pulmonary artery, or stent graft through a medical image[93]. More specifically, the digital image gets sliced into various subgroups called image segments. Every image pixel is labeled according to its topology or application relevance[94]. The ultimate goal of this procedure is the reduction of the complexity of the rich-in-information images while facilitating the image analysis.

As already highlighted, image segmentation is valuable for clinical applications but also for in vitro simulations. Healthcare practitioners assess the size, shape, and condition of patients' organs and tissues for diagnosing and monitoring purposes. Even though nowadays there are several automated or semi-automated segmentation tools available, employing Machine Learning or Neural Networks techniques, manual segmentation remains the golden standard for clinicians[95,96,97]. This happens mainly because clinicians hesitate to proceed to decision-making based solely on automatically segmented data. In the field of computational simulations, image segmentation provides us with patient-specific surfaces, which can thereafter be converted to personalized Computer-Aided Design (CAD) models[98].

In the case of Study I, a Computed Tomography (CT) scan was taken from a newborn suffering from complete pulmonary atresia at Fondazione Toscana 'Gabriele Monasterio' (Massa, Italy) with a conventional clinical CT 640-detector scanner (Toshiba Aquilion One, Toshiba, Japan). For Studies II and III, four Computed Tomography Angiography (CTA) scans were acquired at St. Olavs Hospital, using a Siemens scanner (Sectra Somatom, Syngo CT): one for an AAA patient and three for the pre-implantation state of the examined stent grafts, i.e. Zenith Alpha, Excluder and Endurant II. For the first case, i.e. AAA patient, the pixel spacing and slice thickness were set equal to 0.5 mm × 0.5 mm and 1 mm respectively. For the imaging of the stent grafts, the pixel spacing and slice thickness were tunned equal to 0.3 mm × 0.3 mm and 0.6 mm accordingly.

Image segmentation was performed in 3D Slicer 5.4.0, which is an open-source software for image analysis[99]. In the case of the neonate and the AAA patient, we segmented the cardiovascular volume from the acquired CT scan. On the contrary, for the three stents, we segmented the graft wires and then, we built the stent volume based on them. The followed segmentation procedure is outlined in the form of steps below:

- Image importing: Digital Imaging and Communications in Medicine (DICOM) files were imported into Slicer environment.
- Selection of region of interest (ROI): With the crop volume feature, we excluded all the irrelevant to our application vessels, or organs such as the heart volume.
- Threshold algorithm: Employing the threshold algorithm, we extracted foreground based on gray value information. For example, the applied threshold range for segmentation of the stent grafts was -450 and 3070.

- Segments' erasing: Using the scissors and islands features, we removed some segments that had been retained after the masking algorithm but they were not of interest to our applications.

- Surface smoothing: Lastly, surface smoothing was applied to decrease the surface roughness and make it suitable for computational simulations. The smoothing factor was set to 0.3 for all the performed segmentations. We ensured that the smoothing process had a negligible effect on the total volume of the studied morphologies.

The above-described procedure was applied for the segmentation of neonate's and the stent grafts' scan. The segmentation of the AAA patient was excluded from the aforementioned procedure. For this work, a segmentation algorithm, based on intensity threshold and morphological operations (i.e. binary opening to keep only the largest connected components) was utilized. The algorithm was developed in Python 3.9 to semi-automatically segment the lumen of the abdominal aorta[56].

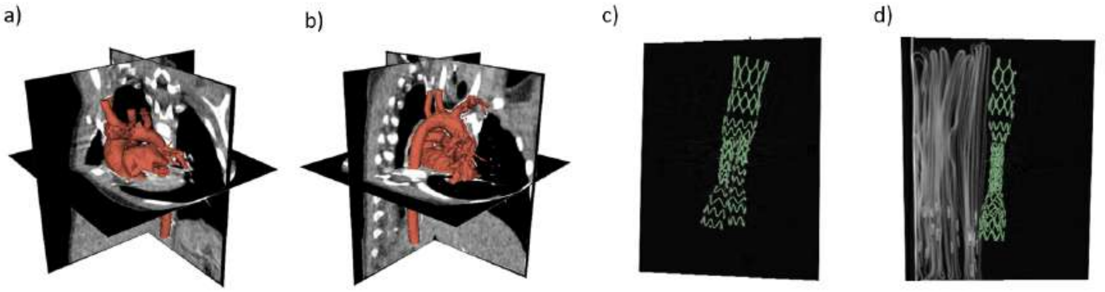

Figure 3: Segmentation of the MBTS case: front view a), back view b) and Zenith-Alpha (Cook Medical) stent graft case coronal view c) and sagittal view d)

After completing the image segmentation, we qualitatively evaluated the accuracy of our results via visual inspection. This is one of the simplest methods in which the original image and the segmented one are overlaid. As illustrated in Fig. 3a and b, by comparing the color of the image pixels and the boundaries of the segmented surface, we were able to estimate the quality of our segmentation. The segmented geometries were considered accurate as long as just a few pixels were mislabelled.

2.2 Computer Aided Design Reconstruction

The output of image segmentation was a file in stereolithography format, which describes the geometrical surface of 3D models as a collection of triangular facets. This format is compatible with some software or applications, however, for performing Computational Fluid Dynamics (CFD) simulations within our software of choice, i.e. Ansys® Fluent, CAD reconstruction was required. For converting the stereolithography files to CAD, Ansys® Spaceclaim, Release 22R1 was employed[100]. Reverse engineering is a demanding procedure that necessitates smooth surfaces and good designing skills. During this process, the user should pay attention is preserving the important features of the geometry.

2.2.1 Study I

For Study I, the CAD of the newborn's vascular configuration was generated through the Skin Surface feature of Ansys® Spaceclaim, Release 22R1. With this tool, surface patches were created on the model's facets. Subsequently, these patches were stitched together, forming a solid body.

Then, an MBTS implant was added between the pulmonary artery and the right subclavian artery. The total length of the implant was 16.4 mm and the diameter at the middle of its length was equal to 4 mm. The implant sizing is in line with the currently employed MBTS shunts[101]. The implantation position was selected under the guidance of surgeons, who specialized in conducting this procedure.

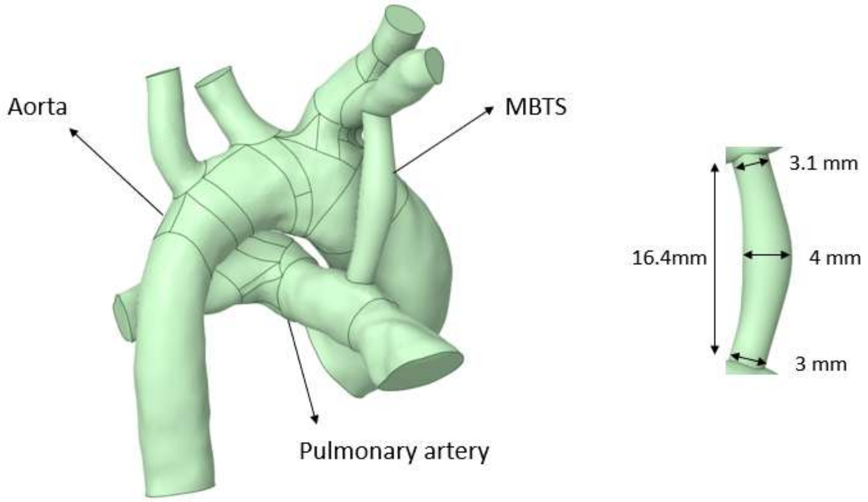

Figure 4: Result of the CAD reconstruction of the pulmonary artery, the aorta, and the MBTS implant of the examined neonate

2.2.2 Study III

For Study III, the CAD reconstruction of the considered stent grafts was performed. As illustrated in Fig. 3 c and d, solely the radiopaque stent frame was extracted from the CT scan. What is more, as shown in Fig. 5b, the stent frame had high density, leading to an artificially increased thickness, i.e., CT artifacts. To minimize the influence of artifacts, we extracted the stent frame morphology based on the center points of the stent's metallic wires. This was decided upon discussion with clinicians. Subsequently, we validated our models based on the nominal dimensions of the physical grafts.

Thereafter, a manual CAD modeling procedure was followed for the generation of the internal volume of the stent graft. We performed interpolation between simplified geometric shapes and elements such as cylinders and circles lengthwise of the metal stent frame to capture the volume nesting inside each stent graft. The results of this procedure are illustrated in Fig. 5a. The primary issue of these morphologies was their unrealistic sharp edges, especially in the bifurcating region. To tackle this defect, the obtained graft CAD models were smoothed along their surface via Autodesk Meshmixer 3.5, so that they become appropriate for Computed Fluid Dynamics (CFD) simulations (Fig. Fig. 5b)[102].

Upon obtaining the precise CAD models, we encountered another challenge: the

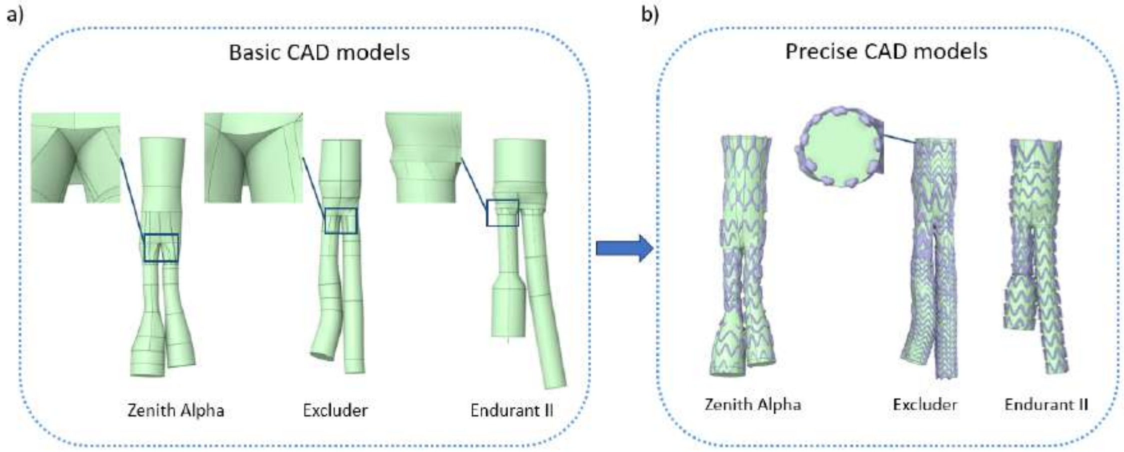

Figure 5: Primary CAD reconstruction of Zenith Alpha, Excluder, and Endurant II with simplified geometric shapes a), precise CAD models achieved via smoothing the surface of the previous models with Autodesk Meshmixer 3.5 b)

examined stents were designed for markedly different aortic sizes. At the same time, finding similar stent graft sizes within the hospital premises was not an option. To enable the comparability of our results, we manually modified the stent geometries according to a uniform sizing hypothesis regarding the nominal dimensions of the graft components. More precisely, we assumed that the stents were designed for an average AAA patient. Subsequently, we identified the available stent graft sizes based on the information provided in manufacturers' brochures. Finally, a common iliac bifurcation angle of 55° was imposed on all the geometries replicating the post-implantation stent morphology. In Fig. 6, the above-described procedure is illustrated.

Recognizing the uncertainty of the final configurations due to the extensive CAD changes that were presented above, we consider the final models as simplified versions of the examined commercial stent grafts, which are in line with manufacturers' sizing. Therefore, any conclusions deriving from this study should not be associated with the performance of the corresponding commercial grafts. To keep it clear, henceforth, we refer to the simplified grafts of Zenith Alpha, Excluder, and Endurant II as models 1, 2, and 3 respectively.

Additionally, in Fig. 6a, the following basic stent dimensions are defined: aortic neck diameter d_n, common iliac diameter on contralateral side d_c, common iliac diameter on ipsilateral side d_i, post-bifurcation diameter on contralateral side d_s,

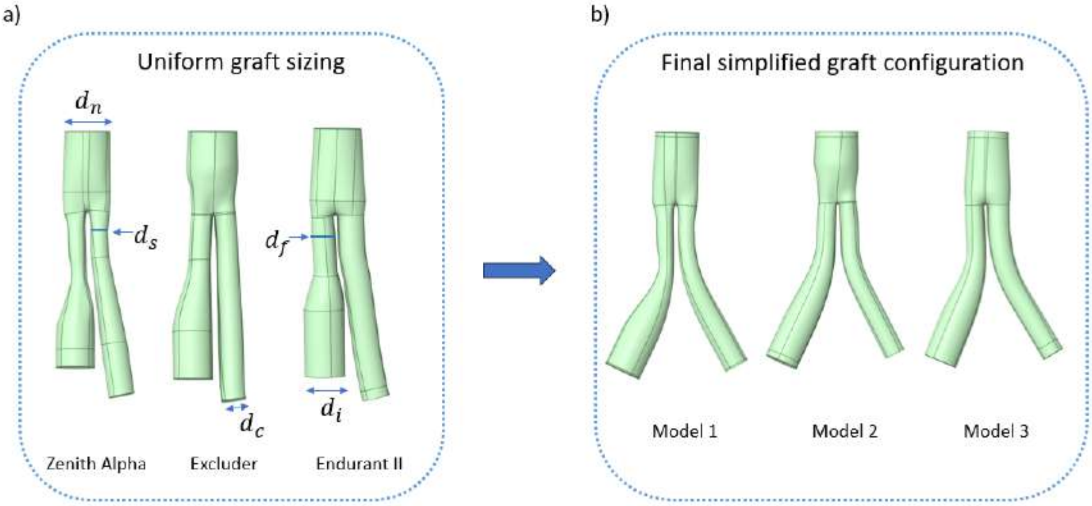

Figure 6: Uniform graft sizing based on manufacturers' brochures for Zenith Alpha, Excluder, and Endurant II stent graft (Table 2) a), introduction of a common iliac bifurcation angle of 55° in the final simplified configuration of Zenith Alpha, Excluder, and Endurant II graft named as model 1, 2, and 3 accordingly b)

post-bifurcation diameter on ipsilateral side d_f. In Table 2, the values of these diameters are reported for each examined stent graft. The slight variations identified among the stent grafts derived from the unique manufacturers' size standardization.

To guarantee the full development of the blood flow within the stents, the models' extremes were extended by 5 times their diameter. Finally, we divided the graft morphologies into 17 zones to facilitate the results' analysis. In Fig. 7, for simplicity reasons, we present solely the volume subdivision of model 1. The same procedure was followed for models 2 and 3. The sections were formed by splitting the stent's centreline every 20 mm with Ansys® Spaceclaim. The ipsilateral and the contralateral sides, designated in Fig. 7, are identified based on the insertion site, which we assume to be the left side in our case. For the sake of simplicity, the ipsilateral and the contralateral graft extensions are also referred to as flared and straight extensions respectively.

	d_n (mm)	d_c (mm)	d_i (mm)	d_s (mm)	d_f (mm)
Model 1	28	16	24	11	11
Model 2	28.5	14.5	23	13	13
Model 3	28	16	24	16	13

Table 2: Basic dimensions of the simplified stent grafts: aortic neck diameter d_n, common iliac diameter in contralateral side d_c, common iliac diameter in ipsilateral side d_i, post-bifurcation diameter in contralateral sided_s, post-bifurcation diameter in ipsilateral side d_f

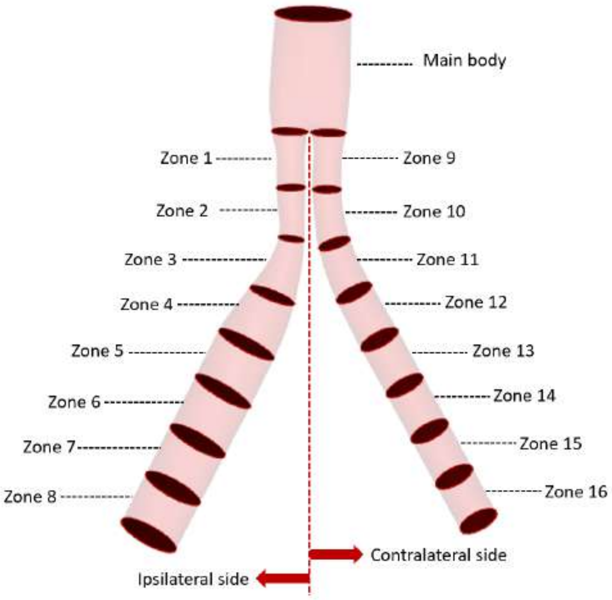

Figure 7: Illustration of the division of the blood flow domain of model 1, i.e. simplified Zenith Alpha, into 17 fluid zones: 8 zones per side and the main body. A similar zone partition is applied for the other examined grafts (Excluder and Endurant II).

2.3 Computational Fluid Dynamics

In this part of the work, the Computational Fluid Dynamics modeling of studies I and III is presented. Initially, the mesh generation in the involved geometries is described and then a mesh sensitivity analysis is displayed. Eventually, the CFD setup is presented along with the developed user-defined functions.

2.3.1 Mesh generation

The concept of a mesh as a discretization in space has been associated with computational methods since the first attempts to obtain numerical solutions of partial differential equations. Establishing a suitable mesh was long considered to be a rather tedious exercise and a minor part of the computational effort involved in solving the partial differential equations[103]. However, mesh generation has steadily evolved into a discipline in its right drawing on ideas from other fields, in particular mathematics and computer science, and gradually developing its distinct identity[104].

The mesh generation is highly linked to the accuracy of the flow results. A highly detailed mesh can capture the microscale fluid motion, but such precision is often unnecessary. What is more, the computational cost of solving differential equations is proportional to the mesh size. This signifies that a compromise between mesh density and computational cost should be performed, taking into account the nature and the scale of each problem[105]. Finding out the suitable mesh size and its distribution is usually time-consuming and involves trial and error tasks. The final mesh is usually selected upon mesh sensitivity analysis[106]. In this type of analysis, we assess the impact of mesh density (discretization of the computational domain) on the results of numerical simulations. At the same time, we should monitor the flow convergence plots, to ensure sufficient result precision. Finally, the fulfillment of some standard mesh criteria, such as minimum orthogonality and maximum aspect ratio, should be taken care of. As it appears, mesh generation and selection of the final mesh constitute a multifactorial process. Below, we outline the employed mesh procedure for our applications, utilizing the Ansys® Fluent Watertight geometry meshing tool.

2.3.1.1 Study I

For the meshing of the neonate's cardiovascular geometry including the shunt (Fig. 4), an unstructured mesh consisting of 1.79 million polyhedral elements was built. The minimum and maximum cell size of the surface mesh was set equal to 0.2 and 2 mm respectively. To capture the laminar ongoing phenomena close to the boundaries, ten uniform distributed inflation layers with a growth rate of 1.05 and a total thickness of 2.5 mm were introduced. In Fig. 8, a cross-section of the implant's mesh is presented. The minimum orthogonal quality and the maximum aspect ratio were calculated equal to 0.21 and 25 respectively. According to Ansys documentation, these values lay within the acceptable mesh tolerance limits.

Before deciding on the final mesh, a mesh sensitivity analysis was performed.

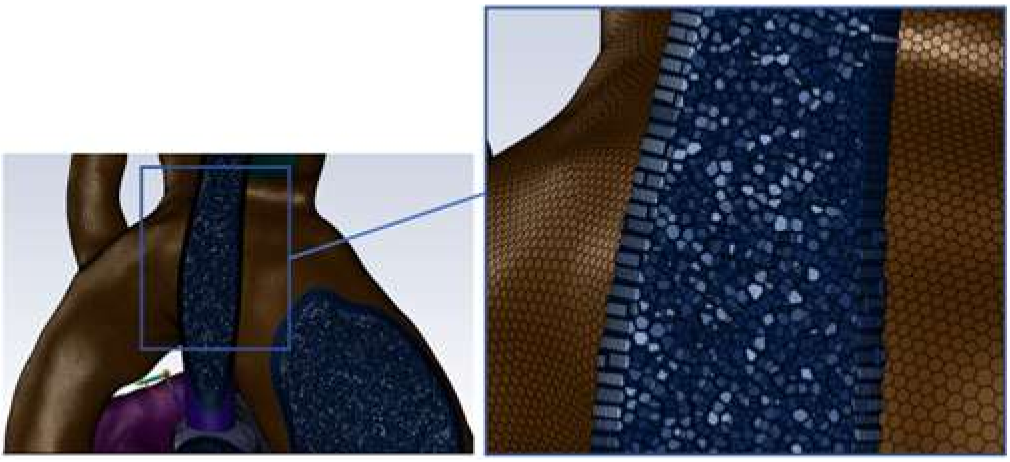

Figure 8: Illustration of the mesh in a cross-section of the shunt (left), further zoom in the ten inflation layers (right)

For this purpose, we generated five meshes with different densities. Afterwards, we solved the flow equations on them and we calculated the area averaged Wall Shear Stresses of the surface of the shunt. We selected this geometrical part because we needed sufficient flow solution precision in it. The results of our analysis are exposed in Fig. 9. The shunt's average Wall-Shear-Stress is getting stabilized for meshes with a density of 1.79 million cells or more. This signifies that our solution won't change significantly beyond this mesh size. For this reason, we selected the above-mentioned mesh for our simulations.

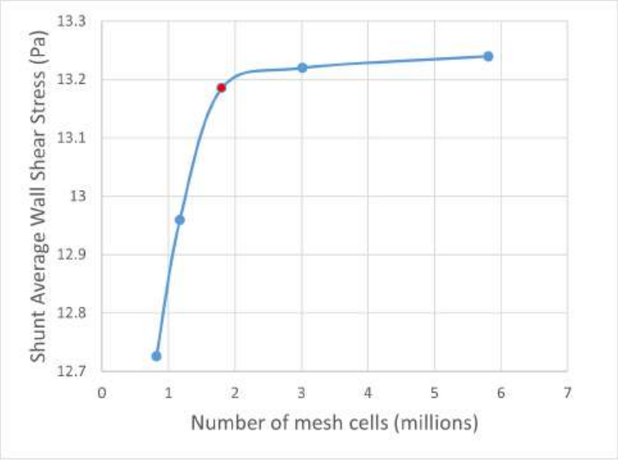

Figure 9: Mesh sensitivity analysis for MBTS study: calculation of area-averaged wall shear stresses as a function of mesh size, red-colored final mesh

2.3.1.2 Study III

For the meshing of the three stent grafts, a similar procedure was followed. We performed a sensitivity analysis to detect the most appropriate meshes for our simulations. In this case, the investigated variable was the maximum wall shear stress, which was located in the bifurcation region for all grafts. The results of the mesh sensitivity analysis for models 1, 2 and 3 are presented in Fig. 10, 11, 12 respectively. Considering the balance between the computational cost and the mesh refinement, we selected the meshes with the following densities: ≈2.1 million cells for model 1, ≈2.5 million cells for model 2, and ≈2.3 million cells for model 3. An interesting observation in the presented graphs is that the maximum wall shear stress is overestimated in the coarse meshes of models 2 and 3 and underestimated in the similar density mesh of model 1. When using a coarse mesh in numerical simulations, there is a tendency for numerical diffusion to occur, leading to the loss of critical flow features. However, the direction of this smoothed-out effect cannot be easily predicted.

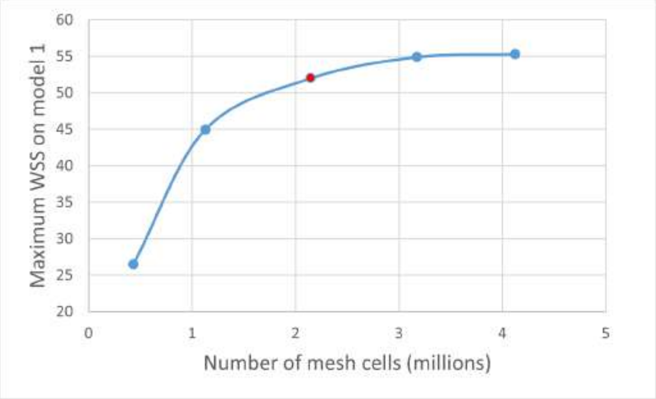

Figure 10: Mesh sensitivity analysis for model 1: calculation of maximum wall shear stress (WSS) as a function of mesh size, red-colored final mesh

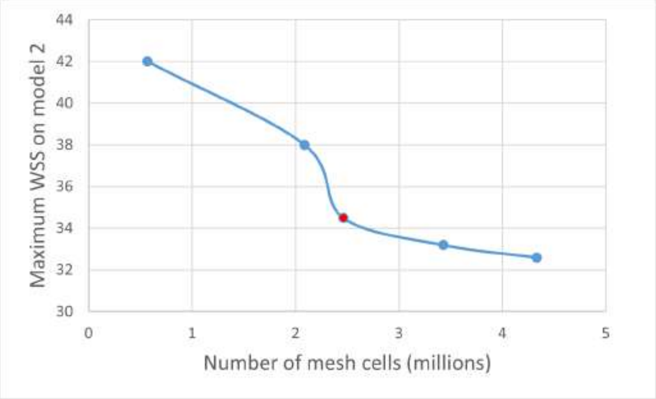

Figure 11: Mesh sensitivity analysis for model 2: calculation of maximum wall shear stress (WSS) as a function of mesh size, red-colored final mesh

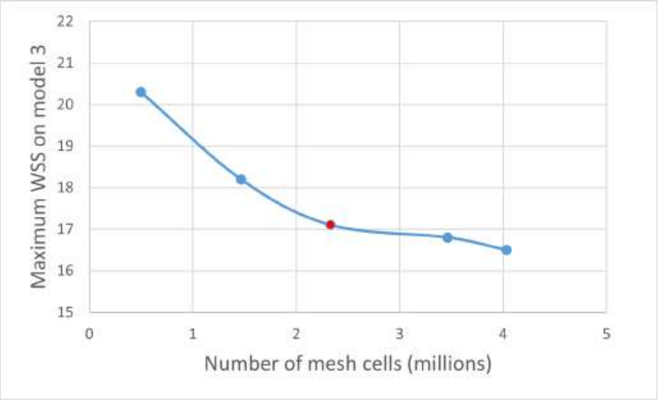

Figure 12: Mesh sensitivity analysis for model 3: calculation of maximum wall shear stress (WSS) as a function of mesh size, red-colored final mesh

Polyhedral mesh elements were employed for the meshing of all the models: the maximum cell length was set to 0.9 mm. The aortic wall was treated with 5 boundary layers with a growth rate of 1.2 and a transition ratio equal to 0.272. The boundary layer set-up is crucial, especially for the calculation of the WSS. In our case, the adopted set-up was selected based on the recommendations of Ansys® Fluent user guide and by looking up already conducted CFD studies in the area of ascending aorta[107,108]. The following mesh quality criteria were respected in all the generated meshes: minimum orthogonality >0.2, maximum aspect ratio <15, and maximum skewness <0.25. An illustration of the mesh in the main cross-section of the stents, with emphasis on the grafts' bifurcation and the transition area between zones 3 to 4, is provided in Fig. 13.

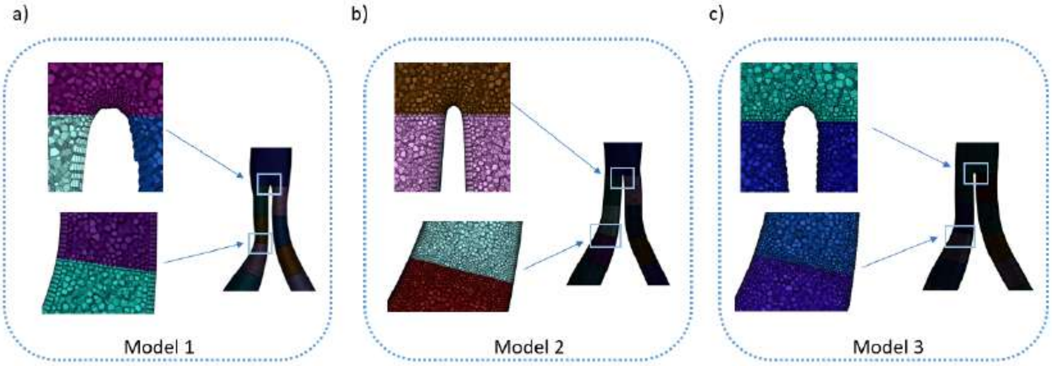

Figure 13: Final computational mesh for model 1 a), model 2 b), and model 3 c) with emphasis on the construction of 5 boundary layers on the aortic wall. The total thickness of the layers is lower at the level of the iliac bifurcation, where the local curvature is high.

2.3.2 CFD set-up

Ansys® Fluent, Release 22R1 and 22R2 were used to solve the governing flow equations for studies I and III accordingly. In the following section, the flow regime, the boundary conditions, the discretization schemes, and the developed user-defined functions are described separately for the two relevant works.

2.3.2.1 Study I

With regards to the MBTS study, a steady state flow regime was adopted and the k-ω SST model was employed for the integration of the turbulent phenomena[109,110]. The main reason for including a turbulent model was that the Reynolds number on the shunt's level was remarkably high, i.e. ≈ 5000, and the laminar solver could not capture the ongoing phenomena. The k-ω SST model was selected against the other turbulence models because it offers good accuracy in the boundary layer region close to the wall. This area is particularly important for the calculation of WSSs. Kabir *et al.*[111] and Perinajová *et al.*[112] confirmed the good agreement between this model and experimental aortic flow data in the wall vicinity.

The blood was considered as a Newtonian fluid with a density and viscosity equal to 1060 kg/m^3 and $3.5 \cdot 10^{-3}$ Pa $\cdot$ s, respectively. Even though the blood is a non-Newtonian fluid, it follows Newtonian nature when the shear rate is above 100 s^{-1}. This happens in large blood vessels like the aorta[113,114]. Therefore, considering the blood as a Newtonian fluid is a satisfactory assumption[115].

We opted to model the systolic peak condition in our simulation as it is one of the most critical phases in the cardiac cycle. During systole, when arterial pressure attains its peak, the stresses applied on both the aorta and the implant are maximized. The examination of these stresses can unveil the presence of cardiovascular issues such as stenosis and thrombosis[116].

The selection of the boundary conditions was performed keeping in mind the age of the studied patient, i.e. an infant. More precisely, we applied a plug inlet velocity boundary condition equal to 0.24 m/s at the aortic valve section. The aortic branches, i.e., the Right/Left Common Carotid Arteries (RCCA/LCCA), Left Subclavian Artery (LSA), and descending aorta (DA) were handled with a constant pressure condition of 55 mmHg. The Right Subclavian Artery (RSA) was treated with a 48 mmHg condition[117]. These values were selected upon discussion with surgeons from Fondazione Toscana 'Gabriele Monasterio'. For the pulmonary branch, the right and the left pulmonary artery (RPA/LPA) boundary conditions were set to a constant pressure condition of 8 mmHg and 7 mmHg, respectively [118]. These pressure values correspond to the physiological pressure conditions of an infant. Finally, a wall condition was imposed on the pulmonary valve boundary to simulate the pulmonary atresia (PA) condition. An illustration of the selected boundary conditions is presented in Fig. 14.

Finally, concerning spatial discretization, second-order upwind schemes were selected for momentum, turbulent kinetic energy, specific dissipation rate, and second-order pressure.

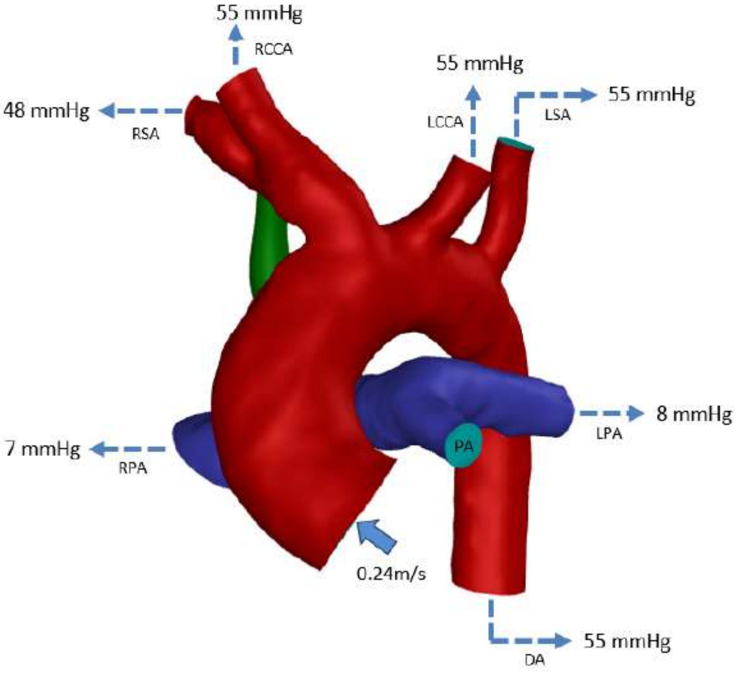

Figure 14: Depiction of the boundary conditions for the aortic and the pulmonary valve (PA) section, the aortic and the pulmonary branches.

2.3.2.2 Study III

In the case of the stent graft work, transient laminar simulations were launched to capture the blood flow field throughout the heart cycle. Following the same rationale as the study I, the blood was modeled as a Newtonian fluid with constant viscosity

Graft type	Extension side	Proximal Resistance R $\left(\frac{\text{kg}}{\text{m}^4 \cdot \text{s}}\right)$	Capacitance C $\left(\frac{\text{m}^4 \cdot \text{s}^2}{\text{kg}}\right)$	Distal Resistance R_d $\left(\frac{\text{kg}}{\text{m}^4 \cdot \text{s}}\right)$
Model 1	contral.	1.195 e+08	1.415 e-09	1.475 e+09
	ipsil.	5.315 e+07	3.184 e-09	6.555 e+08
Model 2	contral.	1.294 e+08	1.308 e-09	1.596 e+09
	ipsil.	5.142 e+07	3.292 e-09	6.342 e+08
Model 3	contral.	1.195 e+08	1.415 e-09	1.475 e+09
	ipsil.	5.315 e+07	3.185 e-09	6.555 e+08

Table 3: RCR parameters for the ipsilateral and the contralateral outlets of model 1, 2, and 3

equal to $3.5 \cdot 10^{-3}$ Pa s and density set to 1060 kg/m^3. A plug-inlet velocity profile, obtained from the blood flow rate curve at the level of the infrarenal aorta, was imposed on the aortic neck cross-section[119]. A Resistance-Compliance-Resistance (RCR) model was adopted for the common iliac contralateral and ipsilateral outlets. The velocity and pressure curves are presented in Fig. 15. As shown, the velocity profile receives negative values between 0.35 and 0.45 s. Flow reversal is a common phenomenon in the infrarenal aorta during early diastole, especially in resting conditions[120,121]. The values of the three-element model were calculated via an in-house MATLAB script so that the outlet pressure curve lies within the physiological range, i.e. 80 and 120 mmHg. Further details can be retrieved in Table 3 and Fig. 16. Finally, a PISO (Pressure-Implicit with Splitting of Operators) solver was employed for the pressure-velocity coupling while second-order schemes were used for the spatial discretization.

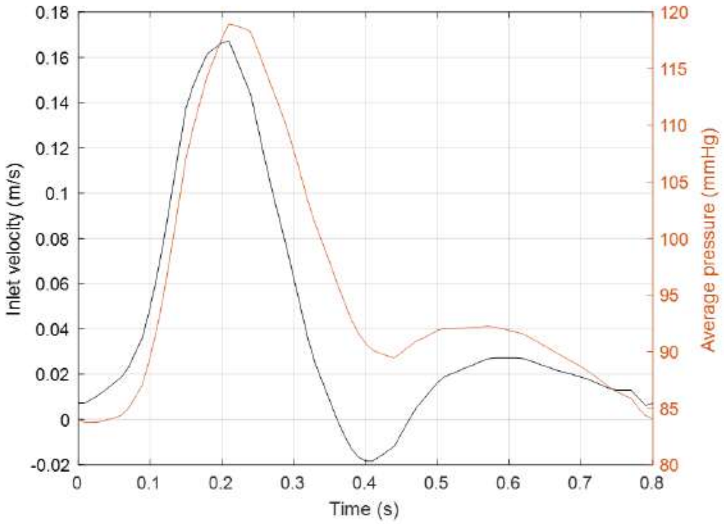

Figure 15: Inlet velocity curve and average pressure outlet curve imposed on the stent grafts during the heart cycle

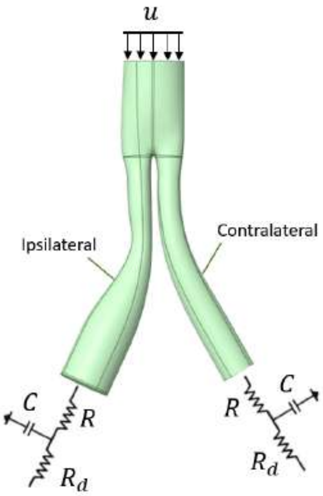

Figure 16: Schematic sketch of the stent graft geometry and the adopted RCR boundary conditions for the case of model 1. Similar boundary conditions were applied for the rest models where: u is the inlet velocity of Fig. 15, R, R_d, the proximal and the distal resistance, and C, the capacitance given in Tab. 3.

2.3.3 Study III: Flow analysis parameters

2.3.3.1 Shear Strain rate

As outlined in the introduction, elevated shear strain rates (SSR) induce the unfolding of vWF, initiating the subsequent platelet processes of adhesion, aggregation, and activation. For tracking the reformation of vWF, we measured the magnitude of SSR in all zones of the examined stent grafts throughout the heart cycle. As already highlighted, the magnitude of SSR holds great significance. Hitherto, many studies have delved into the estimation of the critical SSR above which the vWF changes morphology. Casa *et al.*[122] suggested that shear rates should be kept below 5000 s^{-1} to reduce the risk of IPT formation. Ruggeri[123] calculated that after seven flow seconds, single platelets started adhering and aggregating to the artery boundary when the wall shear rate was 3000 s^{-1}. Sakariassen *et al.*[124] considered the SSR above 4000 s^{-1} as pathological. Taking into consideration these works, we computed the volume, V_{SSR}, for each zone of the considered grafts in which SSR exceeds 3000 s^{-1}, in line with the most conservative study:

$$V_{SSR} = \sum_{i}^{N} v_{cell} \quad \forall \; SSR_{cell} > 3000 \; s^{-1} \tag{1}$$

where N is the total number of cells of each zone, v_{cell} is the volume of each cell within a zone.

2.3.3.2 WSS-related indices

As highlighted in the introduction, the analysis of wall shear stresses (WSS) can be used for examining the endothelium's health and therefore possibly predicting IPT events. Among the most diffused WSS-related indices are the following:

- Time Averaged Wall Shear Stresses ($TAWSS$): Low WSS regions within medical devices have been previously linked to blood clot formation[125,126]. Biochemically, low values of WSS are related to a decrease in the production of prostacyclin, prostaglandins, and nitric oxide (NO), which are agents in charge of protecting the arterial wall against pro-thrombotic activities[127,128]. Most studies suggest that $TAWSS$ in the range of 0.2 – 0.3 Pa are linked with blood clotting. The definition of $TAWSS$ is given from the following equation:

  $$TAWSS = \frac{1}{T}\int_0^T |\mathbf{WSS}|dt, \tag{2}$$

  where T is the duration of a heart cycle.

- Oscillatory Shear Index (OSI): OSI represents the temporal variation in WSS direction,

  $$OSI = \frac{1}{2}\left(1 - \frac{|\int_0^T \mathbf{WSS}dt|}{TAWSS}\right) \tag{3}$$

  and has been shown to affect the endothelial cells (EC) behaviour[129]. The majority of studies support that there is an association between high OSI and thrombus formation[130]. More precisely, regions with OSI exceeding ≈0.3 are considered as thrombo-prone[86,84]. However, some studies have contradicted this, finding low OSI in thrombotic regions[87,131,132].

- Endothelial Cell Activation Potential ($ECAP$): The endothelial cell activation potential characterizes the degree of thrombogenic susceptibility[87]. This parameter localizes regions of high OSI and low $TAWSS$ by using the ratio of OSI and the $TAWSS$.

$$ECAP = \frac{OSI}{TAWSS} \tag{4}$$

Areas with $ECAP$ values above 1.4 Pa^{-1} are viewed as thrombo-prone[84].

2.3.3.3 Backflow and vector analysis

Our study also focused on the quantification of the recirculating areas. Undeniably, the measurement of the length and intensity of a recirculation region is a very demanding task because of the dynamic nature of the blood flow. To tackle this challenge, we examined recirculation by two different means: the quantitative calculation of the backflow and the qualitative illustration of the flow velocity vectors. The estimation of backflow stems from the fact that part of a swirl, which exists within a flow, has a negative velocity with respect to the main bloodstream. By measuring this portion of the swirl, we can get an estimation of the existence and the magnitude of recirculation. However, backflow does not occur only due to recirculation. It can also happen because of flow deceleration, imposed change in the flow direction, and flow turbulence. In our application, we are interested in the backflow due to flow separation. Nonetheless, we cannot exclude the backflow deriving from other sources. Keeping that in mind, our study proposes that the detection of backflow can be used as a tool for further investigating whether a recirculation area really exists. In other words, backflow constitutes a necessary but not sufficient condition for the existence of recirculation. For enhancing the analysis of the backflow and recirculation patterns, the backflow magnitude and intensity of each fluid zone were defined with the following indices:

$$V_{back} = \sum_{i}^{N} v_{cell} \quad \forall \ u_{cell} < 0, \tag{5}$$

$$V_{back}(\%) = \frac{V_{back}}{V_{zone}} \cdot 100\%. \tag{6}$$

where V_{back} is the volume summation of the cells that have a negative velocity component u_{cell} with respect to the main flow direction. Finally, V_{back} (%) is the percentage of backflow volume with respect to the total volume of each zone, i.e.,

V_{zone}. A similar approach was adopted by Martorell *et al.*[90], who evaluated the degree of flow recirculation through the analysis of velocity vectors.

2.3.4 Study III: User Defined Functions

For the application of the RCR model on the grafts' outlets and the analysis of the results of the stent grafts' study, we generated some tailored codes, named User-Defined Functions (UDFs). In the context of Ansys® Fluent, a UDF is a customized function that users can create to extend or enhance the standard features of the FLUENT solver. These functions allow users to define their own boundary conditions, material properties, specify customized model parameters (e.g., discrete phase model (DPM), multiphase models), initialize a solution, or facilitate postprocessing. UDFs are written in the C programming language using any text editor and the source code file is saved with a .c extension. Multiple UDFs can be defined within one source file. Finally, to utilize UDFs, it is necessary to undergo a compilation process. In our case, we used the Build-in Compiler provided within the Fluent environment.

For carrying out our study, we created four distinct UDFs for the following operations:

- Quantification of the percentage of the backflow volume of each zone throughout the heart cycle, via `backflow.c`
- Measurement of the graft's volume exposed to high shear strain rates, >3000 s^{-1} per zone, via `shear_rate.c`
- Assessment of $TAWSS$, OSI, $ECAP$, via `stresses.c`
- Implementation of RCR model on the graft's outlets, via `RCR.c`

In Fig. 17, the flow chart of `backflow.c` is presented. The code begins by initializing a summation variable, $V_{back,i}$, for each zone, i, of the stent graft. Subsequently, a zone loop starts, in which we examine the N cells of each zone. The value of N changes from zone to zone. Then, we analyze the velocity of each cell, j, of each zone, i, in a local coordinate system that is perpendicular to the graft's centerline.

If the U_z component is negative, then we set the value of the flag variable named $Var(i,j)$ to 1 and we add the volume of the cell, $V(i,j)$ in the summation variable of the zone that it belongs to, i.e., $V_{back,i}$. If the U_z component is positive, i.e. blood moving downstream, the flag $Var(i,j)$ is set to zero and the cell loop continues. The algorithm ends when all zones are examined. This procedure is executed for every time step. We deem this velocity analysis accurate since there are minimal changes in the centerline direction in most segments of the graft. By knowing the backflow volume of each zone, $V_{back,i}$, we calculated the percentage of the backflow over the total volume of each zone with equation 6.

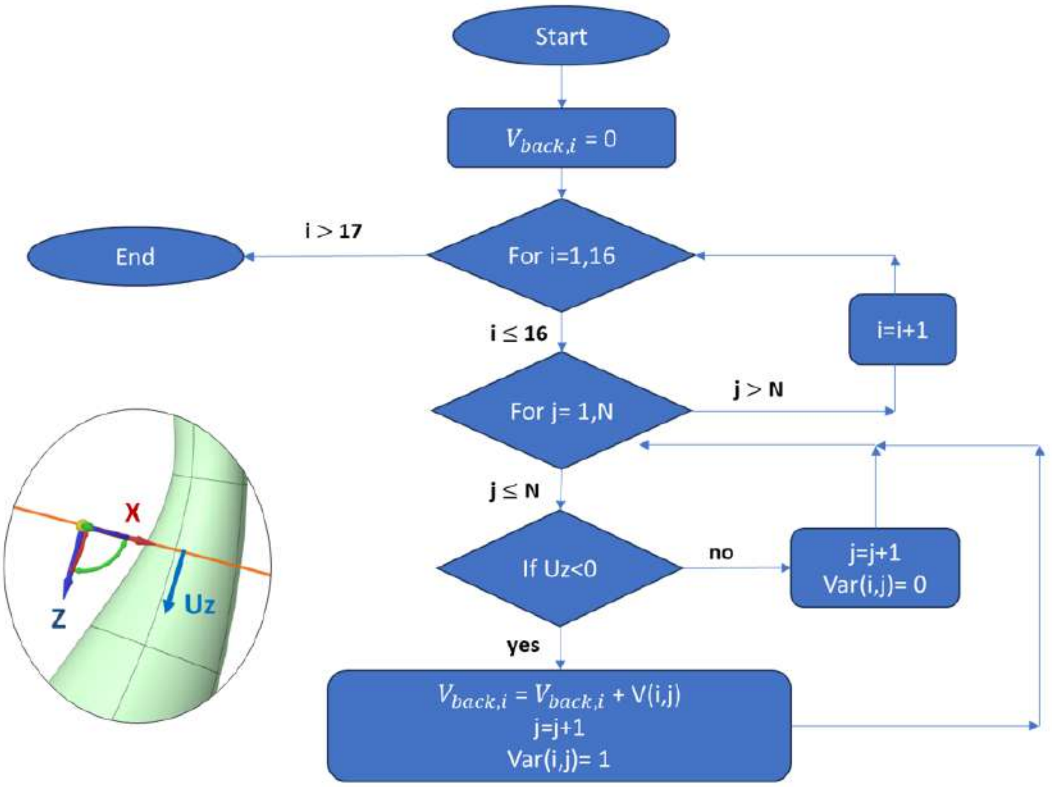

Figure 17: Flow chart of `backflow.c` including the velocity analysis on a local coordinate system

In Fig. 18, the results of `backflow.c` are showcased. In this example, we are examining the flow on zones 3 and 4 of model 1 at the systolic peak. On the left side (a), where velocity magnitude vectors are plotted, a significant swirl appears to be formed near the aortic wall. On the right side (b), our algorithm has captured the backward-moving portion of this swirl, i.e. volume represented in red. With the exhibited example, the effectiveness of the adopted approach for the detection of recirculating areas is demonstrated.

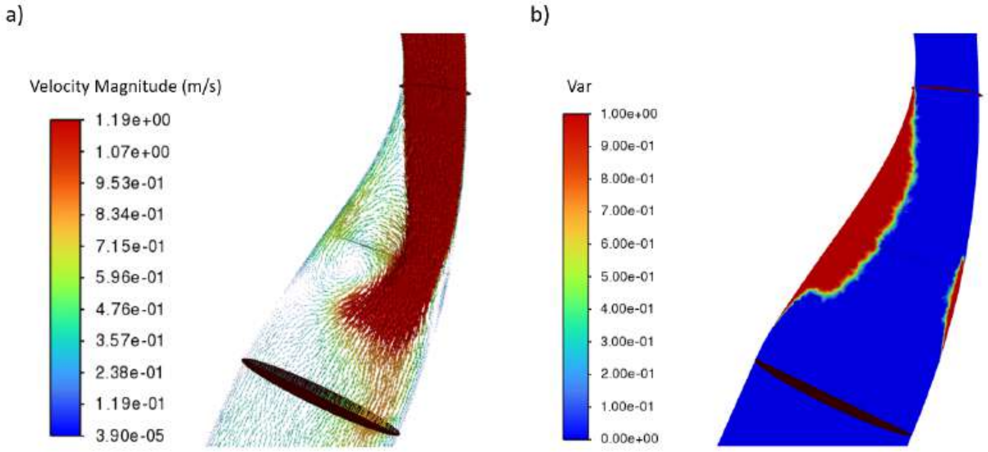

Figure 18: Results of `backflow.c` algorithm: good correlation between recirculation and backflow on zones 3 and 4 of model 1 at the systolic peak

A similar procedure was followed for the calculation of the graft's volume that is exposed to shear strain rates above $3000s^{-1}$, i.e. `shear_rate.c` algorithm. For clarification purposes, we did not calculate the shear strain rate directly. Such a task is very complex because we would have to analyze the strain rate tensor, i.e. 3 x 3 matrix, into a local coordinate system on each cell and then retain only the off-diagonal elements. Instead, we calculated the magnitude of the strain rate tensor on each computational model and we found out that the peak values, that are of interest, occur on the graft's wall. In this region, shear forces dominate, therefore, the assumption that the strain rate is almost equal to the shear strain rate is valid.

2.4 Finite Element

In this section, the Finite Element (FE) modeling of the EVAR study is presented. Initially, the surface mesh generation and the problem's boundary conditions are described. Then, the model's parameterization in terms of mechanical and clinical properties is reported. The geometrical parameterization of the problem is omitted since it is explicitly described in the section 2.5.3.

2.4.1 Study II: Set-up

The simulation of EVAR navigation was performed with the commercial FE software, Ansys® LS-DYNA, Release 22R1. The segmented geometry of the aorta was discretized with triangular shell elements, choosing a thickness of 2.5 mm and a characteristic length of 1.4 mm (obtained based on a mesh sensitivity analysis), and modeled as a linear elastic material. A geometric model of the guidewire was created and discretized with beam elements, selecting a 4 mm length and assuming linear elasticity. As illustrated in Fig. 19, the guidewire had a flexible tip, which was modeled with a gradually decreasing elastic modulus. More precisely, it was divided into three parts, and the following values of stiffness were applied, respectively: 1, 10, and 50 GPa[133]. A rigid introducer was included to avoid undesired movements of the guidewire outside the vessel. For the sake of simplicity, henceforth, the baseline finite element case will be denoted as baseline.k.

The insertion of the stiff guidewire in the left iliac artery was simulated by imposing a velocity curve to the most distal node of the guidewire as proposed by Gindre *et al.*[133]. Previous works[133,56] have shown that the simulation results are not sensitive to the insertion speed. Thus, to minimize simulation time, insertion was performed at an insertion speed of 500 mm/s, with a duration of insertion equal to 1.2 s. The nodes of the proximal and distal endings of the vessel were fixed. An Automatic Beams to Surface contact algorithm, based on soft constraint penalty formulation, was applied between the guidewire and the vessel. The adopted numerical high-fidelity model was previously validated against in-vitro experiments that replicated the EVAR procedure[56].

2.4.2 Study II: Mechanical and Clinical Parameterization

The above-described FE model was mechanically and clinically parameterized through in-house written Python scripts. The term ‘mechanically’ is used here to denote the material properties of the aortic tissue and the guidewire, whereas the term ‘clinically’ is employed to signify the clinicians’ preferred insertion orientation.

Initially, the aortic elasticity was selected as a critical parameter due to its pivotal role in determining the vessel’s flexibility during endovascular interventions. Furthermore, this parameter exhibits substantial variability among patients. Upon literature review[134], we decided to explore the range of aortic elasticity, E_{aorta} between [0.8 – 3] MPa, considering a population of aneurysmatic subjects.

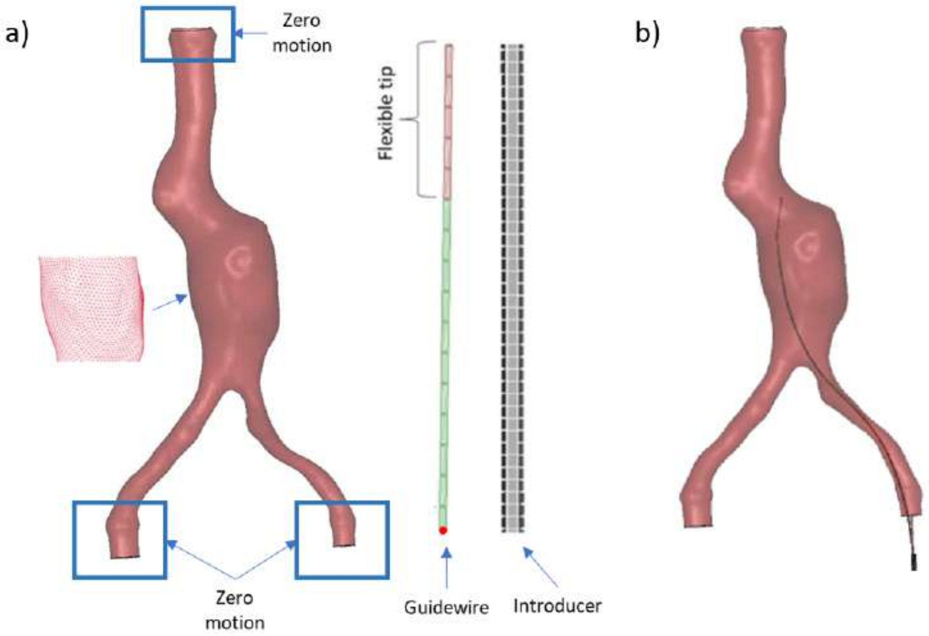

Figure 19: Illustration of the FE set-up: a) depiction of the adopted aortic structure with constrained motion on its extremes, guidewire, and introducer models. The guidewire is inserted in the introducer to reduce undesired movements. b) EVAR snapshot in which the guidewire is developed through the left iliac artery.

The stiffness of a guidewire plays also a crucial factor in determining the effectiveness of EVAR. For example, a very stiff guidewire may lead to vessel damage whereas a rather soft one could hinder the navigation through tortuous vessels. Taking this into consideration, we investigated the effect of the Young's Modulus of the guidewire, E_{wire} in the range of 60 to 200 GPa. This range corresponds to the softest and the stiffest commercial guidewire types available in the market: Amplatz Super Stiff (Boston Scientific) and Lunderquist Extra Stiff (Cook Medical), respectively[135,54]. For enabling the automated tunning of the mechanical parameters, i.e. E_{aorta}, E_{wire}, we developed a Python code, i.e. `mechanical.py`, which changed the baseline case according to user's input values.

Finally, we introduced two guidewire insertion angles, i.e. ϕ and θ, on the sagittal and the frontal view accordingly, as shown in Fig. 20. Our aim was to reproduce the insertion orientation adopted by each clinician. The spans of ϕ and θ were ranging between [-25 – 0]° and [0 –20]°, accordingly. These values respected the given anatomical boundaries and tools' maneuverability, i.e., the presence of the spine, the supine position of the patient, and the access from the femoral artery. In practice, to perform changes in angles ϕ, θ, we rotated the guidewire nodes around the y and

z axis, presented in Fig. 20, through a developed Python code, called `clinical.py`. Further details on the investigated parameters and their corresponding ranges are reported in Table 4.

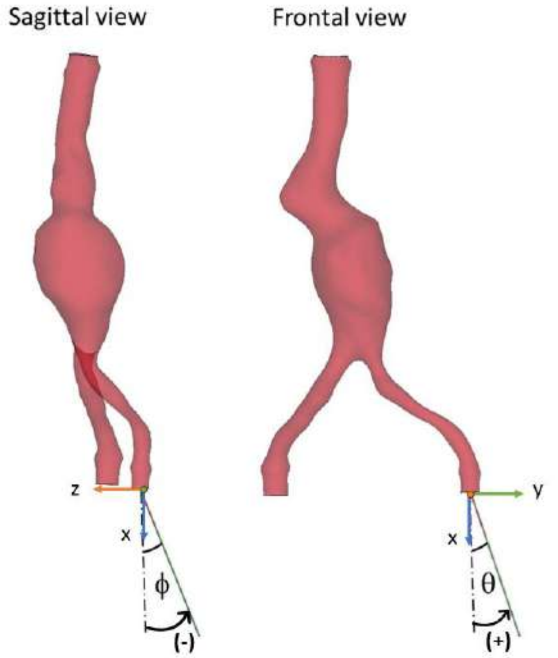

Figure 20: Detail of the insertion angles ϕ and θ in the sagittal and frontal views, respectively. Definition of the local coordinate system used for the nodes' rotation.

Parameter	Description	Range
E_{aorta}	Young's Modulus of aorta	[0.8 – 3] MPa
E_{wire}	Young's Modulus of guidewire	[60 – 200] GPa
ϕ	insertion angle - saggital plane	[-25 – 0]°
θ	insertion angle - frontal plane	[0 – 20]°

Table 4: Range of the mechanical and clinical explored parameters of the FE model

2.5 Radial basis functions - Morphological Parameterization

2.5.1 RBF Background

Radial basis functions consist of a powerful mathematical tool for interpolating data which has further proven to be reliable and accurate in the mesh morphing of a discretized computational model's domain[136]. The mesh morphing action is performed by imposing a desired displacement on a set of points, named source points. Then, a displacement field is interpolated and applied to the nodes of the computational model, named target points. The interpolation result depends on the selection of the radial function and on the type of support (local or global) that it offers. The nucleus of the RBF theory is based on the calculation of unknown weight functions and polynomial terms from known data (displacement at source points in case of mesh morphing). The RBF approach can be applied to multidimensional problems as well[137,138].

The general form of the interpolation function consists of a radial basis and a polynomial term, as shown in equation 7:

$$s(\mathbf{x}) = \sum_{i=1}^{N} \gamma_i \phi(||\mathbf{x} - \mathbf{x}_{ki}||) + h(\mathbf{x}). \tag{7}$$

The scalar function $s(\mathbf{x})$ is defined for each arbitrary point in space $\mathbf{x}$ and represents the point's displacement after the morphing action. The movement of a point can be considered as the aggregation of its interactions with all the source points $\mathbf{x}_{ki}$. This is known as the Euclidean distance between source $\mathbf{x}_{ki}$ and target points $\mathbf{x}$ multiplied by the radial function ϕ and the coefficient γ_i. The additional polynomial factor $h(\mathbf{x})$ is introduced to guarantee the existence and the uniqueness of the solution.

The linear system becomes solvable with the fulfillment of a desired displacement, $\mathbf{g_i}$, at the source points and the implementation of the orthogonality conditions:

$$s(\mathbf{x}_{ki}) = \mathbf{g_i}, \quad 1 \leq i \leq N \; and \; \sum_{i=1}^{N} \gamma_i h(\mathbf{x}_{ki}) = 0. \tag{8}$$

According to Micchelli[139], a unique interpolation polynomial exists if the basis function is a conditionally positive definite function. Assuming that the basis functions are conditionally positive definite of order $m \leq 2$, the linear polynomial can be expressed in 3D space as follows:

$$h(\mathbf{x}) = \beta_1 + \beta_2 x + \beta_3 y + \beta_4 z. \tag{9}$$

The weights of the linear polynomial of equation 9, β_i, are calculated such that the given value at the source points $\mathbf{x}_{ki}$ can be retrieved exactly. It is crucial to underline that mesh morphing is obtained through a vector field displacement, while RBF are scalar functions. Therefore, the interpolation of a 3D set of displacement at source points can be performed using the following equations:

$$s_x(\mathbf{x}) = \sum_{i=1}^{N} \gamma_i^x \phi(\mathbf{x} - \mathbf{x}_{ki}) + \beta_1^x + \beta_2^x x + \beta_3^x y + \beta_4^x z. \tag{10}$$

$$s_y(\mathbf{x}) = \sum_{i=1}^{N} \gamma_i^y \phi(\mathbf{x} - \mathbf{x}_{ki}) + \beta_1^y + \beta_2^y x + \beta_3^x y + \beta_4^y z. \tag{11}$$

$$s_z(\mathbf{x}) = \sum_{i=1}^{N} \gamma_i^z \phi(\mathbf{x} - \mathbf{x}_{ki}) + \beta_1^z + \beta_2^z x + \beta_3^z y + \beta_4^z z. \tag{12}$$

The morphing action can be restricted in the space by establishing a domain beyond which the mesh remains unaltered.

RBF techniques are gaining more and more ground in the Computer-Aided Engineering (CAE) field. Their application has already spread in the automotive[140], naval[141], aeronautical[142], energy[143], and medical field[144,145]. Their main advantage is their potential to morph the mesh without changing its topology or its consistency while retaining disk usage at low levels. Thanks to this feature, the time consuming re-meshing process can be avoided. RBF-based mesh morphing allows for precise control of the source points' final position while at the same time preserving a high degree of mesh quality.

2.5.2 Study I

The RBF Morph (www.rbf-morph.com) software program was employed to mold the configuration of the shunt, using the baseline mesh, as described in section 2.3.1.1, as a starting point. Initially, we ensured that baseline mesh was characterized by good quality to restrict the mesh deterioration post morphing. As already explained in section 2.5.1, we strategically selected some source points. The source points , $\mathbf{x}_{ki}$, were organized into four sets on the implant's district, as depicted in Fig. 21a,b. The morphing action was constrained inside the borders of the blue cylinder indicated in Fig. 21a, called domain. The four different sets of source points were generated and placed in:

- the inferior boundary of the shunt's geometry (ISP)

- the central segment of the shunt, corresponding to the maximum cross-sectional diameter (DSP)
- the cylindrical periphery of the shunt's geometry (CSP)
- the superior boundary of the shunt's geometry (SSP)

Adhering to the clinicians' needs, twelve RBF transformations were introduced to cover the wide spectrum of possible shunt configurations. The shunt's geometry was modified by imposing linear translation and rotation to its upper, central, and lower section. The combination of all the RBF modifiers enabled the creation of complex shunt configurations. For the determination of the RBF modifiers, a local coordinate reference system (LCRS) was defined. The LCRS was placed on the shunt's cross-section centerline (Fig. 21b).

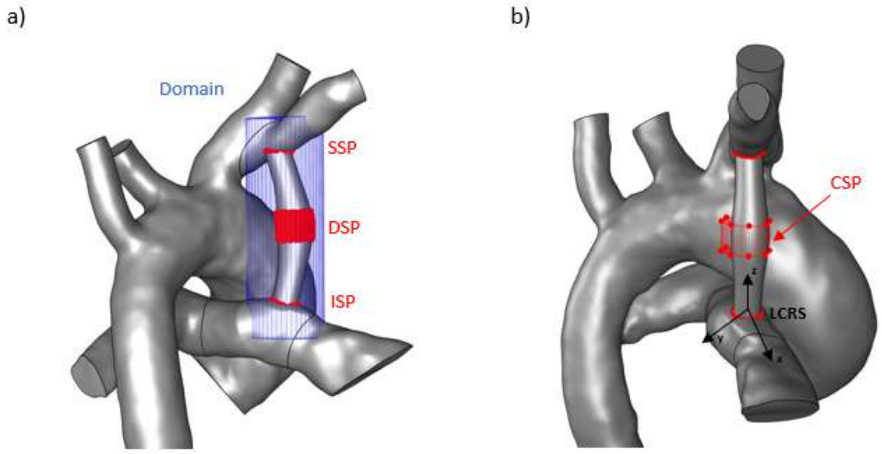

Figure 21: Illustration of the source points on the superior, middle, and lower part of the shunt, i.e. SSP, DSP, and ISP sets respectively. The source points are used for driving the morphing action. Blue colored cylindrical morphing domain a), CSP source point set in the periphery of the shunt with the local coordinate reference system (LCRS) b).

The center line of the implant was defined according to Biancolini *et al.*[146]. The setup of each modifier was built by activating a group of source points subjected to a predefined motion. The action of each modifier and its source points' motion are reported below:

- dl-1-vol—Rigid motion of ISP along the ±x direction: sliding of the shunt's root along the length of the pulmonary artery (Fig. 22a).

- dl-2-vol—Rigid motion of SSP along the ±x direction: sliding of the shunt's top segment along the length of the right subclavian artery (Fig. 22b).
- dr-1-vol—Rigid motion of ISP along the ±y direction: sliding of the shunt's root along the width of the pulmonary artery (Fig. 22c).
- dr-2-vol—Rigid motion of SSP along the ±y direction: sliding of the shunt's top segment along the width of the right subclavian artery (Fig. 22d).
- mid-dl-vol2—Rigid motion of DSP along ±x direction: inflation or deflation towards the ±x axis (Fig. 22e).
- mid-dl-vol—Rigid motion of CSP along ±x direction: inflation or deflation towards the ±x axis (Fig. 22f).
- mid-dr-vol2—Rigid motion of DSP along ±y direction: inflation or deflation towards the ±y axis (Fig. 22g).
- mid-dr-vol—Rigid motion of CSP along ±y direction: inflation or deflation towards the ±y axis (Fig. 22h).
- rl-1-vol—Rotation of ISP with respect to the y axis of LCRS: the shunt's root, which is located on pulmonary boundary, is revealed or hidden on the zx plane (Fig. 22i).
- rl-2-vol—Rotation of SSP with respect to the y axis of LCRS: the shunt's upper segment which is located on the right subclavian aortic boundary, is revealed or hidden on the zx plane (Fig. 22j).
- rr-1-vol—Rotation of ISP with respect to the x axis of LCRS: the shunt's root is revealed or hidden on the yx plane (Fig. 22k).
- rr-2-vol—Rotation of SSP with respect to the x axis of LCRS: the shunt's upper segment is revealed or hidden on the yx plane (Fig. 22l).

The shape factors were employed by using amplification factors to determine the extent of their influence on the morphology of the MBTS. The amplification factor of the dl-1-vol, dl-2-vol, mid-dl-vol, mid-dl-vol2, mid-dr-vol, and mid-dr-vol2 ranged between -0.5 and 0.5, whereas the range of the rest of the shape parameters was modified between −5 and 5. The action of each shape parameter is showcased in Fig. 22, where the maximum and minimum effect of each modifier is displayed.

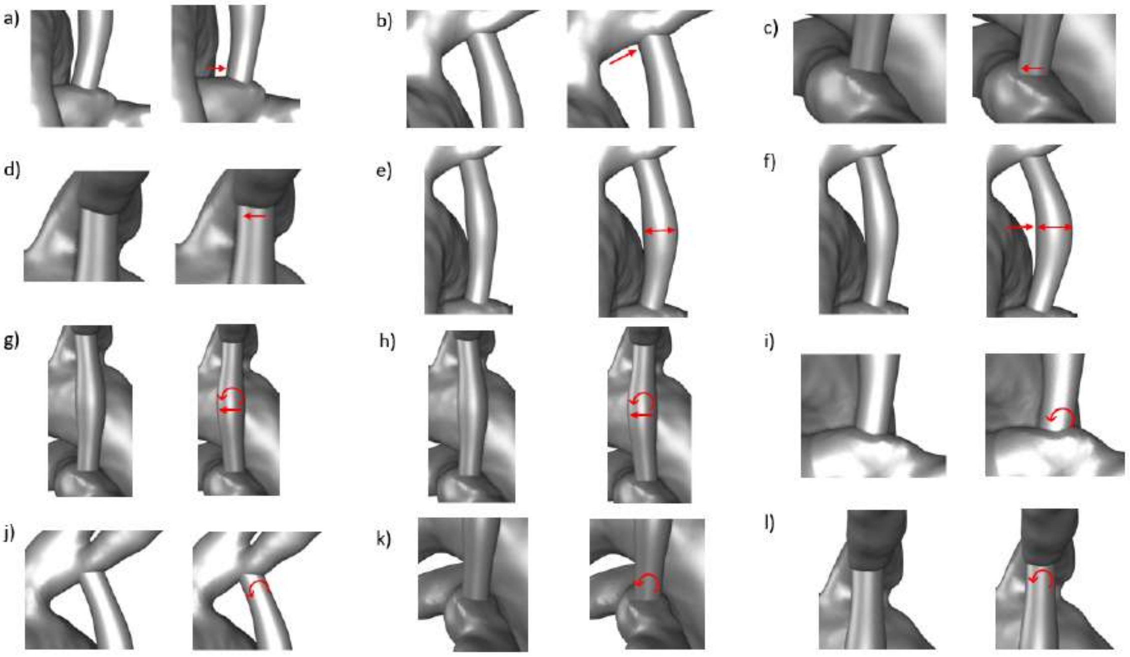

Figure 22: Morphing effect of the twelve RBF shape modifiers: dl-1-vol (**a**); dl-2-vol (**b**); dr-1-vol (**c**); dr-2-vol (**d**); mid-dl-vol2 (**e**); mid-dl-vol (**f**); mid-dr-vol2 (**g**); mid-dr-vol (**h**); rl-1-vol (**i**); rl-2-vol (**j**); rr-1-vol (**k**); rr-2-vol (**l**).

For morphing the shunt as a combination of the twelve modifiers, the mesh was modified successively according to the amplification factor that was imposed on each shape modifier. This sequence of mesh morphing actions induced the risk of mesh quality deterioration. To control this hazard, the maximum mesh cell squish was monitored after each morphing action.

2.5.3 Study II

In the context of the EVAR study, the morphological parameterization of the aortic geometry was performed with the Python version of the RBF Morph software. This software allowed us to rapidly generate new configurations of the baseline abdominal aorta (Fig. 19). For the mesh morphing of the aortic geometry, we introduced three shape parameters: the supra- and infra-renal neck angles, α and β, defined according to previous works[147,148], and the tortuosity of the left iliac artery, τ. All the considered parameters are depicted in Fig. 23 a).

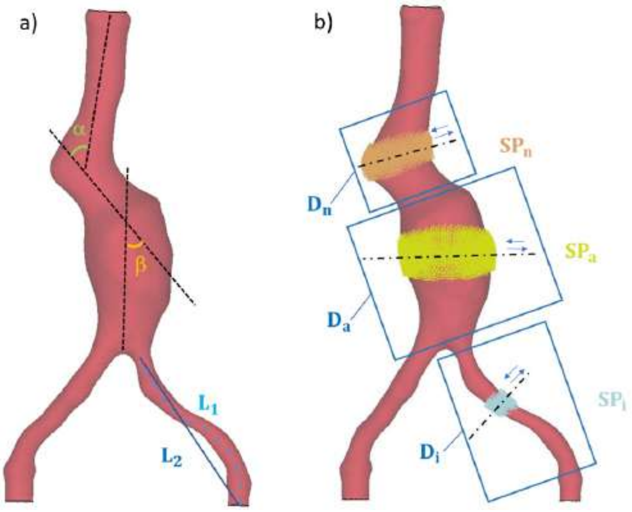

Figure 23: Description of the morphing actions: a) Morphing parameters: α, supra-renal neck angle; β infra-renal neck angle; L_1 and L_2 that are respectively the length of the left iliac artery and the Euclidean distance between its ending points, these lengths are used to calculate the tortuosity of the iliac artery, τ, according to equation 13. b) Set of source points SP_n, SP_a and SP_i, with the corresponding domains D_n, D_a and D_i. The black dotted lines indicate the direction of translations imposed on each set of source points. c) Example of morphed geometry (wire-frame), overlaid onto the original geometry shown in transparency.

The tortuosity of the iliac artery was defined as follows[149]:

$$\tau = \frac{L_1}{L_2} - 1, \tag{13}$$

where L_1 and L_2 are respectively the length of the left iliac artery and the Euclidean distance between its ending points. In this study, solely the tortuosity of the left iliac artery was considered because we hypothesized that this was the side of insertion.

To perform shape changes, three different sets of source points SP_n, SP_a and SP_i, shown in Fig. 23 (b), were generated using LS-PrePost processor:

- SP_n, located in the neck region
- SP_a, placed in the middle part of the aneurysm, e.g. aortic bulge.
- SP_i, positioned in the middle of the left iliac artery.

For changing angle, α, we translated the source points SP_n in the direction of the black dotted line, as the arrows of Fig. 23b indicate. All the nodes within the domain D_n were displaced according to the interpolating equation 7. The nodes outside the domain borders were not affected by the morphing action. A similar procedure was performed for angle, β, and tortuosity τ using the source points SP_a, SP_i and restricting the morphing inside the domains D_a and D_i accordingly. We chose the domains of the three shape modifiers such that they do not overlap, to keep the morphing process simple. An example of the output of the morphing action is depicted in Fig. 23c. As already mentioned, the morphing procedure was achieved by coding in Python, using the RBF Morph libraries. The developed code, i.e. `morphological.py`, was able to change the values of the morphological parameters α, β, and τ according to the user-defined displacement on the source points SP_n, SP_a and SP_i.

Regarding the range of the aortic shape modifiers, we chose values to capture reasonable morphological variations that have clinical meaning. In Table 5, the investigated spectrum of each shape modifier is reported. The selection of the parameters was driven by literature data. Severe supra- and infra-renal neck angulation, i.e. α and β greater than 60°, are associated with increasing risk of post-operative complications, such as type 1A endoleaks[147,150]. High values of iliac tortuosity, τ, are correlated with increasing levels of deformations and more challenging procedures[46].

Parameter	Description	Range
α	supra-renal neck angle	$[30 - 55]^\circ$
β	infra-renal neck angle	$[25 - 60]^\circ$
τ	tortuosity of left iliac	$[0.09 - 0.15]$

Table 5: Range of the morphological parameters of the examined FE parametric model

The combination of the selected morphing parameters enabled us to explore a broad spectrum of possible aortic configurations. In this way, we were able to construct hypothetical patient configurations and run simulations on them. The time needed for each morphing action was equal to 0.1 s, i.e. instantaneous software response.

Finally, we performed a control on the mesh quality after the application of the most radical morphing actions. The mesh was evaluated in terms of skewness and

Jacobian ratio. Our results showed that the mesh deterioration was very low, i.e. negligible. More precisely, the skewness was kept below 0.8 and the Jacobian ratio was above 0.15 for all the mesh elements. This was expected as the morphing was applied only on a surface mesh, which is more tolerant to changes compared to a volume mesh.

2.6 Reduced Order Modeling

In this part, the reduced order modeling technique is analyzed. Initially, the ROM theoretical background is introduced and then the hands-on ROM creation procedure is explained for both studies I and II.

2.6.1 ROM Background

A Reduced Order Model (ROM) is a simplified mathematical representation of a complex system or process that captures its essential behavior while significantly reducing the computational cost and complexity associated with modeling and simulation[151]. The principal idea behind ROM is that a generic problem has an intrinsic dimension much lower than the number of degrees of freedom of the discretized system. There are mainly two distinct approaches in ROM generation: the model-based and the data-driven[152]. Their difference is that the first builds a mathematical model of the system, typically represented by differential equations or state-space formulations, whereas the second generates a model based on observed data or simulation data, without explicit knowledge of the underlying mathematical model. In this study, the latter method is adopted and described.

Before delving into the ROM construction, it is crucial to outline the methodology employed for obtaining the necessary 3D parametric simulation data. In Fig. 24, the main steps for acquiring the ROM input data are described. According to this diagram, initially, the baseline problem is parameterized. While there is no restriction on the number of chosen parameters, it is recommended to keep this number as low as possible to save computational power. The parameters should always be independent from one another. What is more, the range of the adopted parameters is defined. Afterwards, we generate a Design of Experiments (DOE) table. A DOE is a list of several possible parameter combinations, called scenarios[153,154]. The selection of a DOE technique is pivotal because it determines the scenarios' distribution in the desired exploration space, hence the quality of the produced data. Once the DOE is set, we launch the corresponding simulation serially or in parallel on the workstation. The results' calculation typically requires substantial computational resources and takes hours or days to be finished. Since a data-driven, i.e., blind to the differential equations, ROM approach is adopted, a wide database of high-fidelity solutions is required. Finally, in various software used for ROM build-up, including Ansys® Twin Builder, it is necessary to convert the simulation data into a snapshot form. Snapshots adhere to some specific format rules, which should be respected.

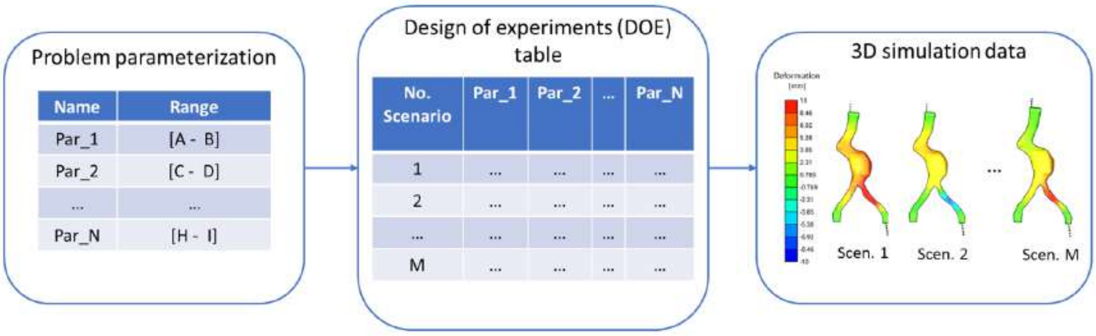

Name	Range
Par_1	[A - B]
Par_2	[C - D]
...	...
Par_N	[H - I]

No. Scenario	Par_1	Par_2	...	Par_N
1	...	...	...	...
2	...	...	...	...
...	...	...	...	...
M	...	...	...	...

Figure 24: Illustration of the main steps for generating the 3D parametric simulation data, used as input for the ROM training and validation: problem parameterization (step 1), generation of a design of experiments table (DOE) (step 2), calculation of the simulation results (step 3).

After completing the generation of parametric data, we proceed with the ROM creation. In Fig. 25, the main blocks of this procedure are presented. The first part of constructing a ROM consists of building a basis of vectors representative of any field solution within the design space. For this purpose, the snapshots are compressed into a smaller set of modes using Singular Value Decomposition (SVD). In further detail, the SVD theorem decomposes a matrix $\mathbf{A}$ into three components:

$$\mathbf{A} = \mathbf{U}\mathbf{S}\mathbf{V}^{\mathrm{T}}, \tag{14}$$

where $\mathbf{U}$ represents the left singular vectors, $\mathbf{S}$ the singular values, and $\mathbf{V}^{\mathrm{T}}$ the right singular vectors[155]. $\mathbf{U}$, $\mathbf{S}$ and $\mathbf{V}^{\mathrm{T}}$ represent the spatial components, the significance of each mode, and the temporal components, respectively[156].

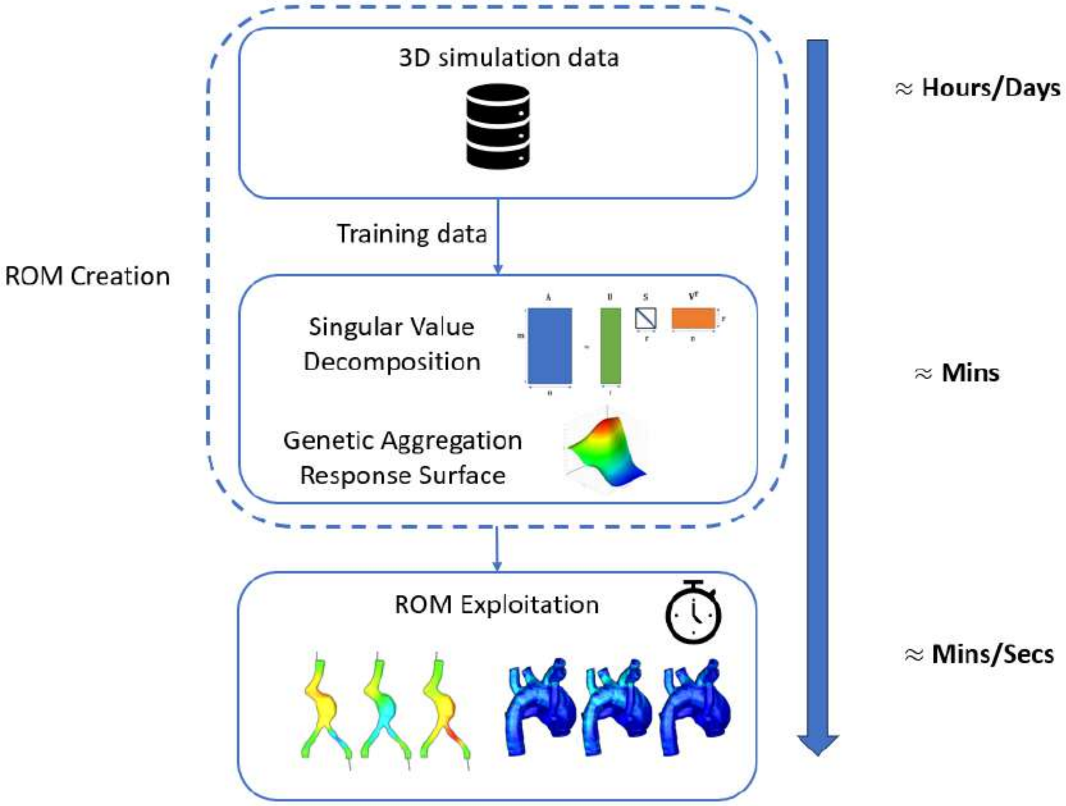

Figure 25: Description of the main steps of the ROM workflow with the estimation of the time needed for the completion of each step.

The singular values in the diagonal matrix $\mathbf{S}$ are arranged in descending order. By exploiting this mathematical property, the matrix $\mathbf{A}$, which contains all the training data, can be approximated by a linear combination of the first r left singular vectors i.e. $\mathbf{U}_i^*$ with $i = 0, r$. The vectors included in $\mathbf{U}^*$ are referred to as modes.

The accuracy of the approximated matrix $\mathbf{A}^*$ depends on the number of r left singular vectors, i.e., increasing the number of r lowers the error tolerance. The approximated matrix $\mathbf{A}_r^*$ in the basis or r modes is given by the following equation:

$$\mathbf{A}_r^* = \mathbf{U}_r^* \, \mathbf{S}_r^* \, \mathbf{V}_r^{\mathrm{T}*} = \mathbf{U}_r^* \, \mathbf{C}. \tag{15}$$

$$\mathbf{C} = [\alpha_1, \alpha_2, \ldots, \alpha_r], \tag{16}$$

where $\mathbf{C}$ is called the mode coefficient matrix and α_i are the mode coefficients.

By definition, the basis of the r modes is the optimal basis of rank r to approximate $\mathbf{A}$. In order to measure the error of the approximated $\mathbf{A}_r^*$, we introduce the percentage reduction relative root mean square RMS error:

$$e_{\text{red}}^{\text{RMS}} = \frac{\|\mathbf{A} - \mathbf{A}_r^*\|}{\|\mathbf{A}\|} \tag{17}$$

Following the diagram of Fig. 25, the second stage of ROM construction is focused on the generation of the response surface (RS) of the mode coefficients α_i with $i = 0, r$. This is performed via interpolating between the known mode coefficient data of the learning snapshots, $\alpha_{p,i}$. As graphically shown in Fig. 26, the response surface is reconstructed based on the $\alpha_{p,i}$ data with $p = 0, N$, where N is the total number of learning snapshots. In the context of Ansys® Twin Builder, and for performing this task, the Genetic Aggregation Response Surface (GARS) technique is employed[157]. The GARS finds the best possible RS based on the selected design of experiments by combining metamodels, settings, kernel variation, and polynomial regression. What is more, a fitness factor is employed to minimize errors, including cross-validation errors.

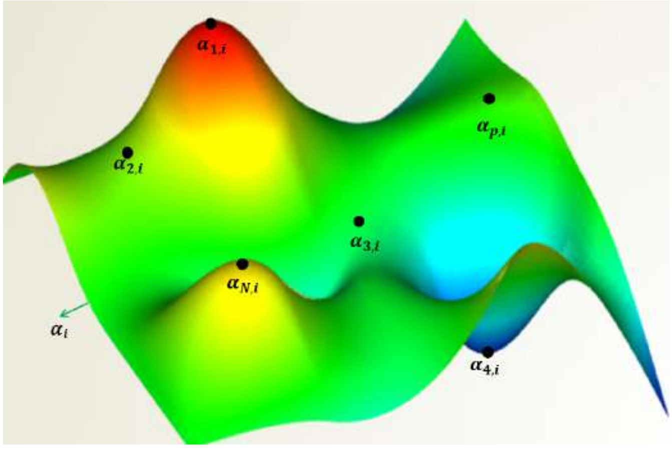

Figure 26: Response Surface generation for every mode coefficient α_i based on known mode coefficients of the learning snapshots, $\alpha_{p,i}$

Finally, the ROM solution of each new input data set can be linearly expressed through equation 18. The variable $\mathbf{v}(\mathbf{p})$ of a selected point $\mathbf{p}(x, y, z)$ is calculated as the accumulation of the product of the mode coefficient α_i and the mode $\mathbf{U}_\mathbf{i}^*$ for the total number of selected modes, r:

$$\mathbf{v}(\mathbf{p}) = \sum_{i=1}^{r} \alpha_i(\mathbf{p})\, \mathrm{U}_i^*(\mathbf{p}). \tag{18}$$

The process of building up a ROM in the Twin Builder environment, i.e. data reduction with SVD and mode coefficient calculation, takes usually some minutes. Then, the ROM exploitation is performed with the use of solvers and standalone systems in almost real-time.

As it appears from the above-described ROM build-up theory, the prediction of the variable of interest, $\mathbf{v}(\mathbf{p})$, on a specific design point $\mathbf{p}$, includes two different errors. The first derives from the data reduction via SVD algorithm, i.e. the approximation of $\mathbf{A}$ in the basis $\mathbf{U}^*$. The second is triggered from the calculation of the RS of the mode coefficients with GARS algorithm, i.e. α_i. A visual representation of the ROM-induced errors is offered in Fig. 27. In this figure, the exact solver solution is stated as $\mathbf{v}_{\text{ref}}$, the solution after the data reduction is named as $\mathbf{v}_{\text{proj}}$ and the final ROM prediction is named as $\mathbf{v}_{\text{rom}}$.

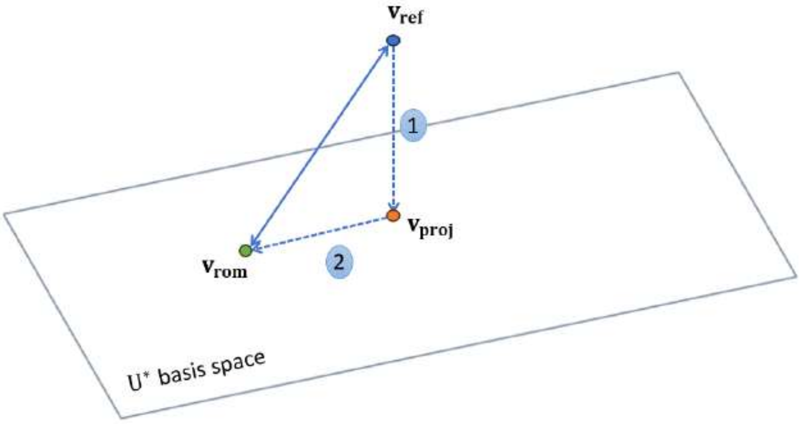

Figure 27: Description of the two ROM-induced errors: the first derives from the SVD procedure, i.e. transitioning from the exact solver solution $\mathbf{v}_{ref}$ (blue point) to the post SVD solution $\mathbf{v}_{proj}$ (orange point). The second is caused by the GARS interpolation, i.e. shifting from the post SVD solution $\mathbf{v}_{proj}$ (orange point) to the final ROM prediction $\mathbf{v}_{rom}$ (green point).

Based on these variables, the following ROM evaluation indices are introduced for every design point: the relative reduction and ROM errors, $e^{\text{rel}}_{\text{red}}$ and $e^{\text{rel}}_{\text{ROM}}$, respectively, and the absolute reduction and ROM errors, $e^{\text{abs}}_{\text{red}}$ and $e^{\text{abs}}_{\text{ROM}}$, respectively.

$$e_{\text{red}}^{\text{rel}} = \frac{\|\mathbf{v}_{\text{ref}} - \mathbf{v}_{\text{proj}}\|}{\|\mathbf{v}_{\text{ref}}\|}, \tag{19}$$

$$e_{\text{ROM}}^{\text{rel}} = \frac{\|\mathbf{v}_{\text{ref}} - \mathbf{v}_{\text{rom}}\|}{\|\mathbf{v}_{\text{ref}}\|}, \tag{20}$$

$$e_{\text{red}}^{\text{abs}} = max(\mathbf{v}_{\text{ref}} - \mathbf{v}_{\text{proj}}), \tag{21}$$

$$e_{\text{ROM}}^{\text{abs}} = max(\mathbf{v}_{\text{ref}} - \mathbf{v}_{\text{rom}}). \tag{22}$$

Finally, the building of a ROM is a dynamic procedure in which the user should experiment with the ratio and the selection of training and validation data. In general, a ROM is considered successful when it estimates the variable of interest from input combinations that are not included in the training set with sufficient precision.

2.6.2 Study I

In this section, the ROM set-up of the study I, i.e. MBTS work, is reported. As already analyzed in section 2.5.2, the MBTS model was parametrized with twelve different RBF shape modifiers. Based on the range of these modifiers, we created a DOE table including 150 scenarios. The scenarios' generation was performed in a systemic way, employing the Optimal Space Filling algorithm of Ansys® DesignXplorer, Release 22R1. This algorithm guarantees the optimal spatial allocation of the investigated scenarios in the design space.

Once the DOE was set up, we wrote a script in Fluent scheme language that performed the morphing of the shunt according to the values of each scenario of the DOE table. Finally, before running the parametric simulations, we selected the output variables of interest, i.e. $\mathbf{v}$ as defined in equation 18, which in our case were the volume velocity, the wall pressure, and WSS of the whole model. The results were exported directly in the format of snapshots, therefore no postprocessing was needed. The entire computational part was performed on a workstation equipped with two Intel Xeon 3.00 GHz processors, exploiting 14 cores from each of them and 256 GB of shared RAM. The snapshots' generation took approximately 20 hours.

Afterwards, snapshots were imported in ROM Builder (Ansys® Electronics, Release 22R1). As previously described, part of them was used for feeding the reduction algorithm. We performed data reduction using several different sizes of training datasets. Our objective was to determine the optimal size of the training dataset, which would give us the desired reduction precision. The reduction threshold error, i.e. $e^{\mathrm{RMS}}_{\mathrm{red}}$, was selected for each ROM individually depending on its complexity. In tables 6, 7, and 8, a sensitivity study on the reduction error, $e^{\mathrm{RMS}}_{\mathrm{red}}$, as a function of the size of the training dataset is reported for the pressure, velocity, and WSS ROM. The corresponding number of modes, r, is also presented.

Pressure ROM

Size of training dataset	$e^{\mathrm{RMS}}_{\mathrm{red}}$ (%)	Number of modes r
50	0.354	12
70	0.295	16
85	0.269	19
100	0.244	22
120	0.205	27

Table 6: Sensitivity study on the reduction-induced error, $e^{\mathrm{RMS}}_{\mathrm{red}}$, as a function of the size of the training dataset for the pressure ROM

Velocity ROM

Size of training dataset	$e^{\mathrm{RMS}}_{\mathrm{red}}$ (%)	Number of modes r
50	9.389	11
70	8.917	12
85	8.416	14
100	8.136	16
120	7.424	18

Table 7: Sensitivity study on the reduction-induced error, $e^{\mathrm{RMS}}_{\mathrm{red}}$, as a function of the size of the training dataset for the velocity ROM

As vividly depicted in the tables, the percentage of reduction error of pressure ROM is substantially lower than the one of velocity and WSS. This happens because

WSS ROM

Size of training dataset	$e_{\text{red}}^{\text{RMS}}$ (%)	Number of modes r
50	8.878	9
70	7.82	12
85	6.924	16
100	6.679	18
120	6.01	22

Table 8: Sensitivity study on the reduction-induced error, $e_{\text{red}}^{\text{RMS}}$, as a function of the size of the training dataset for the WSS ROM

the pressure on the cardiovascular wall does not change drastically for the various explored MBTS configurations. Another significant remark is that the pressure and WSS ROM predict solely surface values whereas the velocity ROM is calculated for the whole internal volume. This makes the latter ROM much more prone to higher SVD reduction errors by default. Finally, we can see that the magnitude of the SVD error is particularly high for small sizes of training data, i.e. 50 and 70, for both the velocity and WSS ROM. This indicates that the blood flow complexity cannot be captured with so few learning data.

Taking into consideration the data reduction sensitivity results, we decided to opt for high accuracy by using 120 scenarios as learning data for all ROMs. Therefore, the number of chosen modes, r, for ROM build-up was 27 for the pressure, 18 for the velocity, and 22 for the WSS evaluation (Table 6, 7, 8). The remaining 30 snapshots were subtracted from the available dataset and were used for the ROM verification. The validation data were selected based on an optimal distribution algorithm to avoid results bias.

2.6.3 Study II

In the context of the study II, i.e. EVAR on AAA patients, to acquire the ROM model, we had to feed the ROM Builder with parametric FE simulation results. In Fig. 28, the procedure for obtaining the ROM snapshots is demonstrated by showcasing its main steps. Starting from the baseline FE case, we generated a DOE table varying the range of the seven mechanical, clinical, and morphological parameters, analyzed in sections 2.4.2 and 2.5.3. Similarly to study I, we used the Optimal Space Filling algorithm, since exploring uniformly the design space was necessary. The generated DOE table consisted of 300 scenarios. Then a shell script was written to modify successively the FE baseline case, i.e. baseline.k, according to the scenario-specified parameter values using mechanical.py, clinical.py, and morphological.py for the mechanical, clinical, and morphological modifiers respectively. At the end of this procedure, the corresponding LS-DYNA simulations were launched.

The entire computational part was performed using 240 cores (Intel Xeon Gold 6152 CPU @2.10 GHz) in task parallelism mode. We opted for task parallelism because individual simulations were independent. After conducting a scalability analysis of the high-fidelity FE simulation, we found out that using 4 cores leads to the minimum computational time which was around 25 minutes. Thus, we conducted 5 sets of 60 concurrent simulations, which lasted 125 minutes in total.

The typical output of the FE simulation was a text file, i.e. nodout.k, which contained the values of several important parameters such as velocity, displacement, spatial coordinates, and acceleration of each node at the final timestep. In contrast with the MBTS ROM build-up procedure, there was no direct coupling between the FE solver and the ROM builder. For this reason, we had to develop a custom pipeline, i.e. python scripts, for exporting the variables of interest and converting them into binary snapshots, i.e. snapshot.bin. For this study, the selected variables of interest, $\mathbf{v}$ as defined in equation 18, were the nodal displacement and the nodal position, since we wanted to predict the final configuration of the aorta after the full insertion of the stiff guidewire.

Theoretically, we could have selected one of those variables, either nodal displacement or nodal position since we could calculate the other one using the known initial nodal position in the baseline case. However, our purpose was the generation of a ROM that predicts the nodal displacement and at the same time, it allows the visualization of the final aortic configuration. Having both pieces of information within the same tool could prove beneficial for clinicians' decision-making process pre and intra operatively. In terms of ROM terminology, the ROM built for the nodal displacement is called physical ROM while the ROM built for the nodal position is named as geometrical ROM. These two ROMs are superimposed: the

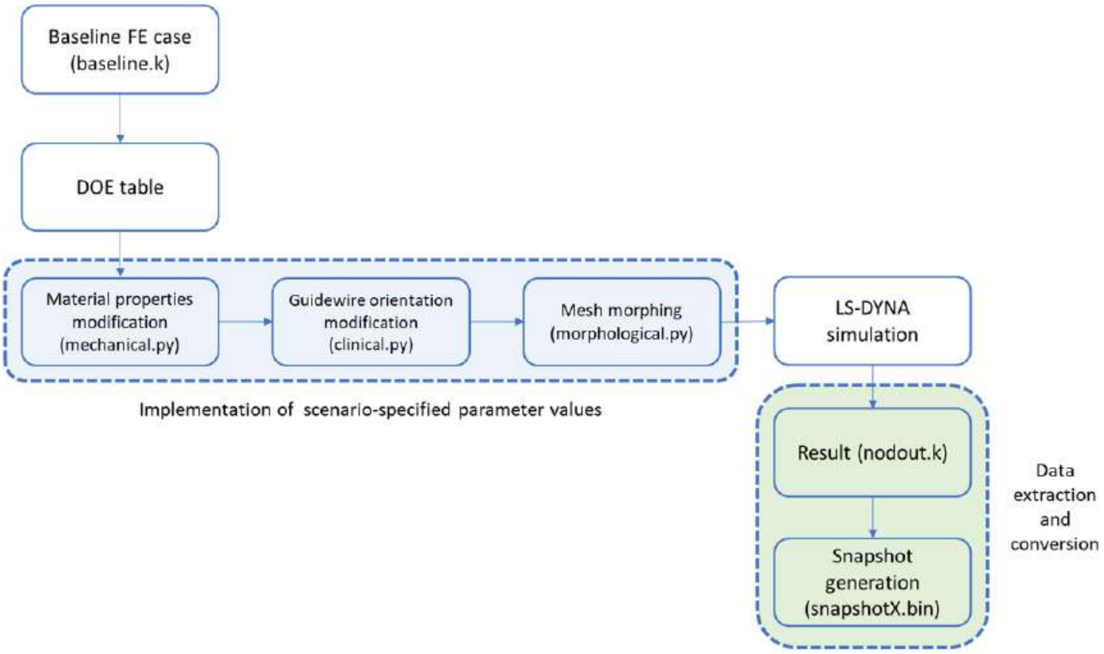

Figure 28: Description of the main steps of the ROM workflow of EVAR study: implementation of scenario-specified parameter values, launching of LS-DYNA simulations, data extraction and conversion to binary snapshot format

geometrical ROM determines the aortic configuration shown in the Graphical User Interface (GUI) display area and the values of the physical ROM, i.e. displacement predictions, are projected on the corresponding nodes.

Once we acquired the snapshots of the geometrical and physical ROM, we fed them individually to the SVD algorithm. In tables 10, 9, the results of the investigation of the appropriate training data size are exhibited.

Nodal Displacement ROM (physical)

Size of training dataset	$e_{\text{red}}^{\text{RMS}}$ (%)	Number of modes r
50	0.504	18
100	0.342	25
150	0.252	33
180	0.225	37
200	0.2	38

Table 9: Sensitivity study on the reduction-induced error, $e_{\text{red}}^{\text{RMS}}$, as a function of the size of the training dataset for the nodal displacement ROM

Based on the presented tables, we chose a training dataset of 200 snapshots

Spatial Position ROM (geometrical)		
Size of training dataset	$e_{\text{red}}^{\text{RMS}}$ (%)	Number of modes r
50	0.012	20
100	0.0048	34
150	0.003	45
180	0.0027	49
200	0.0012	81

Table 10: Sensitivity study on the reduction-induced error, $e_{\text{red}}^{\text{RMS}}$, as a function of the size of the training dataset for the spatial position ROM

for both the nodal displacement and spatial position ROM. Their corresponding percentage reduction error, $e_{\text{red}}^{\text{RMS}}$, was equal to 0.2% and 0.0012%. According to Ansys® Twin Builder theory, these errors are considered to be sufficiently low to obtain an accurate ROM. We note that the ROM reduction errors have a difference of two orders of magnitude. This can be interpreted with equation 17: the physical ROM is normalized with the magnitude of displacement whereas the geometrical with the absolute value of the spatial coordinates. The number of modes, r, for the nodal displacement and spatial position ROM was 38 and 81 respectively. Since the geometrical ROM (i.e. spatial position) is used only for visualization purposes and its reduction error is rather low, we will focus on the physical ROM (i.e. nodal displacement).

Before deciding on the reduction rate, we also considered the graphs of Fig. 29a,b. The Reduction curve (blue) represents the accuracy of snapshot reconstruction with respect to the learning subset while the Leave One Out curve (green) represents this accuracy with respect to snapshots outside the learning set. The curves are given as a function of the training dataset size. As we can see, both curves have a flattening behavior for the selected number of modes (red line) for both the geometrical and the physical ROM. In the case of the reduction curve, this implies that using more modes for the selected size of the training dataset will not substantially enhance the ROM accuracy, $e_{\text{red}}^{\text{RMS}}$. In the case of Leave One Out curve, we find out that there is no benefit in adding more scenarios, which are excluded from the training procedure. Therefore, the chosen ROM set-up could be characterized as optimal for

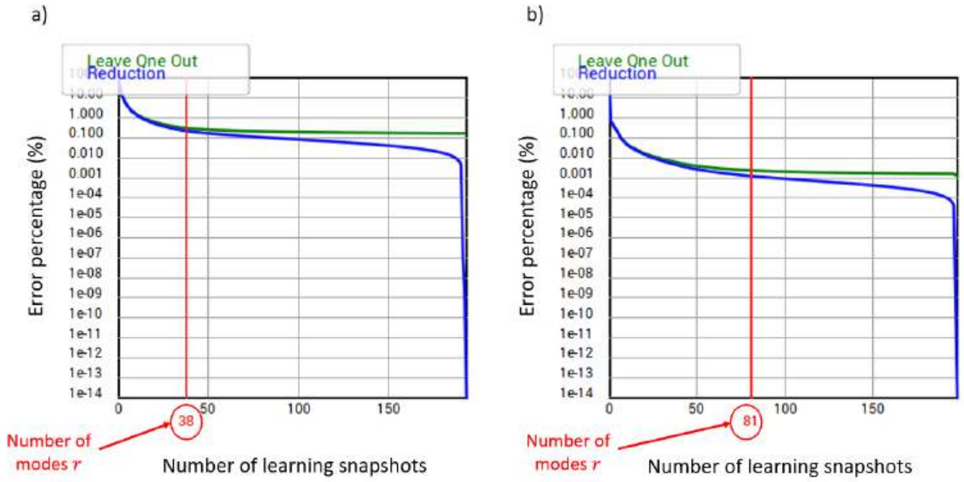

Figure 29: Illustration of the Reduction (blue) and the Leave One Out curve (green) in function of the learning dataset for the physical a) and geometrical b) ROM. The Reduction curve shows the accuracy of snapshot reconstruction with respect to the learning subset, while the Leave One Out with respect to the snapshots outside the learning set. Finally, the red line indicates the optimal selection of the number of modes, r, taking into consideration the above-mentioned curves.

minimizing the error induced by the data reduction for the selected training dataset size.

3 Results

In this section, we present our findings, organized into three distinct subsections to enhance clarity and facilitate comprehension. Firstly, the results of the MBTS work, i.e. study I, are exhibited. Then, the outcomes of generated ROM for EVAR applications, i.e. study II, are showcased. Ultimately, the hemodynamic results of the grafts' work, i.e. study III, are displayed.

3.1 Study I

In this part, the results of the MBTS workflow, which was thoroughly outlined in sections 2.5.2 and 2.6.2 , are presented. In further detail, the results are structured into three subcategories: verification of the RBF mesh morphing, validation of ROM, and hands-on exploitation of the ROM.

3.1.1 RBF Mesh Morphing Verification

Concerning the performance of the mesh morphing technique, Table 11 depicts the setup of the four scenarios linked with the highest mesh degradation. The highest cell squish values among all the morphed meshes as well as the corresponding amplification factors of the shape modifiers are reported. The shape amplification factors close to the range boundaries are shown in bold font within Table 11.

The cell squish index is employed here to quantify the degree to which the cells diverge from orthogonality with respect to their faces. To ensure an acceptable mesh quality, Ansys® Fluent guidelines recommend that the maximum cell squish index remains below 0.99. As presented, the mesh quality is preserved within the studied range of possible shunt configurations for three out of four worst scenarios. The peak cell squish index, i.e. 0.994, is found on three mesh elements of scenario 43.

With regards to the morphing speed, the mesh morphing procedure, including the twelve analyzed shape modifiers, required only one minute per scenario. Related to this, it is worth mentioning that the initial mesh generation took about ten minutes. At the end of the sequence of morphing actions, a mesh preview was offered through

Shape factor	Scenario 23	Scenario 43	Scenario 123	Scenario 142
dl-1-vol	−0.26	**−0.49**	−0.36	−0.39
dl-2-vol	−0.03	−0.27	**0.48**	**−0.46**
dr-1-vol	−0.17	3.30	0.70	−2.23
dr-2-vol	−3.30	0.90	4.23	−0.70
mid-dl-vol2	−0.04	0.30	−0.08	0.34
mid-dl-vol	−0.02	0.18	−0.18	0.14
mid-dr-vol2	**0.48**	−0.36	-0.08	0.34
mid-dr-vol	−0.25	0.24	−0.34	0.05
rl-1-vol	**−4.63**	4.43	−1.83	3.30
rl-2-vol	−2.83	0.57	3.90	2.43
rr-1-vol	−0.57	2.50	−1.37	−3.10
rr-2-vol	**4.77**	−0.37	3.17	−2.37
Cell Squish	0.982	0.994	0.906	0.973

Table 11: Four worst-case scenarios presenting the greatest mesh quality degradation after mesh morphing. The amplification shape factors close to the range boundaries are shown in bold font.

the console almost in real-time (i.e., less than 1s).

3.1.2 ROM Validation

Fig. 30 illustrates the velocity flow field evaluated at the MBTS middle cross-section for the following selected scenarios: No. 135 (a–e), No. 1 (b–f), No. 34 (c–g), and No. 146 (d–h). The full CFD cases, $\mathbf{v}_{\text{ref}}$, and the corresponding ROM solutions, $\mathbf{v}_{\text{rom}}$, are displayed on the upper and the lower level of Fig. 30, respectively. The velocity estimation of the ROM adequately approaches the accurate CFD solution, achieving an average error of 0.03 m/s on the validation dataset. The highest discrepancies are marked locally on the segment of the pulmonary artery (Fig. 30 (c–g),(d–h)). In high shunt curvatures, e.g. Fig. 30 (a–e),(b–hf), an area of low velocities appears on the inner upper part of the shunt.

In Fig. 31, the surface pressure ROM prediction, $\mathbf{v}_{\text{rom}}$, is compared with the CFD model, $\mathbf{v}_{\text{ref}}$, for four different shunt morphologies. The local maps for scenarios No. 76 (a–e), No. 87 (b–f), No. 99 (c–g), and No. 101 (d–h) are represented at the MBTS level. As visually witnessed, the ROM approach captures the pressure distribution along the shunt's geometry. The ROM's average pressure error is calculated equal to 1.92 mmHg. The maximum pressure occurs mainly in the middle of the shunt for all the considered scenarios.

Similarly, in Fig. 32, the WSS distribution between the CFD, $\mathbf{v}_{\mathrm{ref}}$, and the ROM model, $\mathbf{v}_{\mathrm{rom}}$, is displayed for four different investigated scenarios: No. 65 (a–e), No. 52 (b–f), No. 63 (c–g), and No. 87 (d–h), proving that the latter achieves precise predictions. The average deviation between the WSS ROM estimation and the corresponding CFD solution is 3.83 Pa.

In order to quantify the accuracy of the developed ROM models, the maximum detected absolute errors over all the investigated scenarios in terms of velocity, pressure, and WSS are depicted in Fig. 33. The greatest velocity error, $e^{\mathrm{abs}}_{\mathrm{ROM}}$, was found in scenario No. 34 and equated to 1 m/s. It was detected on a few cells of the root of the pulmonary artery and the middle portion of the shunt. The highest pressure error, $e^{\mathrm{abs}}_{\mathrm{ROM}}$, occurred in scenario No. 101 and its' magnitude was 1.38 mmHg. Finally, the largest discrepancy in the WSS ROM, $e^{\mathrm{abs}}_{\mathrm{ROM}}$, was identified in scenario No. 87, mainly on the upper part of the shunt, and was equal to 48 Pa.

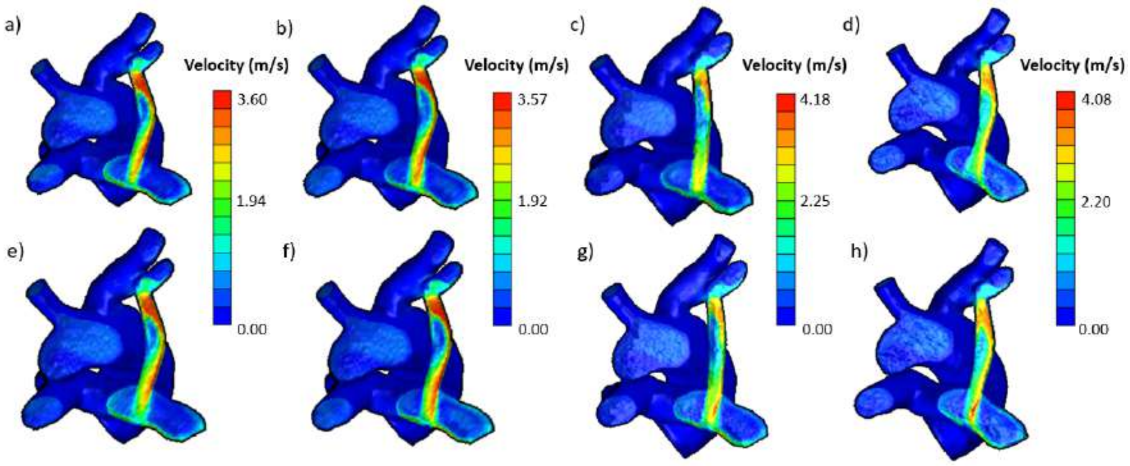

Figure 30: Velocity map comparison of the shunt's longitudinal cross-section between the CFD (**a**–**d**) and the ROM (**e**–**h**) flow field (**e**–**h**) for four different validation scenarios: No. 135 (**a**–**e**), No. 1 (**b**–**f**), No. 34 (**c**–**g**), No. 146 (**d**–**h**).

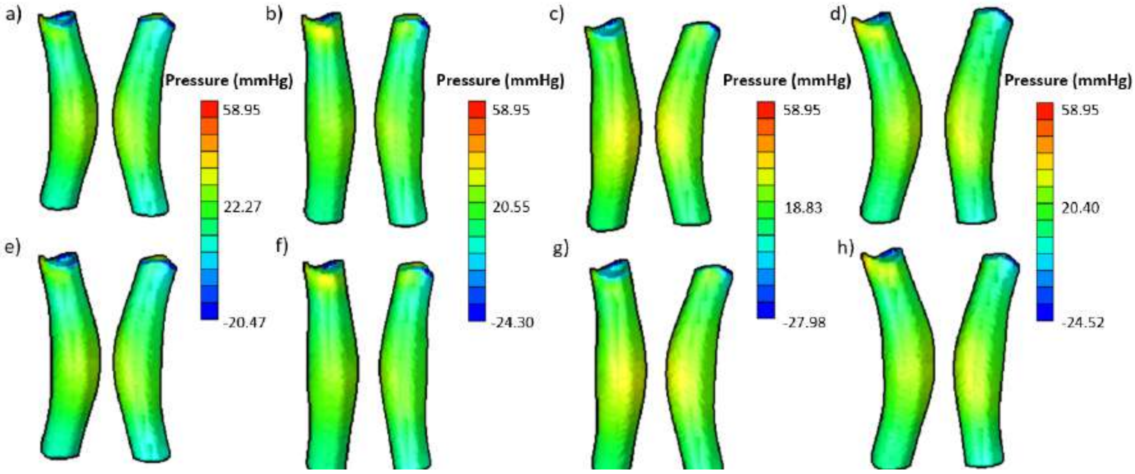

Figure 31: Pressure distribution comparison between the CFD (**a**–**d**) and the ROM (**e**–**h**) flow field (**e**–**h**) for four different validation scenarios using two perspectives: No. 76 (**a**–**e**), No. 87 (**b**–**f**), No. 99 (**c**–**g**) and No. 101 (**d**–**h**).

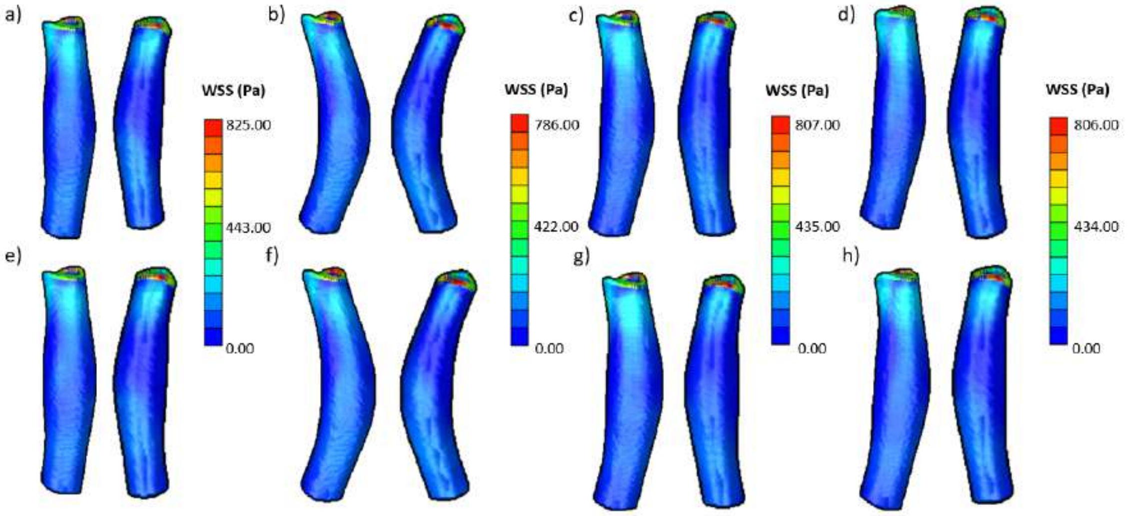

Figure 32: Wall Shear Stress distribution comparison between the CFD (**a**–**d**) and the ROM (**e**–**h**) flow field (**e**–**h**) for four different validation scenarios using two perspectives: No.65 (**a**–**e**), No. 52 (**b**–**f**), No. 63 (**c**–**g**), No. 87 (**d**–**h**).

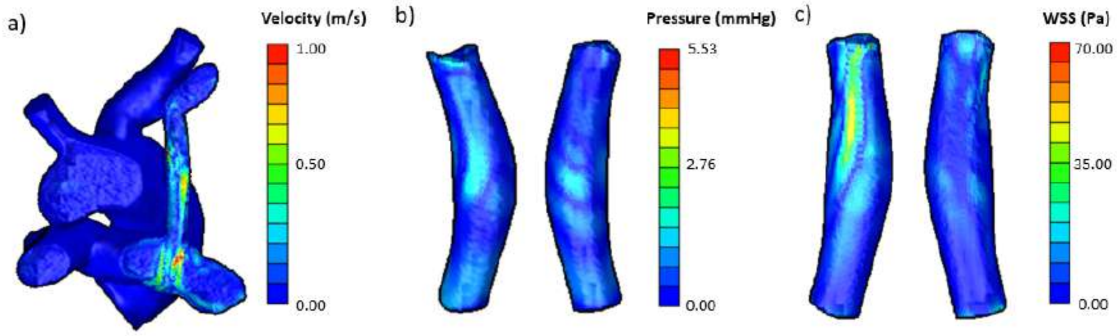

Figure 33: Maximum absolute error of the velocity in scenario No. 34 (**a**), pressure in scenario No. 101 (**b**), and wall-shear stress in scenario No. 87 (**c**) ROM.

3.1.3 ROM Exploitation

Having successfully generated the ROM model, the ROM exploitation is presented in this subsection. The built velocity field ROM file occupies a memory storage of 3 GB, considering its volumetric distribution, while those relative to pressure and WSS fields require 31.2 MB and 35.6 MB, respectively. Concerning the computational requirements, the ROM loading requires 2–3 min. Once their mounting is completed, the user is allowed to interactively set up the MBTS geometry of interest by tuning the available sliders which correspond to the amplification factor of the twelve RBF shape modifiers. A demonstration of the resulting Digital Twin with its interactive environment for the estimation of the velocity field is depicted in Fig. 34.

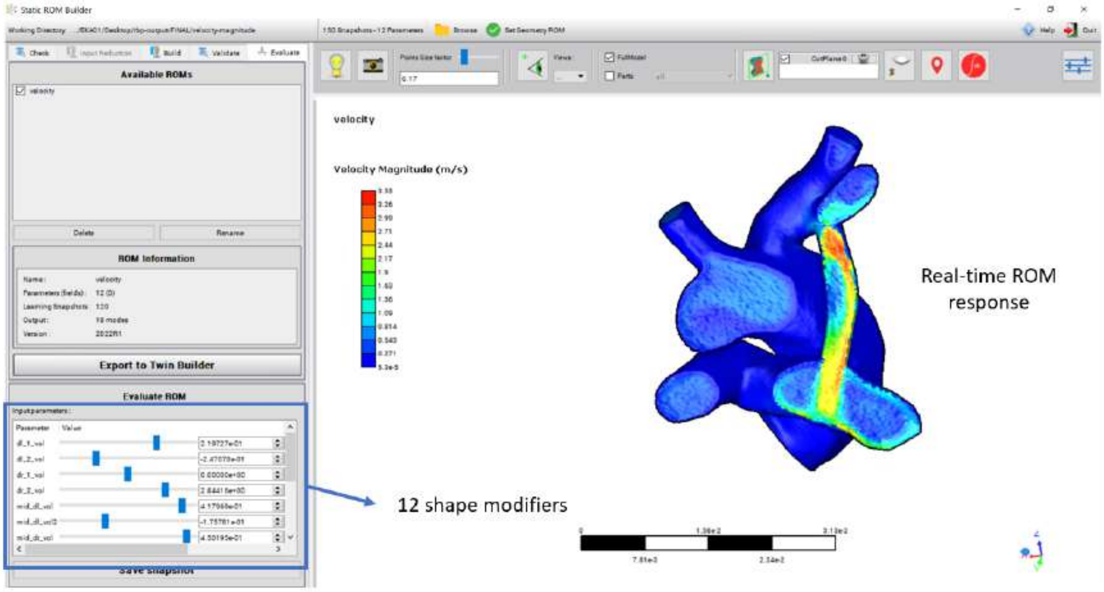

Name: velocity
Parameters (fields): 12 (0)
Learning Snapshots: 120
Output: 18 modes
Version: 2022R1

Figure 34: Visualization of the Digital Twin GUI with the interactive environment of the ROM exploitation. Inside the blue colored box (on the left side), there are twelve sliders with which the user can tune the amplification factor of the shape modifiers. The velocity field view, in a cross-sectional plane of the shunt, is provided in real time.

Based on our preliminary experience with ROM exploitation, we found out that mid-dr-vol and mid-dl-vol were the most impactful parameters on the distribution of WSS. For assessing the influence of the parameters, we opted for the WSS ROM since wall shear stresses are associated with various cardiovascular implications[158,159]. In Fig. 35, the WSS ROM predictions are displayed for various amplification factors of mid-dr-vol ranging from -0.5 to 0.5. We can see that the upper extreme of the shunt experiences high WSS, reaching up to 200 Pa, when the amplification factor goes below zero. On the contrary, when the amplification factor increases (>0), then there is a rise in the WSS on the pulmonary branch.

In Fig. 36, the effect of the mid-dl-vol parameter is presented. As demonstrated, increased values of the mid-dl-vol amplification factor correspond to decreased WSS on the upper section of the shunt.

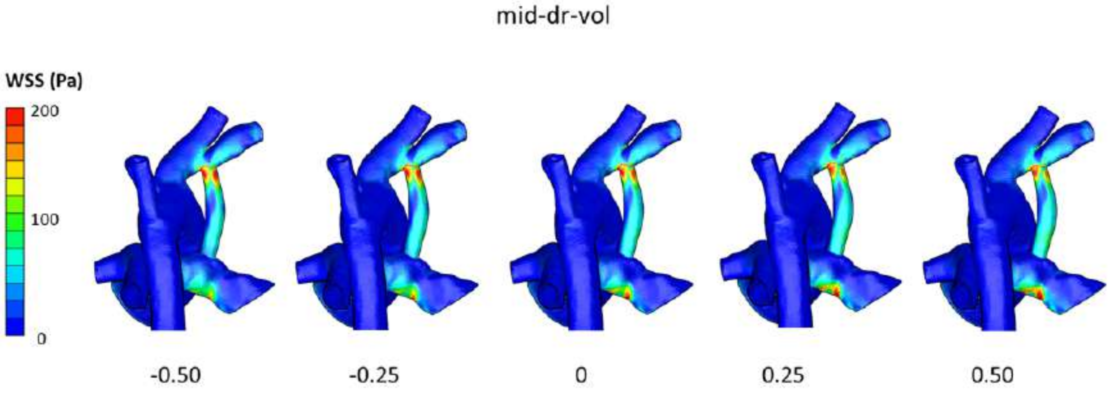

Figure 35: WSS ROM prediction as a function of the amplification factor of mid-dr-vol (defined in section 2.5.2): high WSSs appear in the upper extreme of the shunt for amplification factors lower than zero.

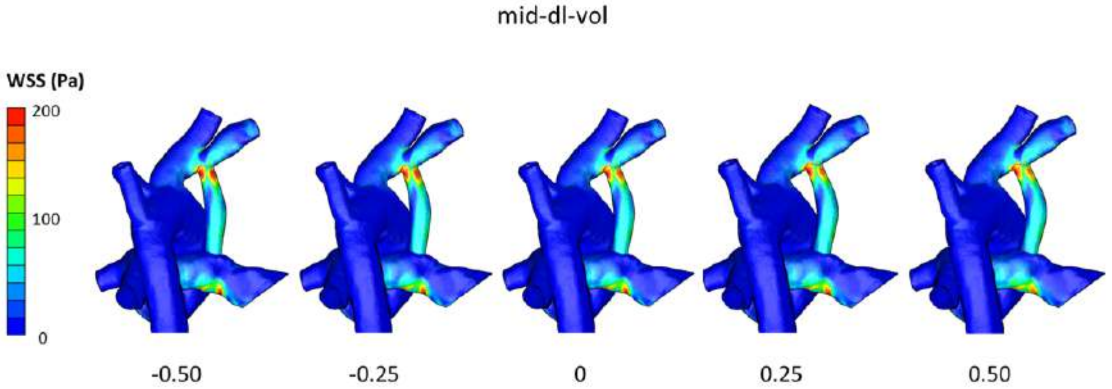

Figure 36: WSS ROM prediction as a function of the amplification factor of mid-dl-vol (defined in section 2.5.2): decreased WSSs occur in the upper shunt section for elevated amplification factors of mid-dl-vol.

Finally, a timeframe comparison for the assessment of the ROM performance against the full CFD analysis is reported in Fig. 37. A complete CFD simulation takes 45 minutes on an 8-core laptop, including the re-meshing process through Ansys® Fluent. Conversely, the computational investment for building up a ROM amounts to approximately 20 hours. Then, the produced ROM can be exploited in almost real-time, offering precise predictions in function of the twelve shape parameters, via an 8-core laptop.

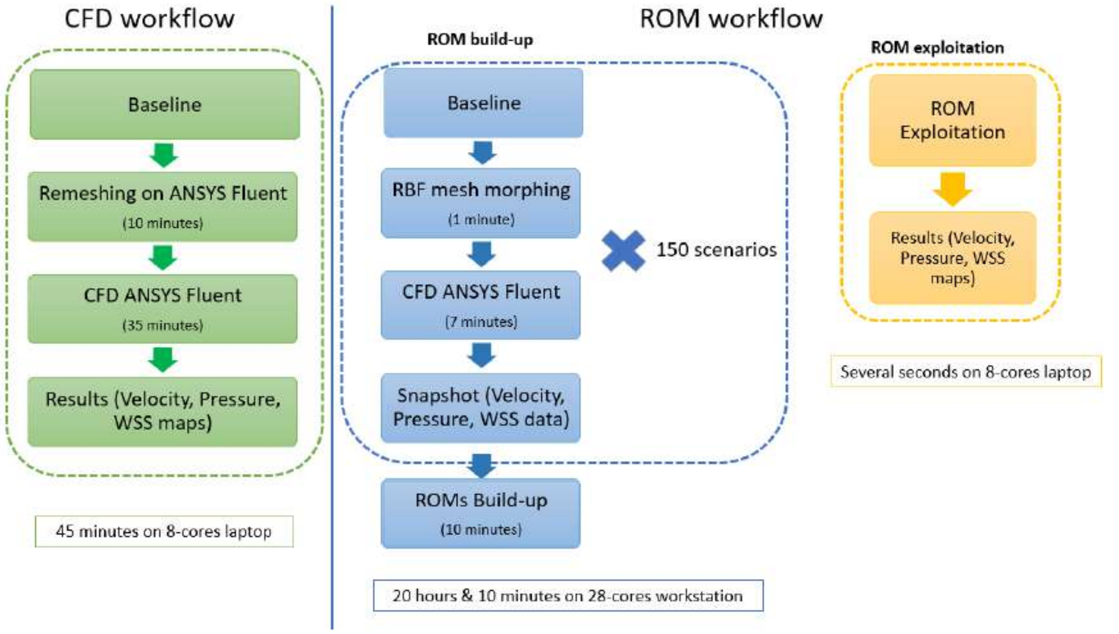

Figure 37: Timeframe comparison between the CFD and the ROM for the exploration of possible MBTS configurations.

3.2 Study II

In this section, the results of the developed physical ROM, i.e. displacement field, for EVAR navigation are reported. Initially, the accuracy of the built ROM is evaluated and then a practical ROM application is demonstrated. Finally, a qualitative sensitivity analysis of the studied parameters is presented.

3.2.1 ROM Validation

A statistical analysis of the relative reduction and ROM error was performed for the assessment of the model's trustworthiness. The distribution of the relative reduction error, $e^{\text{rel}}_{\text{red}}(\%)$, i.e., the error deriving from the approximation of the displacement field using only the first 38, r, modes, is presented in Fig. 38a for all the validation scenarios. In Fig. 38b the relative ROM error, $e^{\text{rel}}_{\text{ROM}}(\%)$ is displayed and it represents the sum of the relative reduction error and the GARS interpolation error.

The average relative reduction error, $e_{\text{red}}^{\text{rel}}(\%)$, is equal to 0.26 ± 0.06%. In 74% of the validation scenarios $e_{\text{red}}^{\text{rel}}(\%)$ varies between 0.20% and 0.30%. An $e_{\text{red}}^{\text{rel}}(\%)$ of more than 0.4% occurs for only three scenarios (Fig. 38 a)).

With regards to the relative ROM error, more than 75% of the validation scenarios have a $e_{\text{ROM}}^{\text{rel}}$ below 4.0% (Fig. 38(b)). The average $e_{\text{ROM}}^{\text{rel}}$ is estimated equal to 3.28 ± 1.00%.

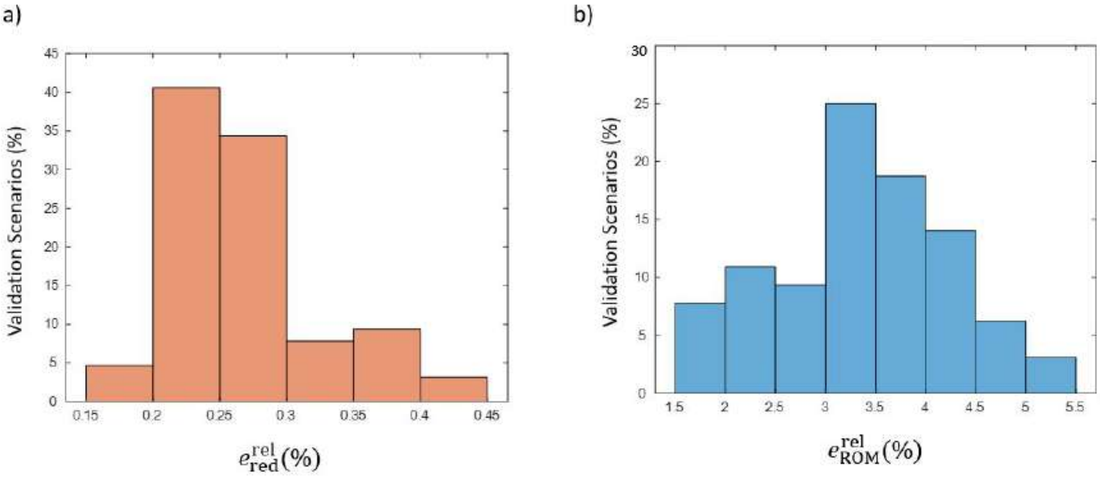

Figure 38: Distribution of the relative reduction error $e_{\text{red}}^{\text{rel}}(\%)$, a) and the relative ROM error $e_{\text{ROM}}^{\text{rel}}(\%)$, b) on the validation scenarios.

In Fig. 39, the absolute deformation error, $e_{\text{ROM}}^{\text{abs}}$, of five chosen validation scenarios, among the least accurate ones, is presented. The maximum $e_{\text{ROM}}^{\text{abs}}$ is 0.32 mm and is observed in validation scenario (d) close to the origin of the left iliac artery. The largest discrepancy between the ROM prediction and the high-fidelity solution is detected in the same region, i.e. left iliac artery, for all scenarios. The aneurysmatic bulge deformation is predicted with an average error of 0.17 mm on validation scenarios (b), (c), and (e). The prediction error, $e_{\text{ROM}}^{\text{abs}}$, of the aortic neck region is below 0.1 mm for scenarios (c), (d), (e), and ≈ 0.20 mm for scenarios (a) and (b).

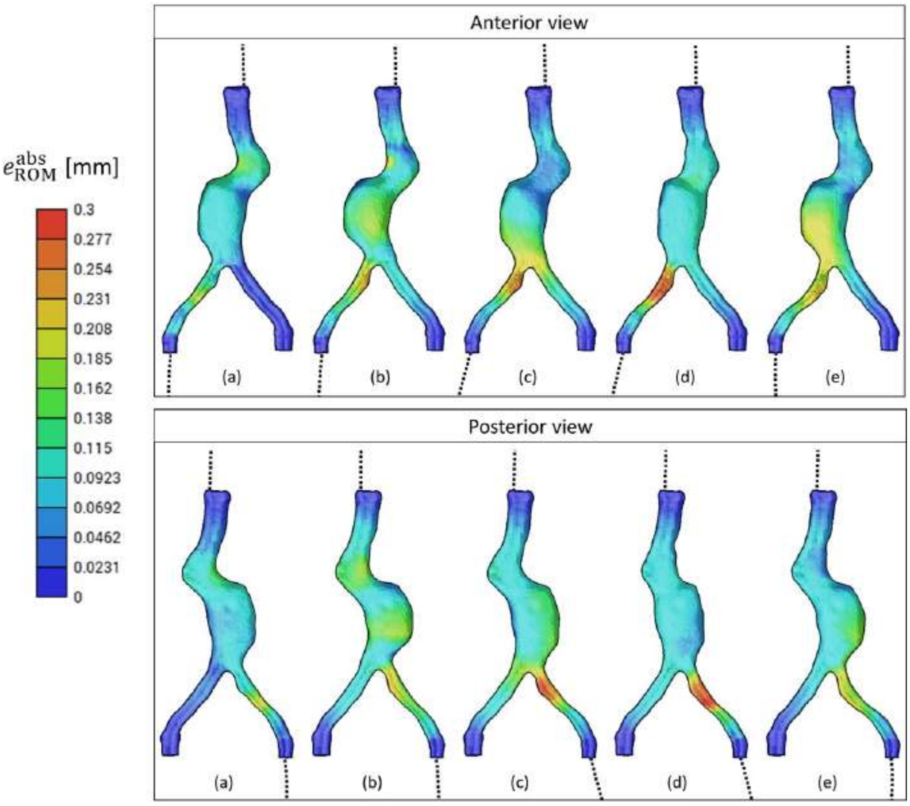

Figure 39: Colour map of the ROM absolute error, $e_{\mathrm{ROM}}^{\mathrm{abs}}$ for five validation scenarios (a), (b), (c), (d) and (e), anterior and posterior views. The values are displayed on the final deformed geometries (i.e. geometrical ROM) resulting from the guidewire interaction with the aorta.

3.2.2 ROM Exploitation

After the successful ROM training and validation, hands-on deployment of the pipeline was carried out. As exhibited in Fig. 40, we selected a trial parametric set-up (E_{aorta}=1.5 MPa, E_{wire}=180 GPa, ϕ=-5°, θ=7°, α=48°, β=52°, τ=0.15) and we were provided with the depicted aortic displacement, i.e. $\mathbf{u}_{\mathrm{ROM}}$, within few seconds.

The left iliac artery experienced the greatest deformations, reaching up to 13 mm, straightening towards the posterior and left patient-oriented direction. The aneurysmatic bulge, the aortic neck, and the right iliac artery were displaced towards the right superior direction. The magnitude of this displacement was 6.5 mm on average. The neck region moved anteriorly in contrast with the aneurysm and the iliac arteries. The sagittal side of the aneurysmatic sac underwent high displacements, almost 9.5 mm, to the superior and right direction.

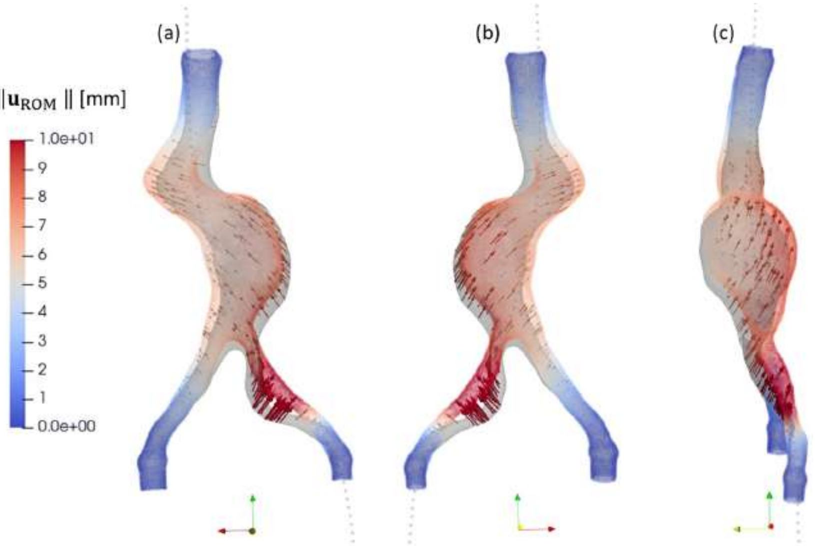

Figure 40: Example of ROM output for the following chosen parameters: E_{aorta}=1.5 MPa, E_{wire}=180 GPa, ϕ=-5°, θ=7°, α=48°, β=52°, τ=0.15. The nodal displacement vectors, $\mathbf{u}_{\text{ROM}}$, defined from the initial (light grey) to the final (color-mapped by displacement magnitude) aortic configuration, are presented. (a) Anterior view, (b) Posterior view, (c) Sagittal view.

3.2.3 Qualitative analysis of the influence of the investigated parameters

The following remarks resulted from the examination of the individual impact of each parameter on the 3D aortic displacement. The findings presented in this section stem from our observations as ROM users and should not be regarded as an extensive study, such as principal component analysis.

In Fig. 41, eight example cases, investigating the impact of aortic elasticity and guidewire's stiffness on the aortic deformation field, are shown. For descending values of E_{aorta}, the left iliac artery and the left side of the aneurysm are encountering increasing displacements, with a maximum value of 12 mm in the case of E_{aorta}=0.9 MPa. The aortic neck region is almost unaffected by the explored values of aortic elasticity. Adopting $E_{\text{aorta}} = 2.9$ MPa, instead of 0.9 MPa, leads to a more uniform deformation map with maximum displacements reduced by 60%. A similar displacement field, i.e., almost equal deformation vectors throughout the whole aorta, is obtained for increasing E_{aorta} and decreasing E_{wire}.

The effect of choosing different insertion angles, ϕ and θ, is presented in Fig. 42. When ϕ is close to zero, the displacement of the left iliac artery and part of the left side of the aneurysm increases. The remaining geometry stays almost unaltered.

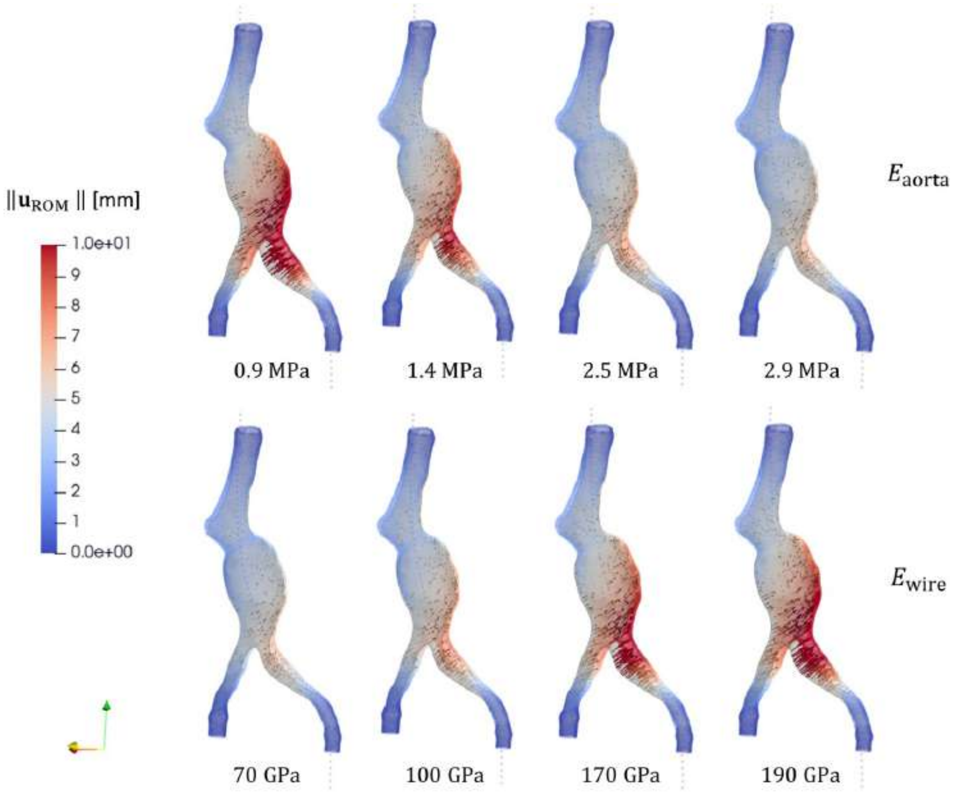

Figure 41: Aortic displacement, $\mathbf{u}_{\mathrm{ROM}}$, as a function of E_{aorta} and E_{wire} parameters. The initial aortic configuration is shown in light grey. The arrows indicate the guidewire-induced displacement vectors, $\mathbf{u}_{\mathrm{ROM}}$. The deformed aortic configuration is colored by the displacement vector magnitude, $\|\mathbf{u}_{\mathrm{ROM}}\|$. The remaining parameters were fixed as follows: $\phi = 0°$, $\theta = 0°$, $\alpha = 44.2°$, $\beta = 32.8°$, $\tau = 0.12$.

For the investigated scenarios, the peak deformations take place for ϕ equal to -5° and extend up to 8.5 mm. The magnitude of θ has negligible effect on the aortic displacement field. For the investigated angles, the most deformed nodes are concentrated on the left iliac artery and the left side of the aneurysmatic sac.

The effect of the left iliac tortuosity is illustrated in Fig. 43. Low tortuosity values result mainly in the displacement of the left iliac artery's origin and left aneurysmatic side in the postero-superior leftward direction. Moving to higher tortuosity values, above 0.12, complex aortic motions take place: the effect of the straightening on the left iliac artery increases, with higher displacement vectors and greater displacement components in the superior direction. The neck region and the aneurysm are displaced towards the right superior direction.

Finally, in Fig. 44, the time comparison between the FE and the ROM trained on FE simulations is presented. As illustrated, every high-fidelity FE simulation costs

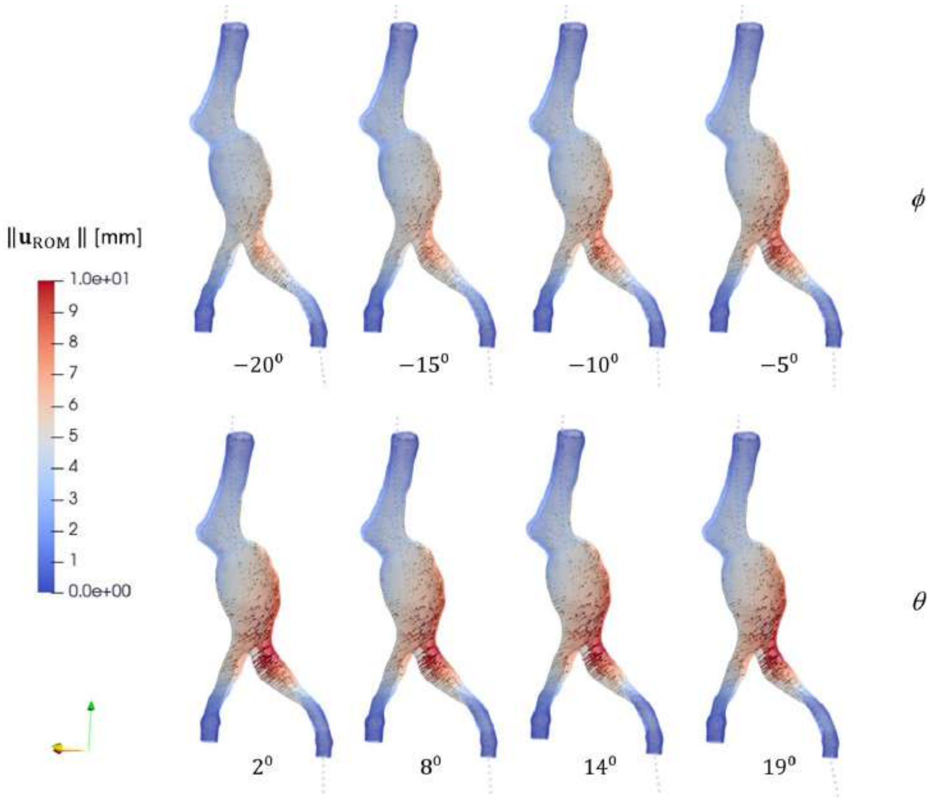

Figure 42: Aortic displacement, $\mathbf{u}_{\mathrm{ROM}}$, obtained from ROM as a function of insertion angles, ϕ and θ. The initial aortic configuration is shown in light grey. The arrows indicate the guidewire-induced displacement vectors. The deformed aortic configuration is colored by the displacement vector magnitude, $\|\mathbf{u}_{\mathrm{ROM}}\|$. The remaining parameters were set as follows: E_{aorta}=1.4 MPa, E_{wire}=150 GPa, $\alpha = 44.2°$, $\beta = 32.8°$, $\tau = 0.12$.

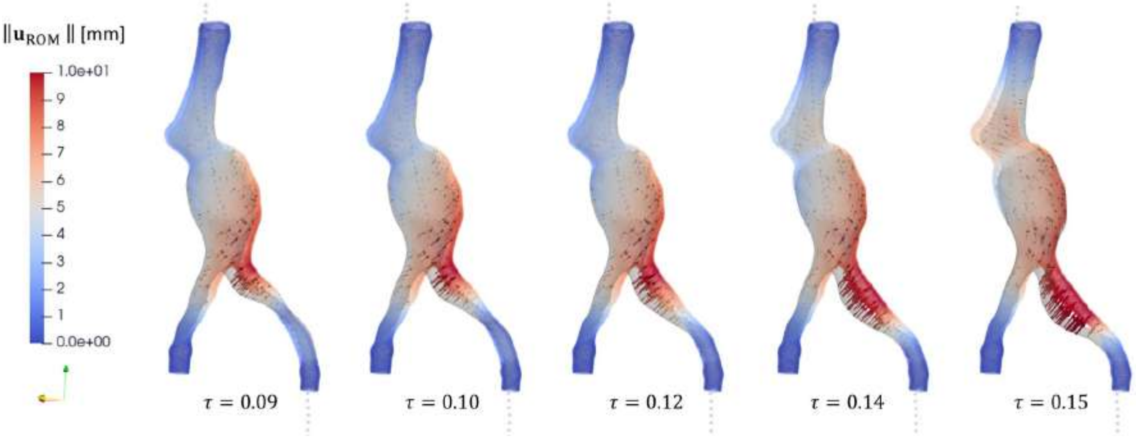

Figure 43: Aortic displacement, $\mathbf{u}_{\mathrm{ROM}}$, obtained from ROM as a function of left iliac tortuosity, τ. The initial aortic configuration is shown in light grey. The arrows indicate the guidewire-induced displacement vectors. The deformed aortic configuration is colored by the displacement vector magnitude, $\|\mathbf{u}_{\mathrm{ROM}}\|$. The remaining parameters were fixed as follows: E_{aorta}=1.4 MPa, E_{wire}=150 GPa, $\phi = 0°$, $\theta = 0°$, $\alpha = 44.2°$, $\beta = 32.8°$.

70 min, including CT segmentation, postprocessing, and the computational part. Conversely, the ROM build-up involves a computational investment of 165 minutes, with the adopted set-up as presented in section 2.6.3, and then the ROM exploitation provides deformation predictions for all the aortic nodes in almost real-time.

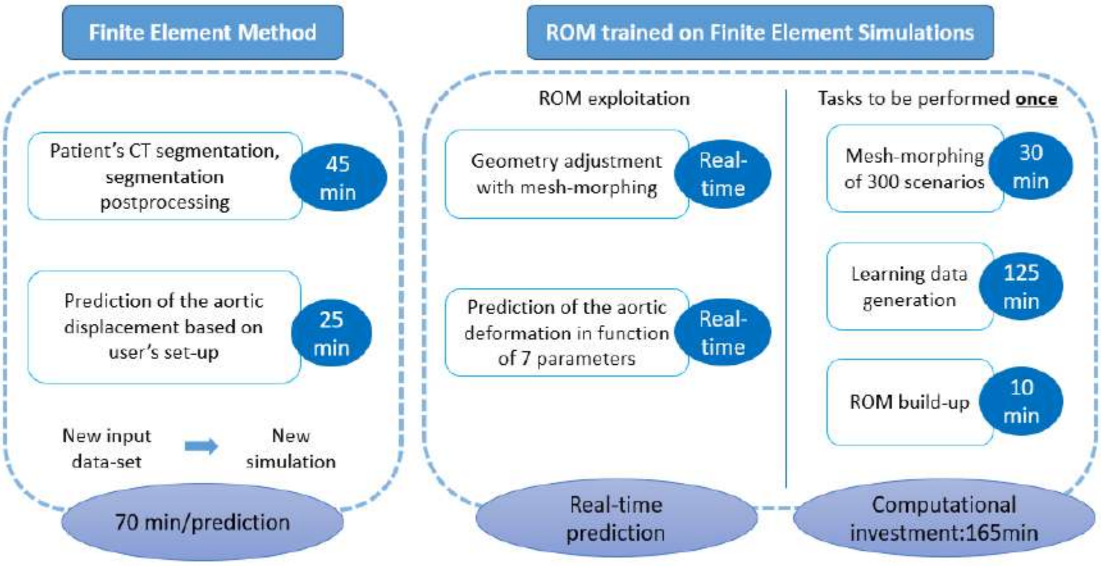

Figure 44: Timeframe comparison between the high fidelity finite element (FE) simulation and the reduced order model (ROM) trained on FE data.

3.3 Study III

In this section, the results of the third study on stent grafts' performance are presented. The results are divided into the following sections: shear strain rate examination, analysis of wall shear stress related indices, backflow, and velocity vectors analysis.

3.3.1 Shear strain rate examination

In Fig 45a, the total volume of each zone's cells characterized by shear strain rates higher than 3000 s^{-}1, i.e. V_{SSR}, is illustrated over the course of a heart cycle. The main body of all the stents experienced elevated SSR between 0.1 and 0.3 s. In the systolic peak, V_{SSR} of model 1, 2, and 3 was 0.0029 ml, 0.0048 ml and 0.0032 ml accordingly. With regards to the flared extension, zones 1 to 5 of model 1 were detected with a high strain rate between 0.1 and 0.4 s. Among them, the most affected zones were 1 and 2 on the systolic peak, as well as zone 5 after the systolic peak. As for the zones of the straight stent extension, they are omitted since they were not exposed to significant SSR in any of the considered grafts. Finally, the flared graft extension of model 2 and 3 was free from high SSR.

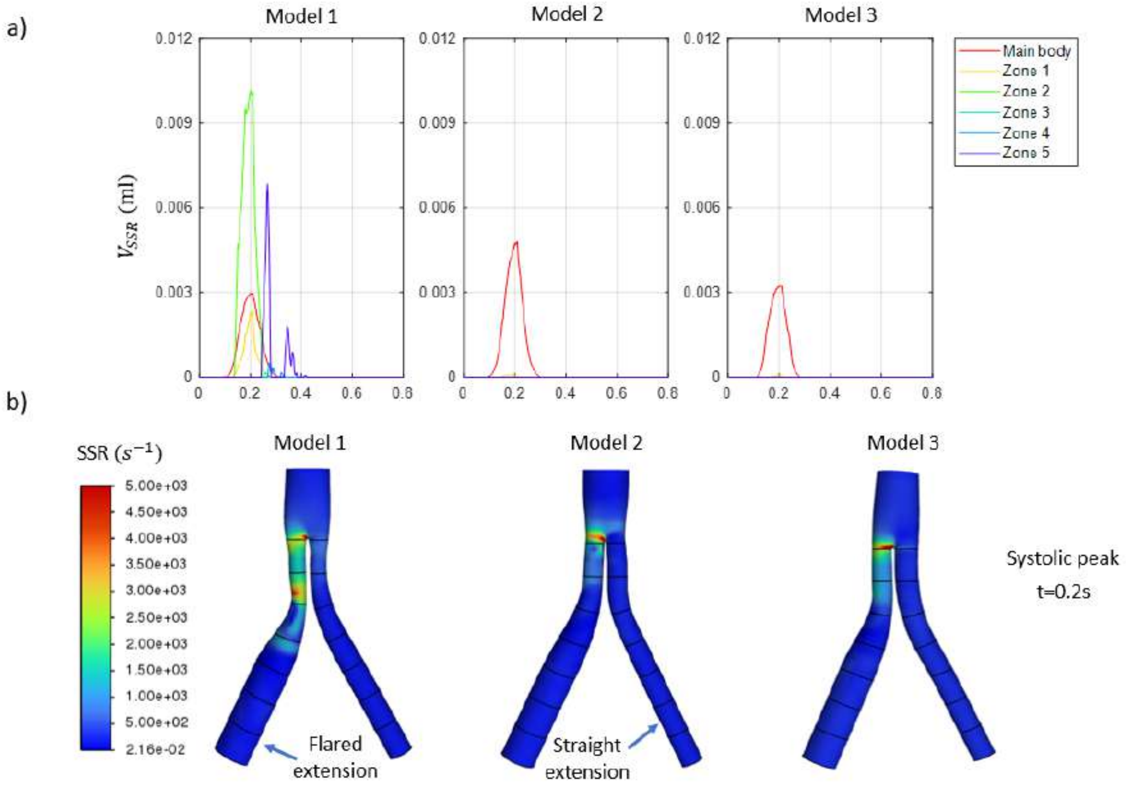

Figure 45: Blood volume with strain rate higher than 3000 s^{-}1: a) diagram of highly stressed volume (ml) per zone per stent graft b) visual representation of the zones' strain rate at the systolic peak.

To enhance the clarity of the findings, we present the shear strain rate map on the surface of models 1, 2, and 3 at systolic peak (t=0.2 s). As witnessed, the bifurcating area was marked with high strain rates up to 5000 s^{-}1 for all the stents. The highly loaded areas were located towards the flared side in all grafts. Additionally, zones 1 and 2 of model 1 were exposed to an area-averaged SSR equal to 1800 s^{-}1 and 2400 s^{-}1 respectively. The corresponding zones of models 2 and 3 were characterized by significantly lower SSR values.

3.3.2 Analysis of Wall-Shear-Stresses related indices

In Fig. 46, 47, and 48, the distribution of the time averaged wall shear stresses ($TAWSS$), oscillatory shear index (OSI), and the endothelial cell activation potential ($ECAP$) are presented on the grafts' wall respectively. According to the literature, $TAWSS$ values lower than 0.3 Pa are linked with stagnant flows, which can trigger thrombus formation. Following this indication, we make the following observations with regard to Fig. 46. The main body of model 3 was characterized by $TAWSS$ less than 0.3 Pa. The same happened to model 1 and 2 but in a smaller range. Zones 4 to 8 of model 2 and 3 were affected by low $TAWSS$. On the contrary, this occurred only in zones 6, 7, and 8 of model 1. As for the straight graft extension, all the zones of model 2, 3 and zones 12 till 15 of model 1 were affected by $TAWSS$ values below 0.3 Pa.

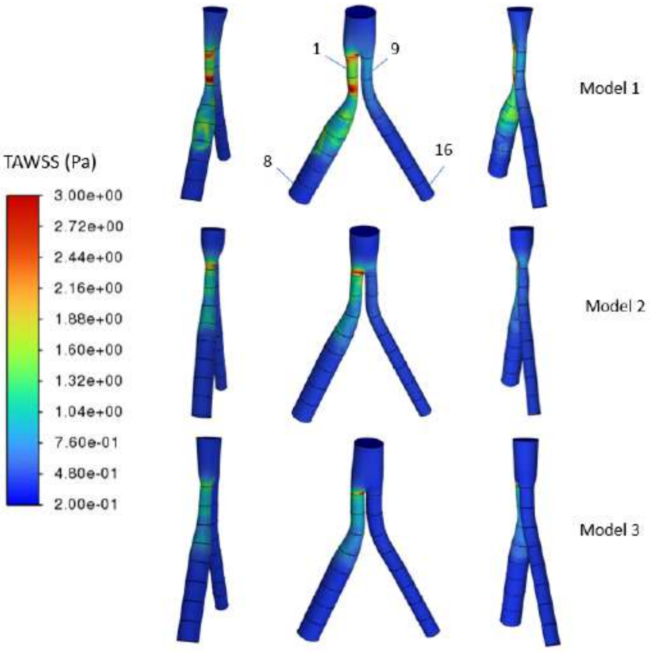

Figure 46: Distribution of time averaged wall shear-stresses ($TAWSS$) on the 17 zones of models 1, 2, and 3, which correspond to the simplified models of Zenith Alpha, Excluder and Endurant II. $TAWSS$ are presented in one frontal and two side views. The zones' numbering is reminded in the frontal view of model 1 (Fig. 7).

As already highlighted in section 2.3.3, OSI values exceeding 0.3 are associated with thrombotic events. Bearing this in mind, we pinpoint the corresponding areas in Fig. 47. OSI values reached up to 0.45 in the main body of model 2 and 3, while they remained in lower levels in the same area of model 1. More precisely, the area-averaged OSI value on the main body of model 1, 2, and 3 was calculated equal to 0.23, 0.27, and 0.34, accordingly. As for the flared graft extension, complex high OSI patterns took place. More precisely, OSI values higher than 0.3 were locally detected on zones 3 to 8 of model 1 and on all zones, i.e., 1 to 8, of models 2 and 3. Regarding the straight extension, elevated OSI values, exceeding 0.3, were identified in all zones of all grafts except from zone 9 of model 1. Peak values, in the range of 0.4 and 0.5, were found mainly in zones 11 and 12 of all grafts.

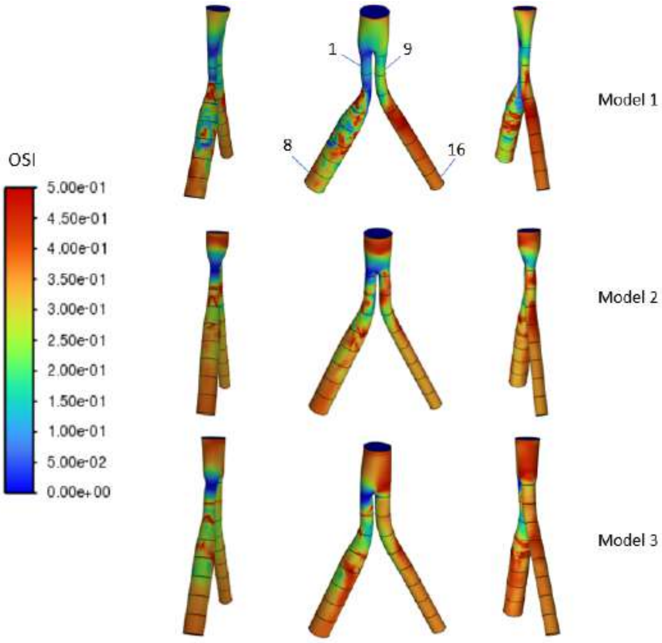

Figure 47: Distribution of Oscillatory Shear Index (OSI) on the 17 zones of models 1, 2, and 3, which correspond to the simplified models of Zenith Alpha, Excluder and Endurant II. OSI are presented in one frontal and two side views. The zones' numbering is reminded in the frontal view of model 1 (Fig. 7).

Finally, in Fig. 48, the endothelial cell activation potential ($ECAP$) of the examined grafts is showcased. As already explained in section 2.3.3, areas with $ECAP$ higher than 1.4 Pa^{-1} are considered thrombogenic. Upon initial inspection, we observe that model 3 was characterized by high $ECAP$ values, in the range of 1.4 – 1.7 Pa^{-1} in the main body, zones 6 till 8 of the flared extension and on the whole straight graft extension. Model 2 had elevated $ECAP$ values, solely on the main body and zones 11 and 12 of the straight extension. Finally, in the case of model 1, primarily zones 12 to 16 of the straight extension and secondarily zones 7 and 8 of the flared extension were affected by increased $ECAP$ values.

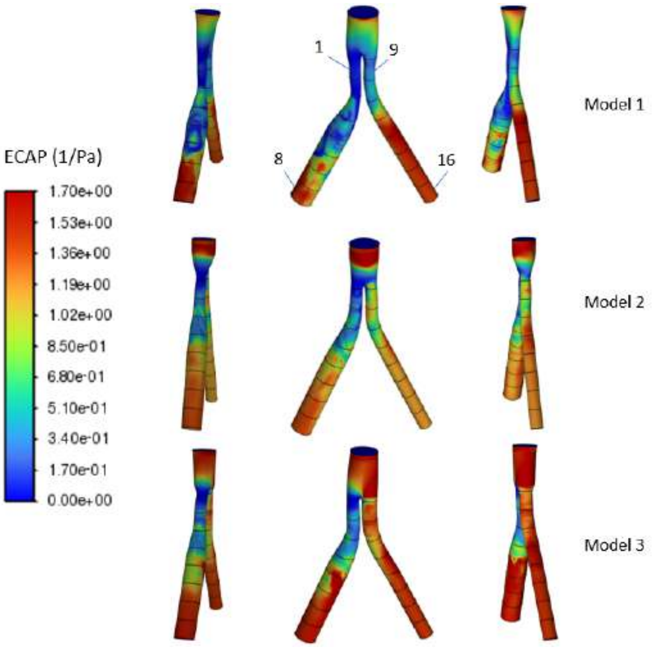

Figure 48: Distribution of Endothelial Cell Activation Potential ($ECAP$) on the 17 zones of models 1, 2, and 3, which correspond to the simplified models of Zenith Alpha, Excluder and Endurant II. $ECAP$ are presented in one frontal and two side views.The zones' numbering is reminded in the frontal view of model 1 (Fig. 7).

3.3.3 Backflow analysis

As already mentioned in section 2.3.3, the recirculation was calculated through the measurement of the blood backflow and the visual analysis of the flow vortices. Regarding the first approach, in Fig. 49, we present the percentage of backflow volume, V_{back} (%), inside each fluid zone for the ipsilateral a) and the contralateral b) graft extension over one heart cycle. The percentage of backflow volume was computed according to equation 6: 100% signifies complete reverse flow, and 0% denotes pure downstream flow.

Examining the curves of Fig. 49 on the ipsilateral and contralateral side, we note that significant backflow was developed in all the zones between 0.35 and 0.45 s due to the imposed flow reverse. Since the scope of this study is the detection of recirculation phenomena, we emphasize the results' analysis in the period before and after the negative flux, i.e., 0 – 0.35 s and 0.45 – 0.8 s.

At the start of the cardiac cycle, all the zones on the flared part of the grafts experienced backflow smaller than 50%. This backflow was terminated for all stents

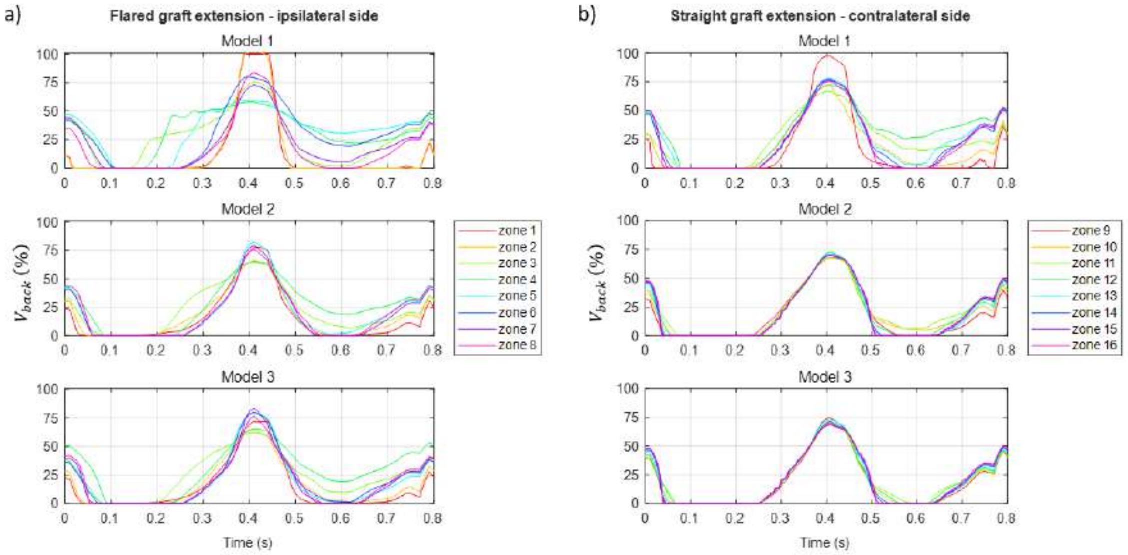

Figure 49: Percentage of backflow volume, V_{back} (%), of the different fluid zones of the examined stent grafts in the duration of a heart cycle: a) zones of the flared extension on the ipsilateral side, b) zones of the straight extension on the contralateral side.

at 0.1 s on average. After that time, zones 3 and 4 of model 1 presented backflow from 0.14 s and 0.17 s, respectively, until the end of the heart cycle. On the contrary, no backflow was detected in any zone of models 2 and 3 before the systolic peak, i.e., 0.2 s. After peak systole, zones 1, 2, 3 of models 2 and 3 experienced reverse flow with the corresponding backflow percentages reaching up to 15%, 20%, and 40% at 0.3 s for both stents. At that moment, backflow percentages of zones 3, 4, and 5 of model 1 were found equal to 36%, 50%, and 50%, accordingly. As for the timeframe between 0.5 s and 0.8 s, we detect that zones 3, 4, and 5 of model 1 retained considerable backflow percentages. At the same time, zones 1 and 2 of models 2, and 3 presented backflow from 0.65 s till the end of the cardiac cycle. The backflow percentages of zones 1, 2 of model 2 and 3 were significantly lower than the ones of zone 3, 4, and 5 of model 1 in the post diastolic peak period.

Focusing on the contralateral side, we observe that between 0.1 and 0.2 s, no backflow was detected in any of the grafts. After the systolic peak, backflow appeared in zone 11 of model 1 at 0.22 s, zone 9 of model 2 at 0.23 s, and in all zones of model 3 simultaneously at 0.25 s. At 0.3 s, backflow had spread in all zones of the grafts with zone 11 of model 1 having the highest backflow percentage equal to 35%. After the diastolic peak, zones 10, 11, 12, and 13 of model 1 had a persistent percentage of backflow until the end of the heart cycle. Model 2 displayed the same behavior solely in zones 10 and 11. On the opposite side, model 3 had small backflow percentages, which were zeroed out in all zones at 0.6 s. At that time instance, zones 10, 11, 12, and 13 of model 1 had backflow percentages equal to 3%, 16%, 26%, and 4%, respectively, whereas zones 10 and 11 of model 2 both had 6%. Finally, the backflow curves of zones 14, 15, and 16 experienced oscillations for all the considered grafts throughout the heart cycle.

In summary, during a cardiac cycle, the flared extension of model 1 exhibits more backflow for longer periods, particularly in zones 3 and 4, compared to the other models. On the straight extension, the backflow is generally lower than the flared one for all the examined grafts, but still, model 1 experiences more reverse flow.

3.3.4 Velocity vectors analysis

For correlating the backflow with the recirculation, we present the velocity vectors analysis for each stent graft extension separately. In Fig. 50, the velocity vectors coloured by their magnitude are showcased on the main cross-section of the flared extension of the considered grafts for eight different time instances. Upon primary examination, we observe that the vectors' distribution in models 2 and 3 resemble each other but they are substantially different from model 1. At the beginning of the heart cycle, low velocity magnitude vectors with non-uniform orientation were found in all zones of the grafts, however, zones 1 and 2 of models 2 and 3 as well as zone 3 of model 1 had discernible swirls. At 0.1 s, no eddy vectors were formed on the grafts, but some velocity vectors were diverging from the main flow stream in zone 4 of the considered stents. At systolic peak, recirculation appeared on a large area of zones 3 and 4 of model 1 and on a small region of zone 1 of models 2 and 3. At 0.3 s, the swirling wave had spread from zone 3 to 5 of model 1 and, zone 1 to 3 of model 2 and 3. The flow experienced severe obstructions at 0.4 s, where negative flow prevailed. Recirculating vectors were formed on the root of zone 1 of models 2 and 3. This did not happen in model 1. At 0.5 s, zone 1 of models 2 and 3 retained significant backflow vectors whereas model 1 was backflow free. From 0.6 s and on, swirling vectors were detected in zones 3 to 6 of model 1 and zones 1 to 4 of models 2 and 3.

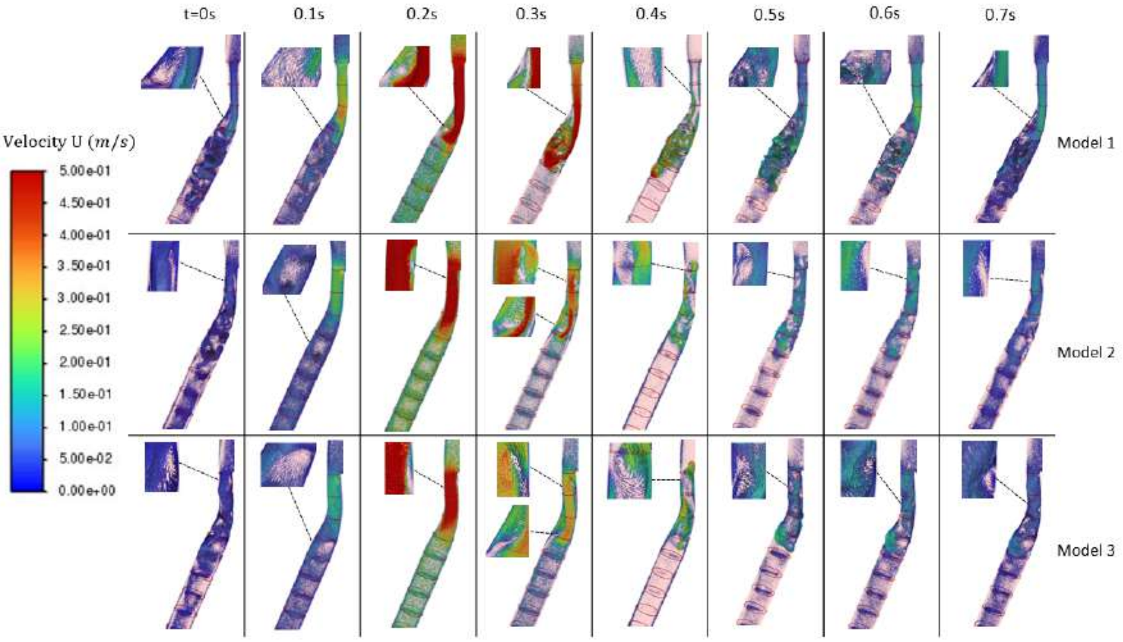

Figure 50: Illustration of the velocity vectors colored by their magnitude, on the main cross-section of the ipsilateral graft extension of models 1, 2, and 3 for 8 discrete time instances in the heart cycle. For enhancing comprehension, the areas of interest are shown with zoom, and the surfaces separating the fluid zones, described in Fig. 7, are included. Before the systolic peak (t=0.2 s), a distinct swirl is formed in zones 3 and 4 of model 1. This vortex extends within zones 3 - 6 between 0.2 and 0.4 s. Smaller swirls are formed in the other grafts.

In Fig. 51, the velocity vectors on the main cross-section of the contralateral iliac graft extension are presented for the considered grafts. At the start of the heart cycle, there was a distinct area that separated the downstream vectors from the backflow ones in all grafts. Backflow was accumulated on the right side of the graft wall. We observe that the flow disturbance was more profound in models 1 and 2 compared to model 3. At 0.1 s, the velocity vectors globally faced the downstream direction. At the systolic peak, no recirculating areas were recorded. The velocity vectors of model 1 had a magnitude of 0.5 m/s in zones 9, 10 whereas model 2 and 3 had 0.3 and 0.2 m/s respectively. At 0.3 s, eddy vectors appeared in zones 10, 11 of models 1 and 2. At this instance, model 3 experienced low uniform flow separation on its walls. At diastolic peak, back moving vectors of 0.25 m/s and 0.15 m/s were found in zones 10, 11 of model 1 and 2 accordingly. Uniform vectors of 0.05 m/s were located along the length of model 3. Finally, between 0.5 and 0.7 s, model 1 and 2 were subjected to some flow obstructions mainly in zones 9 to 11, while model 3 kept its smooth laminar flow profile on all its zones. Zone 9 of model 1 was the sole zone that purely restored its flow to the downstream direction, at 0.7 s.

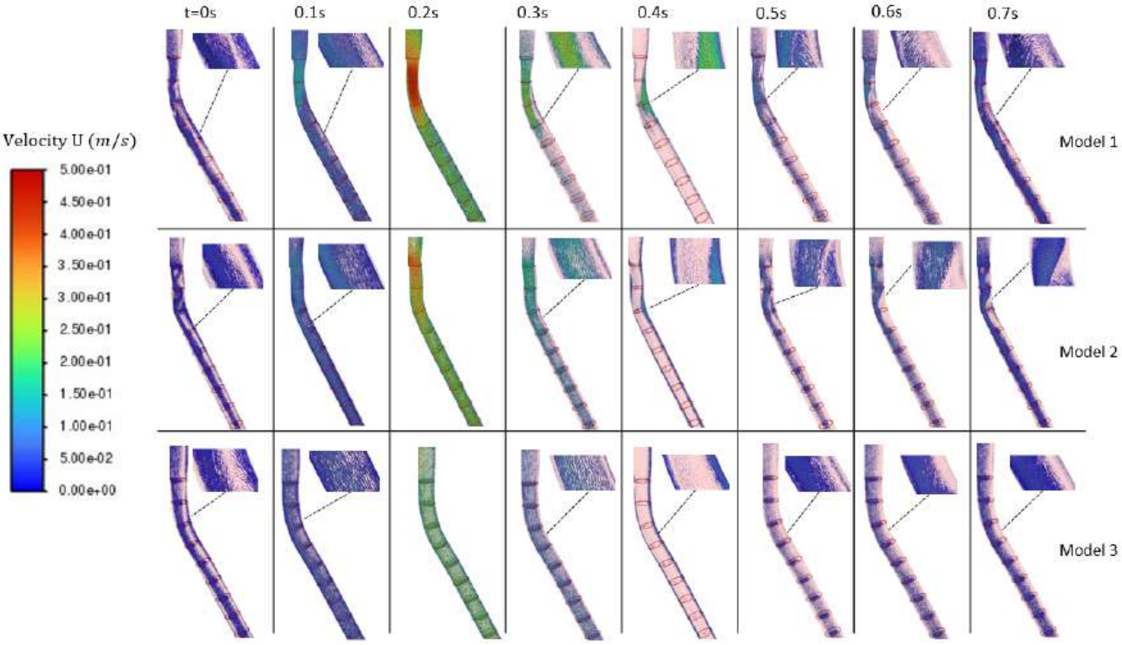

Figure 51: Illustration of the velocity vectors colored by their magnitude, on the main cross-section of the contralateral graft extension of models 1, 2, and 3 for 8 discrete time instances in the heart cycle. For enhancing comprehension, the areas of interest are shown with zoom, and the surfaces separating the fluid zones, described in Fig. 7, are included. Models 1 and 2 have a more disturbed flow in zones 1 - 3, compared to model 3.

4 Discussion

This thesis introduced a methodology for constructing reduced-order models for two distinct operations, i.e. MBTS and EVAR, enabling the patient specific pre operative planning and intra operative navigation. Furthermore, the computational fluid dynamic analysis provided some useful insight into the triggering mechanics of post-EVAR graft thrombus formation. This chapter delves into the significance of these findings, establishing connections with previous research works. The clinical relevance of the findings, with regard to pathophysiology, preoperative planning, and intraoperative procedure is reported. Eventually, the limitations of the presented works are discussed, outlining challenges for future research.

4.1 Study I

In the literature, several studies have been presented to investigate the effect of the MBTS geometry using hemodynamic fluid flow analysis[160,161,16]. Although most of these agree on the pivotal importance of the shunt's morphology for the success of an MBTS operation, no procedure has yet been established to perform preoperative patient-specific studies by exploring multiple implant configurations. Nowadays, the choice of the implant relies on clinicians' experience and is limited to assessing the implant's diameter. This study aimed to provide a tool for the fast and holistic morphological analysis of the MBTS taking into account the uniqueness of each patient's anatomy.

In order to meet this need, a comprehensive framework which fuses the ROM approach and the RBF mesh morphing technique was presented in this thesis, with the added value of providing fast and interactive prediction of the hemodynamic parameters. An infant case affected by complete pulmonary atresia was selected for demonstration of the pipeline's soundness. A baseline MBTS was placed between the pulmonary and the aortic artery (Fig.4). Mesh morphing enabled the modification of the position and shape of the implanted shunt by means of twelve RBF shape modifiers (Fig.22). These modifiers were used to generate possible shunt configurations, i.e., scenarios, for the building up of the ROM. Both morphing and ROM analysis were verified in terms of mesh degeneration and full CFD comparison, respectively. Finally, the ROM consumption allowed the definition of an effective Digital Twin for the evaluation of hemodynamic flow variables in real-time.

As mentioned in Section 2.5.2, it is crucial to inspect and control the mesh quality when employing a mesh morphing method. Adhering to this practice, we validated the adopted RBF mesh morphing technique, concluding that mesh quality degradation was acceptable for almost all of the explored scenarios. With the term acceptable, we state that the maximum cell squish of the mesh remains lower than the critical value of 0.99. As reported in Table 11, mesh quality was maintained for three out of the four meshes with the lowest quality. In the most degraded meshes, we note that the amplification factors of the rr-2-vol, rl-1-vol, dl-1-vol, dl-2-vol, and mid-dr-vo2l shape parameters lay close to the range extremes. This could suggest that these shape factors exerted the most significant influence on the meshing morphing performance of the MBTS structure. Although this constitutes the first work employing the mesh morphing technique for MBTS implants, this approach has been utilized successfully in several computational analyses on the cardiovascular context[108]. The calculated mesh degradation indexes are in accordance with the ones found in the literature[162,163].

Focusing on the building of the ROM, the high accuracy of the ROM predictions was verified with success. More precisely, validation was carried out with regard to the velocity (Fig. 30), pressure (Fig. 31), and WSS (Fig. 32) field. The scenarios reported in Fig. 30 show a velocity range and distribution in line with those reported in the previous literature[164,165]. It appears that higher velocity discrepancies occur at the MBTS junction with the pulmonary branch. This is particularly evident in scenarios with low-curvature MBTS implants (Fig. 30 c–g, d–h). This is further confirmed by the error map of Fig. 33a, where maximum absolute errors of 1 m/s (about 25% of the full velocity range) are reached in the pulmonary branch zone for snapshot No. 34. However, it is important to highlight that inaccuracies remain highly localized on several mesh cells and involve a limited number of scenarios. Additionally, the area of interest, i.e. the MBTS, maintains a low level of errors. Finally, it is crucial to note that based on the selected number of training data and according to Table 30, in the process of reducing the velocity field data, we lost ≈7.4% of the learning data information, i.e. $e^{\mathrm{RMS}}_{\mathrm{red}}$. While this percentage is significant, it becomes tolerable when considering that the velocity ROM gives predictions across the entire volume.

With respect to pressure and WSS, it can be confirmed that the ROM models correctly represent the full CFD flow pattern even in the worst-case scenarios. Fig. 33b refers to the highest recorded error of the pressure ROM, which was identified in snapshot No. 101. The greatest pressure error ($\approx$1.5 mmHg) is in the middle part of the shunt. The least precise prediction of WSS was characterized by localized discrepancies ($\approx$48 Pa) on the upper partition of the implant, as illustrated in snapshot No. 87 (Figure 33c). It is important to underline the fact that these errors constitute about 2.5% and 6% of the full range of values of pressure and WSS, respectively. Delving into the ROM build-up procedure, presented in section 2.6.2, the percentage reduction error, $e_{\text{red}}^{\text{RMS}}$, is equal to $\approx$0.2% and $\approx$6.0% for the pressure and WSS ROM respectively. Despite both ROMs being computed on the MBTS surface, their data reduction errors differ significantly in magnitude. This indicates that the pressure distribution exhibits small variations in the different MBTS configurations. On the contrary, the distribution of WSS proves to be sensitive to the MBTS morphology.

Based on our preliminary study, mid-dr-vol and mid-dl-vol seem to be the most significant shape modifiers for the distribution of WSSs. Therefore, the curvature of the middle portion of the shunt appears to substantially determine the blood flow. Even though additional studies are needed to confirm this finding, this observation may be relevant for the future optimization of the MBTS implant design.

Finally, the ROM exploitation was performed quickly within a user-friendly and interactive environment, as shown in Fig. 34. To appreciate the exhibited results, the timeframe needed to perform MBTS morphology exploration with the CFD and ROM approaches was presented. The main outcome of this comparison is that if we invest $\approx$20 hours for the ROM build-up, then we can get an estimation of the hemodynamic flow as a function of the selected shape factors of the MBTS in almost-real (Fig. 37). This fast ROM responsiveness could prove useful in clinicians' decision-making process on preoperative planning. Moreover, the Medical Digital Twin presents one more advantage: it can be stored in reduced memory space compared to the full-order model. Consequently, the ROM can be considered a rather competitive surrogate model that has the potential to be inserted into the demanding clinical practice context.

In conclusion, it is worth highlighting the limitations and the potential future directions of the presented pipeline. Initially, it would be valuable to enrich the pool of training data with additional snapshots to assess how much we can minimize the data reduction and the final error. With respect to the CFD modeling, the inclusion of the cardiac motion would significantly increase the reliability of our results. Another aspect for improvement is the lack of time-varying fluid dynamic conditions. Incorporating flow pulsatility could offer a more realistic overview of the examined phenomenon. Lastly, the clinical validation of our results is required. Potential validation methods include employing phase-contrast MRI or utilizing color Doppler ultrasound.

4.2 Study II

In the context of EVAR, a stiff guidewire is inserted from the femoral artery to the aneurysm location to facilitate graft implantation. This maneuver induces significant alterations in the morphology of the aorta. In the preoperative stage, clinicians opt for the most suitable stent graft size relying on a non-updated CT scan, which may result in suboptimal sizing. In the intraoperative stage, for monitoring both the navigating tools and the aortic configuration, 2D fluoroscopy and DSA are employed. These imaging modalities involve the use of radiation and contrast agents, which are harmful to the patients and the clinical personnel. Considering the aforementioned challenges, our motivation was the development of a computational tool that can predict guidewire-induced deformations across various similar patient cases.

In this study, a ROM was developed for the fast and accurate estimation of the aortic deformation due to the insertion of a stiff guidewire as a function of seven critical mechanical, morphological, and clinical parameters. Starting from the abdominal aortic geometry of a patient eligible for EVAR (Fig. 19), we introduced the morphological modifiers α, β, and τ using the RBF mesh morphing technique (Fig. 23). By tuning these parameters, we were able to produce a wide range of possible similar patient configurations. Additionally, the elasticity of the aortic wall

(E_{aorta}) and the guidewire (E_{wire}) as well as the wire's insertion angles (ϕ, θ) were included. 300 combinations of these seven adopted parameters were examined as potential EVAR navigation cases, i.e., scenarios. Among them, 200 scenarios were used for the ROM building. The accuracy of the generated model was statistically assessed. The ROM was validated against the remaining 100 scenarios and its final prediction error, $e_{\text{ROM}}^{\text{rel}}$, was found below 5.5%. Lastly, the ROM exploitation was performed, providing almost real-time calculation of the 3D aortic wall displacement during EVAR (Fig. 40).

As a supplement to this study, we conducted a preliminary qualitative analysis of the effect of the adopted parameters on the aortic displacement field. According to our findings, low E_{aorta} and high E_{wire} values tend to cause large deformations ($\sim$ 13 mm) near the root of the left iliac artery. The aortic stiffness is linked to the presence of calcifications, which is common in patients with abdominal aortic aneurysms, and it has been considered a significant factor in the guidewire-induced deformations[166,46]. With regards to the stiff guidewire, clinicians have different types of wires available, with a minimum Young's modulus of 60 GPa (Amplatz Super Stiff) and a maximum of 200 GPa (Lunderquist Extra Stiff)[135]. Therefore, the ROM prediction could help them choose the appropriate tool, as a compromise between navigability and potential tissue damage.

Our study also showed that high τ values trigger an increased displacement of the left iliac artery towards the posterior direction, while the rest of the geometry moves towards the anterior right direction. This is in agreement with what has been already highlighted in literature: the straightening effect of the guidewire on the common iliac artery increases in case of severe iliac tortuosity[46].

Lastly, through the examination of the effect of the insertion angles, we found that for low ϕ values, the deformations are higher close to the left iliac artery. On the other hand, we observed a poor correlation between the magnitude of θ and the resulting deformations. By analyzing the impact of insertion angles in the 3D space, clinicians can potentially identify the best ones to minimize deformations and stresses on the aortic wall. According to our results, it seems that high angles in the sagittal plane allow the lowering of the aortic displacements.

In literature, there are several works that predict the interaction between the stiff guidewire and the aortic wall through finite element models[133,54,166]. In agreement with Cercenelli *et al.*[46] and Kaladji *et al.*[55], we observed that the area with the highest values of displacement is located at the root of the common iliac artery on the side of insertion for all the considered ROM scenarios. In detail, the study by Kaladji *et al.*[55] reports a magnitude of displacement equal to 10.2 ± 3.3 mm for the cannulated iliac artery, occurring mostly in the posterior-superior direction, similar to what is noticed in the depicted case of Fig. 40.

As illustrated in Fig. 44, the proposed workflow speeds up the aortic displacement calculation in two ways. The mesh-morphing technique morphs the aortic shape rapidly and accurately, enabling the exploration of a wide spectrum of aortic configurations without image segmentation. The total morphing time for all the scenarios was around 30 minutes. Employing the ROM approach, the solution's calculation took a few seconds whereas solving the full-order model required 25 minutes. High-fidelity models are not compatible with the tight clinical intra-operative time frame in which surgeons have to make decisions. On the other hand, our ROM took 135 minutes to be built once, i.e. 125 minutes for the snapshots generation and 10 minutes for the ROM build-up, then it was ready for use and provided real-time response. The ROM data generation time can be further reduced by using larger High-Performance Computing (HPC) facilities. In addition to the above-mentioned timeframes, segmentation and meshing procedures take 45 minutes on average, hence the total ROM pipeline is completed within 3 hours and 30 minutes. Thus, the proposed approach lies within the pre-operative timeframe for non-acute cases and once built, is compatible with intra-operative usage.

With regards to the ROM prediction error, we observed that it is kept below 0.32 mm for all the validation scenarios (Fig. 38). This error is comparable to the spatial resolution of the currently adopted imaging modality for EVAR navigation, i.e., DSA, which is about 0.5 mm[167,168]. Comparing the histograms of Fig. 38, we observe that the final ROM error is one order of magnitude higher than the error triggered by the SVD data reduction. This implies that the error introduced by GARS was rather high, i.e. the surface of Fig. 26 was rough with several spikes, challenging the interpolation between the known mode coefficients. To further reduce this error, additional ROM training is required. However, in this work, the choice of this training set-up was made as a compromise between the computational cost and the ROM accuracy. In addition, the highest errors are detected only in a few scenarios, i.e., 8% of our validation scenarios, and are always localized at a few nodes of the cannulated iliac artery.

While highlighting the strengths of the presented study, it is essential to mention its limitations that can tackled in future works. The proposed workflow can be applied to more tortuous and challenging anatomies to examine the behavior of the ROM in demanding cases. Moreover, more realistic boundary conditions could be considered, including the spine and the structures surrounding the abdominal aorta. Lastly, a hyperelastic material model could be adopted to reach one step closer to reality. Further studies are needed to assess the clinical applicability of the proposed approach.

4.3 Study III

Intra-prosthetic thrombosis (IPT) is one of the most frequent complications of endovascular aneurysm repair (EVAR)[60]. According to the literature, it occurs both in the main body and the graft limbs, and in some cases, it can lead to complete blood occlusion and/or reintervention[71,169]. The graft design appears to play a crucial role, with some clinical studies suggesting that Zenith Alpha has a higher limb graft occlusion (LGO) occurrence compared to other commercial grafts[170,70,43].

In the presented study, we examined the hemodynamics of three simplified models, i.e. model 1, 2, and 3, of the most commonly employed stent-grafts, i.e. Zenith Alpha, Excluder, and Endurant II, in the view of examining their susceptibility in IPT events. The thrombus predisposition was examined by means of shear strain rates (SSR) analysis, WSS-related indices examination, backflow, and velocity vector assessment. According to the presented SSR results, model 1 seems to have an increased likelihood of developing IPT in the flared extension with respect to the rest grafts. What is more, the bifurcating area of all grafts seems prone to IPT. Considering the outcomes of $TAWSS$ analysis, we conclude that almost the whole graft hosts favorable conditions for IPT formation in all the examined stents.

Furthermore, model 1 seems to perform significantly better than the rest grafts, exhibiting IPT preventive behavior mainly on the flared side. Based on the OSI results, model 1 has a higher probability of IPT formation on the straight extension whereas models 2 and 3 are more IPT susceptible in the main body. As for $ECAP$ results, they demonstrate that model 3 is the most IPT prone graft among the examined ones. Finally, with regards to the vector and backflow analysis, we detected that model 1 has a wide recirculating area in the flared extension, which is active for 90% of the duration of the heart cycle. Substantially smaller recirculating areas, with less duration, were found in models 2 and 3.

Considering the presented results, the outcomes of the SSR and vortex analysis, seem to agree on the fact that the flared extension of model 1, and more precisely zones 3, 4, 5 have a high probability of hosting an IPT. This is an interesting finding if we recall that model 1 is the simplified model of the Zenith Alpha stent graft, which has been found to have clinically a relatively high IPT occurrence. Katritsis *et al.*[171] suggested that post-stenotic flow conditions favor platelet aggregation, particularly when previously activated by the elevated shear stresses of a stenotic region. This condition matches our findings for model 1. Another work by Stein and Sabbah[172] demonstrated that flow disturbance, i.e., chaotic flow patterns, can contribute to IPT formation. Based on this finding, the flared extension model 1 is more susceptible to IPT because of the extent and intensity of the chaotic patterns, as illustrated in Fig. 50. Additionally, Yazdani and Karniadakis[173] proved that increased levels of vessel constriction lead to significantly enhanced margination of platelets near the wall. According to Table 2, model 1 has the most significant narrowing in the post-bifurcation area, having a diameter of 11 mm.

Conversely, the WSS-related indices provide us with controversial results which makes their interpretation challenging. The range and the distribution of the $TAWSS$ are in line with similar studies performed on stent grafts[173,67]. However, none of them assumed negative flux during diastole. Another important note is that adopted WSS-related criteria derive mainly from studies correlating thrombus formation and AAAs, not specifically IPT. Sticking on the adopted available criteria, it appears that $TAWSS$ is probably by definition a quite ambiguous index since it accounts purely for the magnitude of the WSS, which can greatly depend on different morphologies. This was also confirmed by Arzani *et al.*[87] who suggested that the analysis of $TAWSS$ is not a robust IPT predictor. Furthermore, Zambrano *et al.*[125] found low $TAWSS$ both in regions with and without intraluminal thrombus formation. Bearing these in mind and considering that OSI and ECAP include $TAWSS$ in their formula (equations 3, 4), maybe we could also question the validity of all the WSS-related parameters with regards to their effectiveness in predicting IPT. Furthermore, some recent studies detected that thrombus can occur both in high and low OSI areas and that $ECAP$ cannot be used as a standalone index for IPT prediction[130,131,174,86]. Finally, the presented WSS-related results were anticipated in the following sense: the bigger cross-sections of model 3 compared to the rest grafts (Table 2), were characterized by lower velocity magnitude, which led to lower $TAWSS$, higher OSI and $ECAP$, i.e. higher likelihood of IPT formation.

The presented study provided some hemodynamic insights into the LGO events that occur in all grafts but with a higher reported frequency in the Zenith Alpha graft. Through the examination of the simplified models, this study pinpointed some factors that could contribute to increased LGO formation on the flared extension of Zenith Alpha graft. No significant differences were found in the analysis of thrombotic parameters in the rest areas of the examined stent grafts.

Finally, it is crucial to acknowledge some limitations of the presented work. Firstly, the considered models were simplified and were not validated against the physical commercial grafts. What is more, the implanted configuration of the grafts can significantly diverge from the simplified studied cases. Therefore, further research is needed to confirm our findings. Additionally, the impact of the selected boundary conditions, i.e., flux profile and Windkessel model, on the results should be explored. Further experimental validation, taking into account the multiscale particle motions, is required to further support our findings.

5 Conclusions

In this thesis, three distinct studies were performed: the first two, i.e., study I and II, were focused on the generation of reduced order models to support the preoperative and intraoperative procedure of MBTS and EVAR respectively. The third study was devoted to the assessment of post-EVAR intra-prosthetic thrombus formation using hemodynamic analysis. In further detail:

- In Study I, we presented three ROMs for the prediction of important hemodynamic flow parameters, i.e., velocity, pressure, and WSS, in function of the implant's shape. The ROMs generation was the most time-consuming part, but its duration can be reduced using powerful computational resources, e.g. HPCs. The ROMs' execution time was compatible with the clinical timeframe, giving responses almost in real time. The accuracy of the developed ROMs was found to be sufficient, with the highest errors being localized in a few cells of the velocity ROM. Upon preliminary exploitation of the WSS ROM, we found out that the curvature of the middle portion of the shunt, appeared to be the most significant shape parameter for the distribution of WSS. If further studies confirm this observation, perhaps we should reconsider and enhance the current implant design accordingly.

- In Study II, we developed a ROM for the prediction of the interaction between the stiff guidewire and the aortic tissue in function of mechanical, clinical, and morphological parameters. This model was potent as it could offer precise predictions of the aortic configuration, covering a wide range of procedure and patient related parameters. The ROM generation was achieved within a few hours. This made it suitable for the preoperative planning and intra-operative navigation of non-acute cases. Once built, its responsiveness was in line with the clinical needs. The ROM accuracy was comparable to the precision of the intra operative imaging techniques. This turns our model into a competent surrogate approach for predicting guidewire induced deformations. Finally, the factors that triggered the highest aortic deformation during EVAR were the increased stiffness of the guidewire, the low elasticity of the aorta, and the high tortuosity of the iliac artery. This observation might suggest that clinicians should focus on the tuning of these critical parameters when using the proposed ROM.

- In Study III, the fluid flow of three simplified commercial stent grafts was analyzed with the view of assessing thrombus development potential. The shear strain rate, the backflow, and the vector analysis indicated that the simplified model of Zenith Alpha graft, i.e. model 1, was found more prone in its flared extension with regards to the rest grafts. This finding is in line with the clinical observations. The WSS-related factors provided us with controversial results. It appears that the adopted thresholds of the WSS indices were not suitable for the analysis of thrombotic events within grafts. Maybe the range of these indices should be updated based on studies exclusively performed on abdominal stent grafts. Another crucial aspect is that the precise geometry of the commercial grafts is needed to extract safe conclusions. However, as mentioned in section 2.2.2, finding industrial grafts with similar dimensions in a physical or digital form was not an option.

Overall, the work in this thesis underlines that the fusion of computational techniques, such as reducing order modeling and mesh morphing, can support the clinical needs related to critical cardiovascular operations. With the developed tools, we attempted to bring patient specific treatment closer to the clinical reality while offering models with high reliability. Additionally, the investigation of thrombotic phenomena in terms of CFD analysis brought some enlightening results. Our main conclusion is that by adopting parameters that are linked tightly to the nature of the problem, we are making progress in understanding and avoiding pathological conditions. Multidisciplinary approaches between clinicians and engineers seem promising for advancing healthcare and medical technology.

Bibliography

[1] Townsend, N.; Kazakiewicz, D.; Lucy Wright, F.; Timmis, A.; Huculeci, R.; Torbica, A.; Gale, C. P.; Achenbach, S.; Weidinger, F.; Vardas, P. Epidemiology of cardiovascular disease in Europe. *Nature Reviews Cardiology* **2022**, *19*, 133–143.

[2] Buttar, H. S.; Li, T.; Ravi, N. Prevention of cardiovascular diseases: Role of exercise, dietary interventions, obesity and smoking cessation. *Experimental & clinical cardiology* **2005**, *10*, 229.

[3] Winkleby, M. A.; Jatulis, D. E.; Frank, E.; Fortmann, S. P. Socioeconomic status and health: how education, income, and occupation contribute to risk factors for cardiovascular disease. *American journal of public health* **1992**, *82*, 816–820.

[4] Mensah, G. A.; Brown, D. W. An overview of cardiovascular disease burden in the United States. *Health affairs* **2007**, *26*, 38–48.

[5] Celermajer, D. S.; Chow, C. K.; Marijon, E.; Anstey, N. M.; Woo, K. S. Cardiovascular disease in the developing world: prevalences, patterns, and the potential of early disease detection. *Journal of the American College of Cardiology* **2012**, *60*, 1207–1216.

[6] Organization, W. H., *et al. Prevention of cardiovascular disease: guidelines for assessment and management of total cardiovascular risk*; World Health Organization, 2007.

[7] Pepys, M. B.; Hirschfield, G. M.; Tennent, G. A.; Ruth Gallimore, J.; Kahan, M. C.; Bellotti, V.; Hawkins, P. N.; Myers, R. M.; Smith, M. D.; Polara, A., *et al.* Targeting C-reactive protein for the treatment of cardiovascular disease. *Nature* **2006**, *440*, 1217–1221.

[8] Jin, Z.; Oresko, J.; Huang, S.; Cheng, A. C. HeartToGo: a personalized medicine technology for cardiovascular disease prevention and detection. 2009 IEEE/NIH Life Science Systems and Applications Workshop. 2009; pp 80–83.

[9] Galvis, M. M. O.; Bhakta, R. T.; Tarmahomed, A.; Mendez, M. D. *StatPearls [Internet]*; StatPearls Publishing, 2023.

[10] Cuypers, J. A. A. E.; Witsenburg, M.; van der Linde, D.; Roos-Hesselink, J. W. Pulmonary stenosis: update on diagnosis and therapeutic options. *Heart* **2013**, *99*, 339–347.

[11] Leonard, H.; Derrick, G.; O'sullivan, J.; Wren, C. Natural and unnatural history of pulmonary atresia. *Heart* **2000**, *84*, 499–503.

[12] Blalock, A.; Taussig, H. B. The surgical treatment of malformations of the heart: in which there is pulmonary stenosis or pulmonary atresia. *Journal of the American Medical Association* **1945**, *128*, 189–202.

[13] Gladman, G.; McCrindle, B. W.; Williams, W. G.; Freedom, R. M.; Benson, L. N. The modified Blalock-Taussig shunt: clinical impact and morbidity in Fallot's tetralogy in the current era. *The Journal of thoracic and cardiovascular surgery* **1997**, *114*, 25–30.

[14] Petrucci, O.; O'Brien, S. M.; Jacobs, M. L.; Jacobs, J. P.; Manning, P. B.; Eghtesady, P. Risk factors for mortality and morbidity after the neonatal Blalock-Taussig shunt procedure. *The Annals of Thoracic Surgery* **2011**, *92*, 642–652.

[15] Ashburn, D. A.; McCrindle, B. W.; Tchervenkov, C. I.; Jacobs, M. L.; Lofland, G. K.; Bove, E. L.; Spray, T. L.; Williams, W. G.; Blackstone, E. H. Outcomes after the Norwood operation in neonates with critical aortic stenosis or aortic valve atresia. *The Journal of Thoracic and Cardiovascular Surgery* **2003**, *125*, 1070–1082.

[16] Zhang, N.; Yuan, H.; Chen, X.; Liu, J.; Jian, Q.; Huang, M.; Zhang, K. Computational fluid dynamics characterization of two patient-specific systemic-to-pulmonary shunts before and after operation. *Computational and Mathematical Methods in Medicine* **2019**, *2019*.

[17] Piskin, S.; Altin, H. F.; Yildiz, O.; Bakir, I.; Pekkan, K. Hemodynamics of patient-specific aorta-pulmonary shunt configurations. *Journal of Biomechanics* **2017**, *50*, 166–171.

[18] de Leval, M. R.; McKay, R.; Jones, M.; Stark, J.; Macartney, F. J. Modified Blalock-Taussig shunt: Use of subclavian artery orifice as flow regulator in prosthetic systemic-pulmonary artery shunts. *The Journal of Thoracic and Cardiovascular Surgery* **1981**, *81*, 112–119.

[19] Alsoufi, B.; Gillespie, S.; Mori, M.; Clabby, M.; Kanter, K.; Kogon, B. Factors affecting death and progression towards next stage following modified Blalock-Taussig shunt in neonates †. *European Journal of Cardio-Thoracic Surgery* **2016**, *50*, 169–177.

[20] Dirks, V.; Prêtre, R.; Knirsch, W.; Valsangiacomo Buechel, E. R.; Seifert, B.; Schweiger, M.; Hübler, M.; Dave, H. Modified Blalock Taussig shunt: a not-so-simple palliative procedure. *European Journal of Cardio-Thoracic Surgery* **2013**, *44*, 1096–1102.

[21] Kim, J.-H. In *Recent Advancements in Microbial Diversity*; Cho, J. Y., Ed.; Academic Press, 2022; pp 229–254.

[22] Ladich, E.; Butany, J.; Virmani, R. In *Cardiovascular Pathology (Fourth Edition)*, fourth edition ed.; Buja, L. M., Butany, J., Eds.; Academic Press: San Diego, 2016; pp 169–211.

[23] Aggarwal, S.; Qamar, A.; Sharma, V.; Sharma, A. Abdominal aortic aneurysm: A comprehensive review. *Experimental & Clinical Cardiology* **2011**, *16*, 11.

[24] Wang, L.; Prabhakar, A.; Kwolek, C. Current status of the treatment of infrarenal abdominal aortic aneurysms. *Cardiovascular Diagnosis and Therapy* **2018**, *8*, S191–S199.

[25] Mathur, A.; Mohan, V.; Ameta, D.; Gaurav, B.; Haranahalli, P. Aortic aneurysm. *Journal of translational internal medicine* **2016**, *4*, 35–41.

[26] Cury, M.; Zeidan, F.; Lobato, A. C., *et al.* Aortic disease in the young: genetic aneurysm syndromes, connective tissue disorders, and familial aortic aneurysms and dissections. *International journal of vascular medicine* **2013**, *2013*.

[27] Accarino, G.; Giordano, A. N.; Falcone, M.; Celano, A.; Vassallo, M. G.; Fornino, G.; Bracale, U. M.; Vecchione, C.; Galasso, G. Abdominal aortic aneurysm: natural history, pathophysiology and translational perspectives. *Translational Medicine@ UniSa* **2022**, *24*, 30.

[28] Moxon, J. V.; Parr, A.; Emeto, T. I.; Walker, P.; Norman, P. E.; Golledge, J. Diagnosis and monitoring of abdominal aortic aneurysm: current status and future prospects. *Current problems in cardiology* **2010**, *35*, 512–548.

[29] Noel, A. A.; Gloviczki, P.; Cherry, K. J.; Bower, T. C.; Panneton, J. M.; Mozes, G. I.; Harmsen, W. S.; Jenkins, G. D.; Hallett, J. W. Ruptured abdominal aortic aneurysms: The excessive mortality rate of conventional repair. *Journal of Vascular Surgery* **2001**, *34*, 41–46.

[30] Moll, F. L.; Powell, J. T.; Fraedrich, G.; Verzini, F.; Haulon, S.; Waltham, M.; van Herwaarden, J. A.; Holt, P. J.; van Keulen, J. W.; Rantner, B., *et al.* Management of abdominal aortic aneurysms clinical practice guidelines of the European society for vascular surgery. *European journal of vascular and endovascular surgery* **2011**, *41*, S1–S58.

[31] Chaikof, E. L.; Dalman, R. L.; Eskandari, M. K.; Jackson, B. M.; Lee, W. A.; Mansour, M. A.; Mastracci, T. M.; Mell, M.; Murad, M. H.; Nguyen, L. L., *et al.* The Society for Vascular Surgery practice guidelines on the care of patients with an abdominal aortic aneurysm. *Journal of vascular surgery* **2018**, *67*, 2–77.

[32] Powell, J.; Sweeting, M.; Brown, L.; Gotensparre, S.; Fowkes, F.; Thompson, S. Systematic review and meta-analysis of growth rates of small abdominal aortic aneurysms. *Journal of British Surgery* **2011**, *98*, 609–618.

[33] Laine, M.; Vänttinen, T.; Kantonen, I.; Halmesmäki, K.; Weselius, E.; Laukontaus, S.; Salenius, J.; Aho, P.; Venermo, M. Rupture of abdominal aortic aneurysms in patients under screening age and elective repair threshold. *European Journal of Vascular and Endovascular Surgery* **2016**, *51*, 511–516.

[34] Schanzer, A.; Oderich, G. S. Management of abdominal aortic aneurysms. *New England Journal of Medicine* **2021**, *385*, 1690–1698.

[35] Oderich, G. S.; Factor, D. *Endovascular aortic repair: current techniques with fenestrated, branched and parallel stent-grafts*; Springer, 2017.

[36] Antoniou, G. A.; Antoniou, S. A.; Torella, F. Editor's Choice–endovascular vs. open repair for abdominal aortic aneurysm: systematic review and meta-analysis of updated peri-operative and long term data of randomised controlled trials. *European Journal of Vascular and Endovascular Surgery* **2020**, *59*, 385–397.

[37] Schermerhorn, M. L.; Buck, D. B.; O'Malley, A. J.; Curran, T.; McCallum, J. C.; Darling, J.; Landon, B. E. Long-term outcomes of abdominal aortic aneurysm in the Medicare population. *New england journal of medicine* **2015**, *373*, 328–338.

[38] Patel, R.; Sweeting, M. J.; Powell, J. T.; Greenhalgh, R. M. Endovascular versus open repair of abdominal aortic aneurysm in 15-years' follow-up of the UK endovascular aneurysm repair trial 1 (EVAR trial 1): a randomised controlled trial. *The Lancet* **2016**, *388*, 2366–2374.

[39] Hirsch, A. T.; Haskal, Z. J.; Hertzer, N. R.; Bakal, C. W.; Creager, M. A.; Halperin, J. L.; Hiratzka, L. F.; Murphy, W. R.; Olin, J. W.; Puschett, J. B., *et al.* ACC/AHA 2005 practice guidelines for the management of patients with peripheral arterial disease (lower extremity, renal, mesenteric, and abdominal aortic) a collaborative report from the American Association for Vascular Surgery/Society for Vascular Surgery,* Society for Cardiovascular Angiography and Interventions, Society for Vascular Medicine and Biology, Society of Interventional Radiology, and the ACC/AHA Task Force on Practice Guidelines (writing committee to develop guidelines for the management of patients with peripheral arterial disease): Endorsed by the American Association of Cardiovascular and Pulmonary Rehabilitation; National Heart, Lung, and Blood Institute; Society for Vascular Nursing; TransAtlantic Inter-Society Consensus; and Vascular Disease Foundation. *circulation* **2006**, *113*, e463–e654.

[40] Cernohorsky, P.; Reijnen, M. M.; Tielliu, I. F.; Van Sterkenburg, S. M.; Van

Den Dungen, J. J.; Zeebregts, C. J. The relevance of aortic endograft prosthetic infection. *Journal of vascular surgery* **2011**, *54*, 327–333.

[41] Laheij, R.; Buth, J.; Harris, P.; Moll, F.; Stelter, W.; Verhoeven, E. Need for secondary interventions after endovascular repair of abdominal aortic aneurysms. Intermediate-term follow-up results of a European collaborative registry (EUROSTAR). *Journal of British Surgery* **2000**, *87*, 1666–1673.

[42] Ucci, A.; Perini, P.; Azzarone, M.; Mariani, E.; Bramucci, A.; D'Ospina, R.; Freyrie, A., *et al.* Prevalence, risk factors and clinical impact of intraprosthetic thrombus deposits after EVAR. *The Journal of Cardiovascular Surgery* **2020**, *61*, 729–737.

[43] Bogdanovic, M.; Stackelberg, O.; Lindström, D.; Ersryd, S.; Andersson, M.; Roos, H.; Siika, A.; Jonsson, M.; Roy, J. Limb graft occlusion following endovascular aneurysm repair for infrarenal abdominal aortic aneurysm with the Zenith Alpha, Excluder, and Endurant devices: a multicentre cohort study. *European Journal of Vascular and Endovascular Surgery* **2021**, *62*, 532–539.

[44] Kim, H. O.; Yim, N. Y.; Kim, J. K.; Kang, Y. J.; Lee, B. C. Endovascular aneurysm repair for abdominal aortic aneurysm: a comprehensive review. *Korean journal of radiology* **2019**, *20*, 1247–1265.

[45] Koutouzi, G.; Pfister, M.; Breininger, K.; Hellström, M.; Roos, H.; Falkenberg, M. Iliac artery deformation during EVAR. *Vascular* **2019**, *27*, 511–517.

[46] Cercenelli, L.; Bortolani, B.; Tiberi, G.; Mascoli, C.; Corazza, I.; Gargiulo, M.; Marcelli, E. Characterization of vessel deformations during EVAR: a preliminary retrospective analysis to improve fidelity of endovascular simulators. *Journal of surgical education* **2018**, *75*, 1096–1105.

[47] Dupont, C.; Kaladji, A.; Rochette, M.; Saudreau, B.; Lucas, A.; Haigron, P. Numerical simulation of fenestrated graft deployment: Anticipation of stent graft and vascular structure adequacy. *International Journal for Numerical Methods in Biomedical Engineering* **2021**, *37*, e03409.

[48] Derycke, L.; Avril, S.; Millon, A. Patient-Specific Numerical Simulations of

Endovascular Procedures in Complex Aortic Pathologies: Review and Clinical Perspectives. *Journal of Clinical Medicine* **2023**, *12*, 766.

[49] Daye, D.; Walker, T. Complications of endovascular aneurysm repair of the thoracic and abdominal aorta: Evaluation and management. Cardiovasc Diagn Ther. 2018; 8 (Supl 1): S138-56.

[50] Maurel, B.; Hertault, A.; Sobocinski, J.; Le Roux, M.; Gonzalez, T. M.; Azzaoui, R.; Saeed Kilani, M.; Midulla, M.; Haulon, S. Techniques to reduce radiation and contrast volume during EVAR. *The Journal of cardiovascular surgery* **2014**, *55*, 123—131.

[51] Condino, S.; Calabrò, E.; Alberti, A.; Parrini, S.; Cioni, R.; Berchiolli, R. N.; Gesi, M.; Ferrari, V.; Ferrari, M. Simultaneous tracking of catheters and guidewires: comparison to standard fluoroscopic guidance for arterial cannulation. *European Journal of Vascular and Endovascular Surgery* **2014**, *47*, 53–60.

[52] Jäckle, S.; Garcia-Vázquez, V.; von Haxthausen, F.; Eixmann, T.; Sieren, M.; Schulz-Hildebrandt, H.; Hüttmann, G.; Ernst, F.; Kleemann, M.; Pätz, T. 3D catheter guidance including shape sensing for endovascular navigation. 2020; p 3.

[53] Gindre, J.; Bel-Brunon, A.; Rochette, M.; Lucas, A.; Kaladji, A.; Haigron, P.; Combescure, A. Patient-specific finite-element simulation of the insertion of guidewire during an EVAR procedure: guidewire position prediction validation on 28 cases. *IEEE Transactions on Biomedical Engineering* **2016**, *64*, 1057–1066.

[54] Mohammadi, H.; Lessard, S.; Therasse, E.; Mongrain, R.; Soulez, G. A numerical preoperative planning model to predict arterial deformations in endovascular aortic aneurysm repair. *Annals of biomedical engineering* **2018**, *46*, 2148–2161.

[55] Kaladji, A.; Dumenil, A.; Castro, M.; Cardon, A.; Becquemin, J.-P.; Bou-Saïd, B.; Lucas, A.; Haigron, P. Prediction of deformations during endovascular aortic aneurysm repair using finite element simulation. *Computerized medical imaging and graphics* **2013**, *37*, 142–149.

[56] Emendi, M.; Støverud, K. H.; Tangen, G. A.; Ulsaker, H.; Manstad-H, F.; Di Giovanni, P.; Dahl, S. K.; Langø, T.; Prot, V. Prediction of guidewire-induced aortic deformations during EVAR: a finite element and in vitro study. *Frontiers in Physiology* **2023**, *14*.

[57] Wegener, M.; Görich, J.; Krämer, S.; Fleiter, T.; Tomczak, R.; Scharrer-Pamler, R.; Kapfer, X.; Brambs, H.-J. Thrombus formation in aortic endografts. *Journal of Endovascular Therapy* **2001**, *8*, 372–379.

[58] Oliveira, N. F.; Gonçalves, F. M. B.; Hoeks, S. E.; Ten Raa, S.; Ultee, K. H.; Rouwet, E.; Hendriks, J. M.; Verhagen, H. J. Clinical outcome and morphologic determinants of mural thrombus in abdominal aortic endografts. *Journal of vascular surgery* **2015**, *61*, 1391–1398.

[59] Russell, T.-A.; Premnath, S.; Mogan, M.; Langford, G.; Paice, B.; Kirk, J.; Rowlands, T.; Kuhan, G. Escalation of antithrombotic therapy should Be considered in the presence of intraluminal prosthetic graft thrombus following endovascular aneurysm repair. EJVES Vascular Forum. 2022; pp 1–5.

[60] Mestres, G.; Maeso, J.; Fernandez, V.; Allegue, N.; Constenla, I.; Matas, M. Incidence and evolution of mural thrombus in abdominal aortic endografts. *Annals of vascular surgery* **2009**, *23*, 627–633.

[61] Shintani, T.; Mitsuoka, H.; Atsuta, K.; Saitou, T.; Higashi, S. Thromboembolic complications after endovascular repair of abdominal aortic aneurysm with neck thrombus. *Vascular and Endovascular Surgery* **2013**, *47*, 172–178.

[62] Png, C. Y. M.; Tadros, R. O.; Faries, P. L.; Torres, M. R.; Kim, S. Y.; Lookstein, R.; Vouyouka, A. G.; Marin, M. L. The effect of age on post-EVAR outcomes. *Annals of Vascular Surgery* **2016**, *35*, 156–162.

[63] Wyss, T. R.; Dick, F.; Brown, L. C.; Greenhalgh, R. M. The influence of thrombus, calcification, angulation, and tortuosity of attachment sites on the time to the first graft-related complication after endovascular aneurysm repair. *Journal of vascular surgery* **2011**, *54*, 965–971.

[64] Chuter, T. A. Stent-graft design: the good, the bad and the ugly. *Cardiovascular Surgery* **2002**, *10*, 7–13.

[65] Demanget, N.; Duprey, A.; Badel, P.; Orgéas, L.; Avril, S.; Geindreau, C.; Albertini, J.-N.; Favre, J.-P. Finite element analysis of the mechanical performances of 8 marketed aortic stent-grafts. *Journal of endovascular therapy* **2013**, *20*, 523–535.

[66] Li, Z.; Kleinstreuer, C. Analysis of biomechanical factors affecting stent-graft migration in an abdominal aortic aneurysm model. *Journal of biomechanics* **2006**, *39*, 2264–2273.

[67] Frauenfelder, T.; Lotfey, M.; Boehm, T.; Wildermuth, S. Computational fluid dynamics: hemodynamic changes in abdominal aortic aneurysm after stent-graft implantation. *Cardiovascular and interventional radiology* **2006**, *29*, 613–623.

[68] Molony, D. S.; Callanan, A.; Morris, L. G.; Doyle, B. J.; Walsh, M. T.; McGloughlin, T. M. Geometrical enhancements for abdominal aortic stent-grafts. *Journal of Endovascular Therapy* **2008**, *15*, 518–529.

[69] Broda, M.; Eiberg, J.; Taudorf, M.; Resch, T. Limb graft occlusion after endovascular aneurysm repair with the Cook Zenith Alpha abdominal graft. *Journal of Vascular Surgery* **2023**, *77*, 770–777.

[70] Ulsaker, H.; Lam, M.; Herje, M. L.; Seternes, A.; Manstad-Hulaas, F. A Retrospective Evaluation of Intra-Prosthetic Thrombus Formation After Endovascular Aortic Repair in Cook Zenith Alpha and Medtronic Endurant II Patients. *European Journal of Vascular and Endovascular Surgery* **2023**,

[71] Draper, K.; Choi, S. H.; Fung, A.; Baxter, K.; Taylor, D.; Chen, J. C.; Misskey, J. Evaluation of factors associated with limb thrombus formation after endovascular aortic aneurysm repair. *Journal of Vascular Surgery* **2023**, *77*, 440–445.

[72] Ashorobi, D.; Ameer, M.; Fernandez, R. Thrombosis. 2022 Sep 5. *StatPearls [Internet]. Treasure Island (FL): StatPearls Publishing* **2023**,

[73] Denorme, F.; Vanhoorelbeke, K.; De Meyer, S. F. von Willebrand factor and platelet glycoprotein Ib: a thromboinflammatory axis in stroke. *Frontiers in immunology* **2019**, *10*, 2884.

[74] Bryckaert, M.; Rosa, J.-P.; Denis, C. V.; Lenting, P. J. Of von Willebrand factor and platelets. *Cellular and Molecular Life Sciences* **2015**, *72*, 307–326.

[75] Bergal, H. T.; Jiang, Y.; Yang, D.; Springer, T. A.; Wong, W. P. Conformation of von Willebrand factor in shear flow revealed with stroboscopic single-molecule imaging. *Blood, The Journal of the American Society of Hematology* **2022**, *140*, 2490–2499.

[76] Sing, C. E.; Alexander-Katz, A. Elongational flow induces the unfolding of von Willebrand factor at physiological flow rates. *Biophysical journal* **2010**, *98*, L35–L37.

[77] Schneider, S.; Nuschele, S.; Wixforth, A.; Gorzelanny, C.; Alexander-Katz, A.; Netz, R.; Schneider, M. F. Shear-induced unfolding triggers adhesion of von Willebrand factor fibers. *Proceedings of the National Academy of Sciences* **2007**, *104*, 7899–7903.

[78] Sheriff, J.; Bluestein, D.; Girdhar, G.; Jesty, J. High-shear stress sensitizes platelets to subsequent low-shear conditions. *Annals of biomedical engineering* **2010**, *38*, 1442–1450.

[79] Nobili, M.; Sheriff, J.; Morbiducci, U.; Redaelli, A.; Bluestein, D. Platelet activation due to hemodynamic shear stresses: damage accumulation model and comparison to in vitro measurements. *ASAIO journal (American Society for Artificial Internal Organs: 1992)* **2008**, *54*, 64.

[80] Yun, S.-H.; Sim, E.-H.; Goh, R.-Y.; Park, J.-I.; Han, J.-Y., *et al.* Platelet activation: the mechanisms and potential biomarkers. *BioMed research international* **2016**, *2016*.

[81] Periayah, M. H.; Halim, A. S.; Saad, A. Z. M. Mechanism action of platelets and crucial blood coagulation pathways in hemostasis. *International journal of hematology-oncology and stem cell research* **2017**, *11*, 319.

[82] Casa, L. D.; Ku, D. N. Thrombus formation at high shear rates. *Annual review of biomedical engineering* **2017**, *19*, 415–433.

[83] Davies, P. F. Hemodynamic shear stress and the endothelium in cardiovascular pathophysiology. *Nature clinical practice Cardiovascular medicine* **2009**, *6*, 16–26.

[84] Kelsey, L. J.; Powell, J. T.; Norman, P. E.; Miller, K.; Doyle, B. J. A comparison of hemodynamic metrics and intraluminal thrombus burden in a common iliac artery aneurysm. *International journal for numerical methods in biomedical engineering* **2017**, *33*, e2821.

[85] Tzirakis, K.; Kamarianakis, Y.; Kontopodis, N.; Ioannou, C. V. The Effect of Blood Rheology and Inlet Boundary Conditions on Realistic Abdominal Aortic Aneurysms under Pulsatile Flow Conditions. *Bioengineering* **2023**, *10*, 272.

[86] Tzirakis, K.; Kamarianakis, Y.; Metaxa, E.; Kontopodis, N.; Ioannou, C. V.; Papaharilaou, Y. A robust approach for exploring hemodynamics and thrombus growth associations in abdominal aortic aneurysms. *Medical & Biological Engineering & Computing* **2017**, *55*, 1493–1506.

[87] Arzani, A.; Suh, G.-Y.; Dalman, R. L.; Shadden, S. C. A longitudinal comparison of hemodynamics and intraluminal thrombus deposition in abdominal aortic aneurysms. *American Journal of Physiology-Heart and Circulatory Physiology* **2014**, *307*, H1786–H1795.

[88] Katritsis, D.; Theodorakakos, A.; Pantos, I.; Andriotis, A.; Efstathopoulos, E.; Siontis, G.; Karcanias, N.; Redwood, S.; Gavaises, M. Vortex formation and recirculation zones in left anterior descending artery stenoses: computational fluid dynamics analysis. *Physics in Medicine & Biology* **2010**, *55*, 1395.

[89] Wurzinger, L.; Opitz, R.; Blasberg, P.; Schmid-Schönbein, H. Platelet and coagulation parameters following millisecond exposure to laminar shear stress. *Thrombosis and haemostasis* **1985**, *54*, 381–386.

[90] Martorell, J.; Santoma, P.; Kolandaivelu, K.; Kolachalama, V. B.; Melgar-Lesmes, P.; Molins, J. J.; Garcia, L.; Edelman, E. R.; Balcells, M. Extent of flow recirculation governs expression of atherosclerotic and thrombotic biomarkers in arterial bifurcations. *Cardiovascular research* **2014**, *103*, 37–46.

[91] Petrou, M. M.; Petrou, C. *Image processing: the fundamentals*; John Wiley & Sons, 2010.

[92] Hollands, J. G.; Terhaar, P.; Pavlovic, N. J. Effects of resolution, range, and image contrast on target acquisition performance. *Human factors* **2018**, *60*, 363–383.

[93] Haralick, R. M.; Shapiro, L. G. Image segmentation techniques. *Computer vision, graphics, and image processing* **1985**, *29*, 100–132.

[94] Cheng, H.-D.; Jiang, X. H.; Sun, Y.; Wang, J. Color image segmentation: advances and prospects. *Pattern recognition* **2001**, *34*, 2259–2281.

[95] Milletari, F.; Navab, N.; Ahmadi, S.-A. V-net: Fully convolutional neural networks for volumetric medical image segmentation. 2016 fourth international conference on 3D vision (3DV). 2016; pp 565–571.

[96] Seo, H.; Badiei Khuzani, M.; Vasudevan, V.; Huang, C.; Ren, H.; Xiao, R.; Jia, X.; Xing, L. Machine learning techniques for biomedical image segmentation: an overview of technical aspects and introduction to state-of-art applications. *Medical physics* **2020**, *47*, e148–e167.

[97] Sharp, G.; Fritscher, K. D.; Pekar, V.; Peroni, M.; Shusharina, N.; Veeraraghavan, H.; Yang, J. Vision 20/20: perspectives on automated image segmentation for radiotherapy. *Medical physics* **2014**, *41*, 050902.

[98] Starly, B.; Fang, Z.; Sun, W.; Shokoufandeh, A.; Regli, W. Three-dimensional reconstruction for medical-CAD modeling. *Computer-Aided Design and Applications* **2005**, *2*, 431–438.

[99] 3D Slicer. `https://www.slicer.org/`, 2023.

[100] SpaceClaim. Ansys, 2022.

[101] Elella, R. A.; Umereta, N.; Alabari, I.; Al Ahmadi, M.; Al Wadai, A. The short-and long-term effect of Blalock-Taussig shunt size on the outcome after first palliative surgery for cyanotic heart diseases. *Annals of Saudi Medicine* **2014**, *34*, 494–498.

[102] Meshmixer. Autodesk Inc., 2019.

[103] Baker, T. J. Mesh generation: Art or science? *Progress in Aerospace Sciences* **2005**, *41*, 29–63.

[104] Edelsbrunner, H. *Geometry and topology for mesh generation*; Cambridge University Press, 2001.

[105] Staša, P.; Kebo, V.; Kodym, O. Effect of mesh density on the accuracy of the calculation using CFD. 14th International Multidisciplinary Scientific Geo-Conference SGEM 2014. 2014; pp 161–168.

[106] Tucker, P. G. *Advanced computational fluid and aerodynamics*; Cambridge University Press, 2016; Vol. 54.

[107] Liu, J.; Sun, Q.; Qian, Y.; Hong, H.; Liu, J. Numerical simulation and hemodynamic analysis of the modified Blalock-Taussig shunt. 2013 35th Annual International Conference of the IEEE Engineering in Medicine and Biology Society (EMBC). 2013; pp 707–710.

[108] Capellini, K.; Vignali, E.; Costa, E.; Gasparotti, E.; Biancolini, M. E.; Landini, L.; Positano, V.; Celi, S. Computational fluid dynamic study for aTAA hemodynamics: an integrated image-based and radial basis functions mesh morphing approach. *Journal of biomechanical engineering* **2018**, *140*.

[109] Liu, J.; Sun, Q.; Qian, Y.; Hong, H.; Liu, J. Numerical simulation and hemodynamic analysis of the modified Blalock-Taussig shunt. 2013 35th Annual International Conference of the IEEE Engineering in Medicine and Biology Society (EMBC). 2013; pp 707–710.

[110] Perktold, K.; Peter, R.; Resch, M.; Langs, G. Pulsatile non-newtonian blood flow in three-dimensional carotid bifurcation models: a numerical study of flow phenomena under different bifurcation angles. *Journal of Biomedical Engineering* **1991**, *13*, 507–515.

[111] Kabir, M. A.; Sultana, K.; Uddin, M. A. Performance of k-ω and k-ε Model for Blood Flow Simulation in Stenosed Artery. *Ganit: Journal of Bangladesh Mathematical Society* **2020**, *40*.

[112] Perinajová, R.; Juffermans, J. F.; Mercado, J. L.; Aben, J.-P.; Ledoux, L.; Westenberg, J. J.; Lamb, H. J.; Kenjereš, S. Assessment of turbulent blood

flow and wall shear stress in aortic coarctation using image-based simulations. *Biomedical engineering online* **2021**, *20*, 84.

[113] Pedley, T. J. The fluid mechanics of large blood vessels. *(No Title)* **1980**,

[114] Berger, S.; Jou, L.-D. Flows in stenotic vessels. *Annual review of fluid mechanics* **2000**, *32*, 347–382.

[115] Fung, Y.-c. *Biomechanics: circulation*; Springer Science & Business Media, 2013.

[116] Bundy, J. D.; Li, C.; Stuchlik, P.; Bu, X.; Kelly, T. N.; Mills, K. T.; He, H.; Chen, J.; Whelton, P. K.; He, J. Systolic blood pressure reduction and risk of cardiovascular disease and mortality: a systematic review and network meta-analysis. *JAMA cardiology* **2017**, *2*, 775–781.

[117] Nuntnarumit, P.; Yang, W.; Bada-Ellzey, H. S. Blood pressure measurements in the newborn. *Clinics in perinatology* **1999**, *26*, 981–996.

[118] Abman, S. H.; Hansmann, G.; Archer, S. L.; Ivy, D. D.; Adatia, I.; Chung, W. K.; Hanna, B. D.; Rosenzweig, E. B.; Raj, J. U.; Cornfield, D., *et al.* Pediatric pulmonary hypertension: guidelines from the American heart association and American thoracic Society. *Circulation* **2015**, *132*, 2037–2099.

[119] Cheng, C. P.; Herfkens, R. J.; Taylor, C. A. Comparison of abdominal aortic hemodynamics between men and women at rest and during lower limb exercise. *Journal of vascular surgery* **2003**, *37*, 118–123.

[120] Taylor, C. A.; Cheng, C. P.; Espinosa, L. A.; Tang, B. T.; Parker, D.; Herfkens, R. J. In vivo quantification of blood flow and wall shear stress in the human abdominal aorta during lower limb exercise. *Annals of biomedical engineering* **2002**, *30*, 402–408.

[121] Moore Jr, J. E.; Maier, S. E.; Ku, D. N.; Boesiger, P. Hemodynamics in the abdominal aorta: a comparison of in vitro and in vivo measurements. *Journal of Applied Physiology* **1994**, *76*, 1520–1527.

[122] Casa, L. D.; Deaton, D. H.; Ku, D. N. Role of high shear rate in thrombosis. *Journal of vascular surgery* **2015**, *61*, 1068–1080.

[123] Ruggeri, Z. M. The role of von Willebrand factor in thrombus formation. *Thrombosis research* **2007**, *120*, S5–S9.

[124] Sakariassen, K. S.; Orning, L.; Turitto, V. T. The impact of blood shear rate on arterial thrombus formation. *Future science OA* **2015**, *1*.

[125] Zambrano, B. A.; Gharahi, H.; Lim, C.; Jaberi, F. A.; Choi, J.; Lee, W.; Baek, S. Association of intraluminal thrombus, hemodynamic forces, and abdominal aortic aneurysm expansion using longitudinal CT images. *Annals of biomedical engineering* **2016**, *44*, 1502–1514.

[126] Buck, A. K.; Groszek, J. J.; Colvin, D. C.; Keller, S. B.; Kensinger, C.; Forbes, R.; Karp, S.; Williams, P.; Roy, S.; Fissell, W. H. Combined in silico and in vitro approach predicts low WSS regions in a hemofilter that correlate with thrombus formation in vivo. *ASAIO journal (American Society for Artificial Internal Organs: 1992)* **2018**, *64*, 211.

[127] Dimmeler, S.; Fleming, I.; Fisslthaler, B.; Hermann, C.; Busse, R.; Zeiher, A. M. Activation of nitric oxide synthase in endothelial cells by Akt-dependent phosphorylation. *Nature* **1999**, *399*, 601–605.

[128] Gerritsen, M. E. Functional heterogeneity of vascular endothelial cells. *Biochemical pharmacology* **1987**, *36*, 2701–2711.

[129] Belkacemi, D.; Tahar Abbes, M.; Al-Rawi, M.; Al-Jumaily, A. M.; Bachene, S.; Laribi, B. Intraluminal Thrombus Characteristics in AAA Patients: Non-Invasive Diagnosis Using CFD. *Bioengineering* **2023**, *10*, 540.

[130] Di Achille, P.; Tellides, G.; Figueroa, C.; Humphrey, J. A haemodynamic predictor of intraluminal thrombus formation in abdominal aortic aneurysms. *Proceedings of the Royal Society A: Mathematical, Physical and Engineering Sciences* **2014**, *470*, 20140163.

[131] O'Rourke, M. J.; McCullough, J. P.; Kelly, S. An investigation of the relationship between hemodynamics and thrombus deposition within patient-specific models of abdominal aortic aneurysm. *Proceedings of the Institution of Mechanical Engineers, Part H: Journal of Engineering in Medicine* **2012**, *226*, 548–564.

[132] Zambrano, B. A.; Gharahi, H.; Lim, C. Y.; Lee, W.; Baek, S. Association of vortical structures and hemodynamic parameters for regional thrombus accumulation in abdominal aortic aneurysms. *International journal for numerical methods in biomedical engineering* **2022**, *38*, e3555.

[133] Gindre, J.; Bel-Brunon, A.; Kaladji, A.; Duménil, A.; Rochette, M.; Lucas, A.; Haigron, P.; Combescure, A. Finite element simulation of the insertion of guidewires during an EVAR procedure: example of a complex patient case, a first step toward patient-specific parameterized models. *International journal for numerical methods in biomedical engineering* **2015**, *31*, e02716.

[134] Vallabhaneni, S. R.; Gilling-Smith, G. L.; How, T. V.; Carter, S. D.; Brennan, J. A.; Harris, P. L. Heterogeneity of tensile strength and matrix metalloproteinase activity in the wall of abdominal aortic aneurysms. *Journal of Endovascular Therapy* **2004**, *11*, 494–502.

[135] Harrison, G.; How, T.; Vallabhaneni, S. R.; Brennan, J.; Fisher, R.; Naik, J.; McWilliams, R. Guidewire Stiffness: What's in a Name? *Journal of endovascular therapy* **2011**, *18*, 797–801.

[136] Biancolini, M. E. Fast Radial Basis Functions for Engineering Applications. 2018.

[137] De Boer, A.; Van der Schoot, M. S.; Bijl, H. Mesh deformation based on radial basis function interpolation. *Computers & structures* **2007**, *85*, 784–795.

[138] Biancolini, M.; Valentini, P. P. Virtual human bone modelling by interactive sculpting, mesh morphing and force-feedback. *International Journal on Interactive Design and Manufacturing (IJIDeM)* **2018**, *12*, 1–12.

[139] Micchelli, C. A. In *Approximation Theory and Spline Functions*; Singh, S. P., Burry, J. W. H., Watson, B., Eds.; Springer Netherlands: Dordrecht, 1984; pp 143–145.

[140] Acar, E. Optimizing the shape parameters of radial basis functions: An application to automobile crashworthiness. *Proceedings of the Institution of Mechanical Engineers, Part D: Journal of Automobile Engineering* **2010**, *224*, 1541–1553.

[141] Zhang, H.; Zhang, X.; Bu, R. Radial Basis Function Neural Network Sliding Mode Control for Ship Path Following Based on Position Prediction. *Journal of Marine Science and Engineering* **2021**, *9*.

[142] Morelli, M.; Bellosta, T.; Guardone, A. Efficient radial basis function mesh deformation methods for aircraft icing. *Journal of Computational and Applied Mathematics* **2021**, *392*, 113492.

[143] Lei, L.; Liu, W. Predictive control of multi-zone variable air volume air-conditioning system based on radial basis function neural network. *Energy and Buildings* **2022**, *261*, 111944.

[144] Carr, J.; Fright, W.; Beatson, R. Surface interpolation with radial basis functions for medical imaging. *IEEE Transactions on Medical Imaging* **1997**, *16*, 96–107.

[145] Kardampiki, E.; Vignali, E.; Haxhiademi, D.; Federici, D.; Ferrante, E.; Porziani, S.; Chiappa, A.; Groth, C.; Cioffi, M.; Biancolini, M. E., *et al.* The hemodynamic effect of modified blalock–taussig shunt morphologies: A computational analysis based on reduced order modeling. *Electronics* **2022**, *11*, 1930.

[146] Biancolini, M.; Capellini, K.; Costa, E.; Groth, C.; Celi, S. Fast interactive CFD evaluation of hemodynamics assisted by RBF mesh morphing and reduced order models: the case of aTAA modelling. *International Journal on Interactive Design and Manufacturing (IJIDeM)* **2020**, *14*, 1–12.

[147] Kim, T.-H.; Jang, H.-J.; Choi, Y. J.; Lee, C. K.; Kwon, S. W.; Shim, W.-H. Kilt technique as an angle modification method for endovascular repair of abdominal aortic aneurysm with severe neck angle. *Annals of Thoracic and Cardiovascular Surgery* **2017**, *23*, 96–103.

[148] van Keulen, J. W.; Moll, F. L.; Tolenaar, J. L.; Verhagen, H. J.; van Herwaarden, J. A. Validation of a new standardized method to measure proximal aneurysm neck angulation. *Journal of Vascular Surgery* **2010**, *51*, 821–828.

[149] Piccinelli, M.; Veneziani, A.; Steinman, D. A.; Remuzzi, A.; Antiga, L. A

framework for geometric analysis of vascular structures: application to cerebral aneurysms. *IEEE transactions on medical imaging* **2009**, *28*, 1141–1155.

[150] Mathlouthi, A.; Locham, S.; Dakour-Aridi, H.; Black, J. H.; Malas, M. B. Impact of suprarenal neck angulation on endovascular aneurysm repair outcomes. *Journal of Vascular Surgery* **2020**, *71*, 1900–1906.

[151] Benner, P.; Ohlberger, M.; Patera, A.; Rozza, G.; Urban, K., *et al.* Model reduction of parametrized systems. **2017**,

[152] Formentin, S.; van Heusden, K.; Karimi, A. Model-based and data-driven model-reference control: A comparative analysis. 2013 European Control Conference (ECC). 2013; pp 1410–1415.

[153] Eriksson, L.; Johansson, E.; Kettaneh-Wold, N.; Wikström, C.; Wold, S. Design of experiments. *Principles and Applications, Learn ways AB, Stockholm* **2000**,

[154] Antony, J. *Design of experiments for engineers and scientists*; Elsevier, 2014.

[155] Wall, M. E.; Rechtsteiner, A.; Rocha, L. M. Singular value decomposition and principal component analysis. *A practical approach to microarray data analysis* **2003**, 91–109.

[156] Ientilucci, E. J. Using the singular value decomposition. *Rochester Institute of Technology, Rochester, New York, United States, Technical Report* **2003**,

[157] Khuri, A. I.; Mukhopadhyay, S. Response surface methodology. *Wiley Interdisciplinary Reviews: Computational Statistics* **2010**, *2*, 128–149.

[158] Samady, H.; Eshtehardi, P.; McDaniel, M. C.; Suo, J.; Dhawan, S. S.; Maynard, C.; Timmins, L. H.; Quyyumi, A. A.; Giddens, D. P. Coronary artery wall shear stress is associated with progression and transformation of atherosclerotic plaque and arterial remodeling in patients with coronary artery disease. *Circulation* **2011**, *124*, 779–788.

[159] Urschel, K.; Tauchi, M.; Achenbach, S.; Dietel, B. Investigation of wall shear stress in cardiovascular research and in clinical practice—from bench to bedside. *International Journal of Molecular Sciences* **2021**, *22*, 5635.

[160] Bove, E. L.; Migliavacca, F.; de Leval, M. R.; Balossino, R.; Pennati, G.; Lloyd, T. R.; Khambadkone, S.; Hsia, T.-Y.; Dubini, G. Use of mathematic modeling to compare and predict hemodynamic effects of the modified Blalock–Taussig and right ventricle–pulmonary artery shunts for hypoplastic left heart syndrome. *The Journal of Thoracic and Cardiovascular Surgery* **2008**, *136*, 312–320.e2.

[161] Wardoyo, S.; Makdinata, W.; Wijayanto, M. A. Perioperative strategy to minimize mortality in neonatal modified Blalock–Taussig–Thomas Shunt: A literature review. *Cirugía Cardiovascular* **2022**, *29*, 31–35.

[162] Biancolini, M. E.; Capellini, K.; Costa, E.; Groth, C.; Celi, S. Fast interactive CFD evaluation of hemodynamics assisted by RBF mesh morphing and reduced order models: The case of aTAA modelling. *International Journal on Interactive Design and Manufacturing (IJIDeM)* **2020**, *14*, 1227–1238.

[163] Geronzi, L.; Gasparotti, E.; Capellini, K.; Cella, U.; Groth, C.; Porziani, S.; Chiappa, A.; Celi, S.; Biancolini, M. E. High fidelity fluid-structure interaction by radial basis functions mesh adaption of moving walls: A workflow applied to an aortic valve. *Journal of Computational Science* **2021**, *51*, 101327.

[164] Aslan, S.; Guillot, M.; Ross-Ascuitto, N.; Ascuitto, R. Hemodynamics in a bidirectional Glenn Shunt supplemented with a modified Blalock-Taussig shunt: Computational fluid dynamics assessment. *Progress in Pediatric Cardiology* **2021**, *60*, 101256.

[165] Zhang, N.; Haiyun, Y.; Chen, X.; Liu, J.; Zhou, C.; Huang, M.; Qifei, J.; Zhuang, J. Hemodynamic of the Patent Ductus Arteriosus in Neonates with Modified Blalock-Taussig Shunts. *Computer Methods and Programs in Biomedicine* **2019**, *186*, 105223.

[166] McLennan, S.; Soulez, G.; Mongrain, R.; Mohammadi, H.; Pfister, M.; Lessard, S.; Jabbour, G.; Therasse, E. Impact of Calcification Modelling to Improve Image Fusion Accuracy for Endovascular Aortic Aneurysm Repair. *International Journal for Numerical Methods in Biomedical Engineering* **2021**, *38*.

[167] Ota, H.; Takase, K.; Rikimaru, H.; Tsuboi, M.; Yamada, T.; Sato, A.; Higano, S.; Ishibashi, T.; Takahashi, S. Quantitative vascular measurements in arterial occlusive disease. *Radiographics* **2005**, *25*, 1141–1158.

[168] Guimaraes, M.; Schönholz, C.; Uflacker, R.; Huda, W. In *Comprehensive Vascular and Endovascular Surgery (Second Edition)*, second edition ed.; Hallett, J. W., Mills, J. L., Earnshaw, J. J., Reekers, J. A., Rooke, T. W., Eds.; Mosby: Philadelphia, 2009; pp 73–116.

[169] Wang, G.; Zhai, S.; Li, T.; Li, X.; Lu, D.; Wang, B.; Zhang, D.; Shi, S.; Zhang, Z.; Liang, K., *et al.* Limb graft occlusion following endovascular aortic repair: Incidence, causes, treatment and prevention in a study cohort. *Experimental and therapeutic medicine* **2017**, *14*, 1763–1768.

[170] Wu, I.; Liang, P.; Huang, S.; Chi, N.; Lin, F.; Wang, S.-S. The significance of endograft geometry on the incidence of intraprosthetic thrombus deposits after abdominal endovascular grafting. *European Journal of Vascular and Endovascular Surgery* **2009**, *38*, 741–747.

[171] Katritsis, D.; Kaiktsis, L.; Chaniotis, A.; Pantos, J.; Efstathopoulos, E. P.; Marmarelis, V. Wall shear stress: theoretical considerations and methods of measurement. *Progress in cardiovascular diseases* **2007**, *49*, 307–329.

[172] Stein, P. D.; Sabbah, H. N. Measured turbulence and its effect on thrombus formation. *Circulation Research* **1974**, *35*, 608–614.

[173] Yazdani, A.; Karniadakis, G. E. Sub-cellular modeling of platelet transport in blood flow through microchannels with constriction. *Soft Matter* **2016**, *12*, 4339–4351.

[174] Qing, M.; Qiu, Y.; Wang, J.; Zheng, T.; Yuan, D. A Comparative Study on the Hemodynamic Performance within Cross and Non-cross Stent-Grafts for Abdominal Aortic Aneurysms with an Angulated Neck. *Frontiers in Physiology* **2021**, *12*, 795085.